

The double Fano cavity

An investigation of Fano cavity resonances based on the guided-modes of sub-wavelength gratings on suspended
SiN membranes

by

Mikkel Kirkegaard Thomsen | 201804798

Supervisor
Aurelien Dantan

A thesis presented for the degree of
Master of Science



Department of Physics & Astronomy
Aarhus University
Denmark
01.06.2025

Contents

Abstract	iii
1 Introduction	1
2 Theory	4
2.1 The Fabry-Perot interferometer	4
2.1.1 Transmission	4
2.1.2 Varying the cavity length	6
2.1.3 Varying the incident wavelength	8
2.1.4 Cavity losses	9
2.2 The Fano mirror: a sub wavelength grating	10
2.2.1 Reflection/transmission spectra and line shape analysis .	10
2.2.2 Lossless grating	10
2.2.3 Lossy grating	14
2.3 The single Fano cavity	15
2.3.1 The single Fano cavity model	15
2.3.2 Transmission linewidth	16
2.4 The double Fano cavity	20
2.4.1 The double Fano cavity model	20
2.4.2 Transmission linewidth	22
2.4.3 Single and double Fano cavity comparison	22
2.4.4 Additional cavity losses	24
2.4.5 Spectral detuning (lossless)	27
2.4.6 Spacial detuning (lossless)	31
3 Method	37
3.1 The experimental setup	37
3.1.1 Tunable diode laser	38
3.1.2 $\lambda/2$ - waveplate	39
3.1.3 Optical telescope	40
3.1.4 Transmission, reflection and incident photo-detectors .	40
3.1.5 The double Fano cavity measurement setup	41
3.1.6 Vibrational noise reduction	44
3.1.7 Additional equipment used	44
3.2 Characterization of sub-wavelength grating	45
3.2.1 The alignment procedure	45

3.2.2	Adjusting and measuring the beam waist	48
3.2.3	Obtaining normalized transmission/reflection spectra	50
3.3	Cavity measurements	51
3.3.1	Aligning the double Fano cavity	52
3.3.2	Cavity resonance - the piezo ring	54
3.3.3	Determining the cavity length	57
3.3.4	Recording normalized spectra	57
3.3.5	Centering of the top grating	59
3.3.6	Estimating parallelism	62
4	Results	64
4.1	Fano mirror characterization	64
4.2	The single Fano cavity	66
4.3	The double Fano cavity	70
4.3.1	Realizing the double fano model	72
4.3.2	The double fano linewidth	77
4.4	Additional discussion	80
4.4.1	Vibrational noise	80
4.4.2	Guided-mode resonance shift	82
4.4.3	Potential broadening due to walk-off effect	84
5	Conclusion	86
5.1	Outlook	86
5.1.1	Matching analytical and experimental linewidths	86
5.1.2	Optomechanics with the double Fano cavity	87
5.1.3	Sensing applications of the double Fano cavity	87
5.1.4	Fano laser based on bound states in the continuum	87
References		89
Appendices		94
A	Simulated broadband and single Fano cavity resonance transmission spectra	94
B	Simulated single and double Fano cavity resonance transmission spectra	96
C	Simulated double Fano cavity resonance transmission spectra for different values of the resonant loss term	97
D	Measured single Fano transmission data	98
E	Measured double Fano transmission data	105

Abstract

1 Introduction

Cavity electrodynamics[1] is the study of light confined inside an optical resonator and, in the case of this project, quantized as a basis of harmonic oscillator modes[2]. The quantization of the electromagnetic (EM) field inside an optical cavity has been, and continues to be, paramount in the advancement of fields such as optical communication, quantum optics, photonics, sensing, optomechanics[3, 4], etc. The ability to enhance mode selection of a coherent light source allows for an increase in control of a given system, and highly resolved measurements[5].

Many different types of resonators and materials have been utilized for cavity electrodynamics, e.g. beams, drums, photonic crystals and membranes[6, 7]. The latter is here of specific interest, as low mass *Silicon Nitride (SiN)* membranes[8] have proven to posses low losses in the visible- and infrared spectral ranges[9], and has furthermore been shown to have excellent mechanical properties[10, 11]. Examples of applications of *SiN* membranes as mechanical resonators used in cavity electrodynamics are as transducers between optical and microwave fields in telecommunication[12, 13] and in sensing for accelerometry[14, 15], thermometry[16, 17, 18] and pressure sensing[19, 20, 21, 22].

However, while *SiN* membranes are great mechanical resonators, they typically display relatively low reflectivities of $\sim 10\% - 35\%$. That is when only the bare membrane is considered. In order to preserve the quality of the mechanical properties along with the low mass, while achieving higher values for the reflectivity, the membranes are patterned with periodic sub-wavelength, 1- or 2-dimensional, photonic crystal structures[23, 24, 25, 26, 27, 28, 29]. In the past decade, tremendous strides have been made in the field of micro- and nano-fabrication methods, and patterned membranes with a record reflectivity of as high as $\sim 99.9998\%$ have been reported[30, 31, 32].

The type of patterned membrane considered for this project is a 1-dimensional sub-wavelength grating with optical properties well-described by the theory presented by Fan and Joannopoulos [33, 34]. It is thus said to act as so-called *Fano mirrors* with transmission and reflection coefficients dependent on the incident wavelength. The wavelength-dependence gives rise to a *guided-mode* resonance which can be utilized in the designing of optical *Fano* cavities with spectra showcasing ultra-narrow linewidth resonance peaks[35, 36]. By tuning the cavity mode and incoming EM-field to match the guided-mode, one can resolve structures with a linewidth in the low picometer regime for cavity lengths

down to a few microns.

In previous work, the single Fano cavity has been realized and characterized, consisting of a broadband mirror and a Fano mirror in a plane-plane configuration. The Fano cavity have proved to produce ultra-narrow linewidth resonance spectra for very short cavity lengths, while still maintaining a high radiation pressure and thus mechanical Q-factor. This makes them an excellent candidate as subjects for optomechanical experiments and corresponding sensing applications.

In this project we propose the *double Fano cavity* as an expansion of the theory presented for the single Fano cavity by Mitra et al. in [35]. The double Fano cavity consists of two Fano mirrors with each their wavelength-dependent set of optical coefficients and will thus, theoretically, produce an even narrower resonance profile than the *single* Fano cavity. Figure 1 shows schematics for all three aforementioned optical cavities, namely the broadband cavity (1a), single Fano cavity (1b) and double Fano cavity (1c), where t_g, r_g refers to transmission- and reflection coefficients of a Fano mirror, and t_m, r_m are the ones for a broadband mirror.

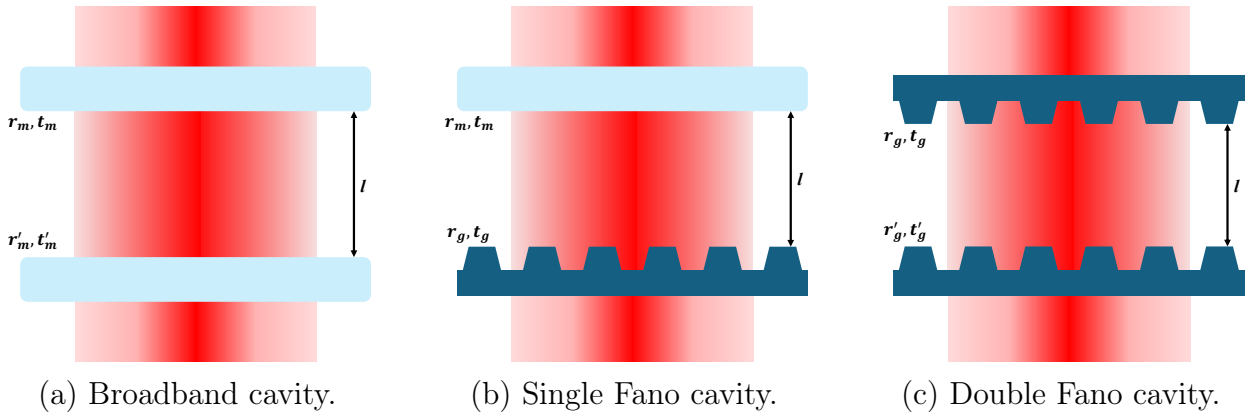


Figure 1

In this thesis I will present the theory of the sub-wavelength grating, i.e. Fano mirrors, and of the single- and double Fano cavities. I will show extensive simulations run for the transmission spectra of the double Fano cavity as a part of my investigations in order to map the on- and off-resonance behaviour as functions of various physical parameters. I will expand in detail on the experimental methods and techniques used in order to realize said theory and outline obstacles faced in that process. Finally I will present the results of my project and compare these with analytical predictions and discuss shortcomings and sources of error and noise of the setup and methods used. I will end by

briefly dicussing the possible outlook of future projects regarding the double Fano cavity and the field of cavity electrodynamics generally in the light of my findings.

2 Theory

2.1 The Fabry-Perot interferometer

The Fabry-Perot interferometer, also known as an optical cavity, is generally comprised of two reflective optical elements, hereafter referred to as mirrors. In the following we assume a plane-plane configuration for two lossless mirrors and a plane-wave at normal incidence for the incoming field, as sketched in figure 2.

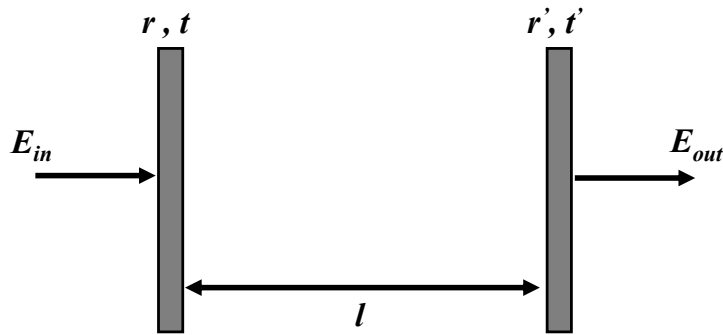


Figure 2: Sketch of a planar Fabry-Perot cavity.

The two mirrors are described by each their respective reflectivity r and transmission t and are placed parallel at a distance l from each other. The field at the second mirror, i.e. the transmitted field E_{out} can then be described as a function of the field at the first mirror, i.e. the incident field E_{in} . The Fabry-Perot cavity furthermore gives rise to so-called eigenstates related to its length l , derived from considering the path difference between successive parallel beams through the cavity. Any allowed mode inside the cavity, and thus transmitted, must fulfill the brightness condition $2l = m\lambda$, where λ is the wavelength of the incident field and $m = 1, 2, 3, \dots$ is a positive integer.[37][38]

2.1.1 Transmission

In order to determine the transmission through the Fabry-Perot cavity, we once again consider the configuration in figure 2. It is further, initially, assumed that the mirrors are both lossless, such that

$$|r|^2 + |t|^2 = |r'|^2 + |t'|^2 = 1. \quad (1)$$

This means that all losses, e.g. due to absorption or scattering, are neglected.

In order to formulate E_{out} in terms of E_{in} , we first consider the incident field as a propagating plane-wave

$$E_{in} = E_{0,in} e^{ik}, \quad (2)$$

where $k = 2\pi/\lambda$ is the wave number and $E_{0,in}$ is the amplitude of the field. We then consider E_{out} to be comprised of contributions for each roundtrip inside the cavity. This can be written as an infinite geometrical series given as

$$\begin{aligned} E_{out} &= tt' E_{0,in} e^{ik} + tt' E_{0,in} e^{ik} rr' e^{i\delta} \\ &\quad + tt' E_{0,in} e^{ik} (rr' e^{i\delta})^2 + tt' E_{0,in} e^{ik} (rr' e^{i\delta})^3 + \dots \\ &= tt' E_{0,in} e^{ik} \sum_{m=0}^{\infty} (rr' e^{i\delta})^m \end{aligned} \quad (3)$$

where $\delta = 2kl$. The first term of the series corresponds to a direct transmission through the cavity, and each term thereafter corresponds to the respective contribution to the transmission after the $m'th$ round trip.

By evaluating the series it is seen that it converges to the final expression for the transmitted field through a planar Fabry-Perot cavity

$$E_{out} = E_{0,in} \frac{tt' e^{i\delta/2}}{1 - rr' e^{i\delta}}. \quad (4)$$

The intensity of the transmission is now taken as the square of the norm of the field amplitude $|E_{out}|^2$ and normalizing with respect to the incident field intensity $|E_{0,in}|^2$. We arrive at an expression for the transmission intensity which is recognized to be given on the form of an *Airy function*[38]

$$T = \frac{|E_{out}|^2}{|E_{0,in}|^2} = \left| \frac{tt' e^{i\delta/2}}{1 - rr' e^{i\delta}} \right|^2 = \frac{(1 - |r|^2)(1 - |r'|^2)}{(1 - |rr'|)^2 + 4|rr'| \sin^2(\delta)}, \quad (5)$$

where δ is the phase shift associated with each round trip inside the cavity.

Figure 3 displays the Airy function in eq. (5), of a lossless cavity of reflectivities $r' = r$, as a function of δ in units of π . The function is plotted for the cases of $|r|^2 = 50\%$, shown in blue, and $|r|^2 = 90\%$, shown in red. It is readily seen that the transmission is maximized for $\delta = n2\pi$ and that the two cases shown differ significantly as the red profile is much narrower than the blue. The red profile

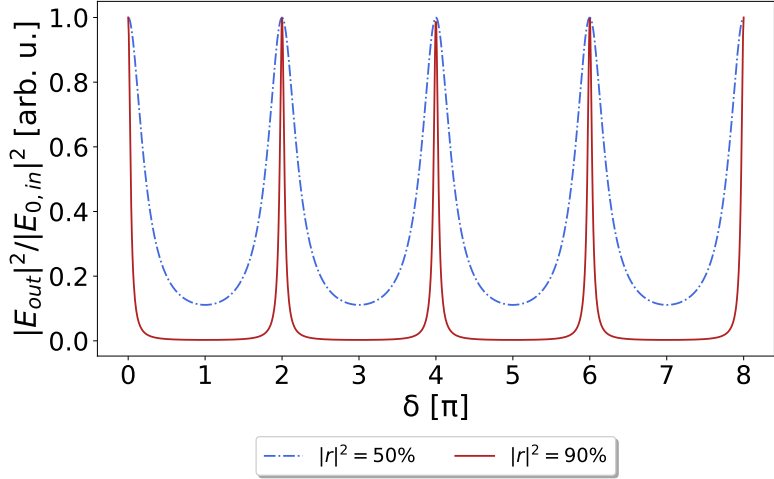


Figure 3: The red line shows the transmission spectrum of a *high* finesse Fabry-Perot cavity of reflectivity $|r|^2 = 0.90$, while the blue dashed line shows the transmission spectrum of a *low* finesse cavity with reflectivity $|r|^2 = 0.50$.

is hence said to have a higher *finesse* \mathcal{F} than the blue profile. The finesse is defined as

$$\mathcal{F} \equiv \frac{FSR}{\delta_\lambda}, \quad (6)$$

where *FSR* is the so-called *Free Spectral Range* indicating the spectral distance between two peaks and δ_λ refers to the *Full Width at Half Maximum (FWHM)* which, as the name suggests, is the linewidth defined at a normalized transmission $T = 1/2$, i.e. at half the maximum value.

Considering the Airy function in eq. (5) for the high finesse case where $|r|^2 = |r'|^2 \rightarrow 1$ we furthermore see that each individual peak closely resembles a Lorentzian distribution.

2.1.2 Varying the cavity length

In order to relate the resonance transmission profile to the length of the cavity we first consider the frequencies at which the cavity is resonant, with respect to the incident light, given as

$$\nu_n = n \frac{c}{2l}, \quad (7)$$

where c is the speed of light, n is a positive integer referring to the order of the resonance frequency and l is the cavity length. This corresponds to resonance

occurring at times related to each round trip inside the cavity.

Since the FSR is defined as the spectral distance between each peak, it follows from eq. (7) that it can be expressed in units of frequency as

$$FSR_\nu = \frac{c}{2l}, \quad (8)$$

and the corresponding linewidth, or FWHM, δ_ν is then given as

$$\delta_\nu = \frac{1}{2\pi} \frac{|t|^2 + |t'|^2}{\tau}, \quad (9)$$

where $\tau = 2l/c$ is the round trip time in seconds.

Finally, considering the definition of the finesse from eq. (6) it can be shown that

$$\mathcal{F} \equiv \frac{FSR_\nu}{\delta_\nu} = \frac{2\pi}{|t|^2 + |t'|^2}, \quad (10)$$

where the finesse is now defined in terms of the total cavity transmission at resonance.

Note here that the relation between the FSR and the cavity length l is clearly shown in eq. (8), and figure 4 furthermore shows transmission spectra underlining the effect of changing the cavity length.

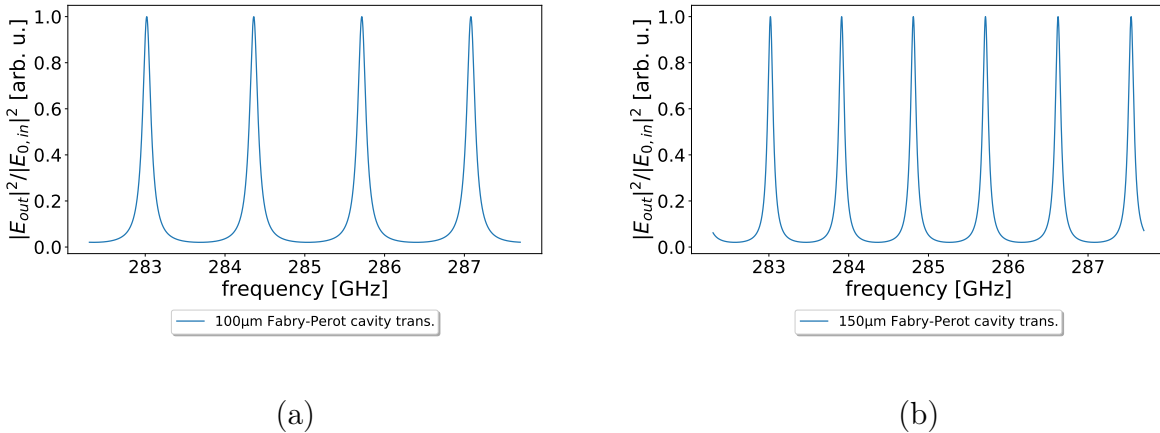


Figure 4: (a) shows the transmission spectrum of a Fabry-Perot cavity of length $l \approx 100\mu\text{m}$ as a function of the frequency ν , while (b) shows the transmission spectrum of a cavity of length $l \approx 150\mu\text{m}$ for the same range of frequencies. Note here how the FSR is inversely proportional to the cavity length.

2.1.3 Varying the incident wavelength

In order to simplify the Airy function in eq. (5) we introduce the so-called *coefficient of finesse* F , which is a function only of the mirror reflectivities, given as

$$F = \frac{4|rr'|}{(1 - |rr'|)^2}. \quad (11)$$

The coefficient of finesse F is not to be confused with the finesse \mathcal{F} . While the finesse is related to the sharpness of the transmission peaks, the coefficient of finesse refers to the contrast of the peaks in the sense that the difference between the minimum and maximum transmittance level increases with F . The coefficient of finesse is related to the finesse as

$$\mathcal{F} = \frac{\pi}{2}\sqrt{F}. \quad (12)$$

Rewriting the Airy function in terms of the coefficient of finesse yields

$$T_\lambda = \frac{1}{1 + F\sin^2(\delta/2)}, \quad (13)$$

where the round trip phase shift δ is related to the wavelength λ of the incident light by

$$\delta = 2kl = \frac{4\pi l}{\lambda}, \quad (14)$$

as $k = 2\pi/\lambda$ is the incident wave number.

Re-writing the general cavity brightness condition, it can easily be shown that the resonant wavelengths for a cavity at normal incidence are given as

$$\lambda_n = \frac{2l}{n}, \quad (15)$$

where $n = 1, 2, 3, \dots$ is a positive integer referring to the order of the resonance.

Since $\nu = c/\lambda$, the relation between the linewidth in wavelength space δ_λ and the one in frequency space δ_ν is non-linear. Therefore one does not simply make the aforementioned substitution in order to relate them. It can however be shown that their respective expressions differ by a factor of λ^2/c , and the linewidth when varying the wavelength is thus given as

$$\delta_\lambda = \frac{\lambda^2}{c} \cdot \delta_\nu = \frac{\lambda^2}{4\pi l}(|t|^2 + |t'|^2). \quad (16)$$

Finally we consider the definition for the finesse \mathcal{F} and the expression given in eq. (10), in order to show that the FSR in wavelength space is given as

$$FSR_\lambda \equiv \delta_\lambda \cdot \mathcal{F} = \frac{\lambda^2}{2l}. \quad (17)$$

Figure 5 shows an example of the Airy function given in eq. (13) as a function of the wavelength for a Fabry-Perot cavity of reflectivities $|r|^2 = |r'|^2 = 90\%$ and length $l = 100\mu m$.

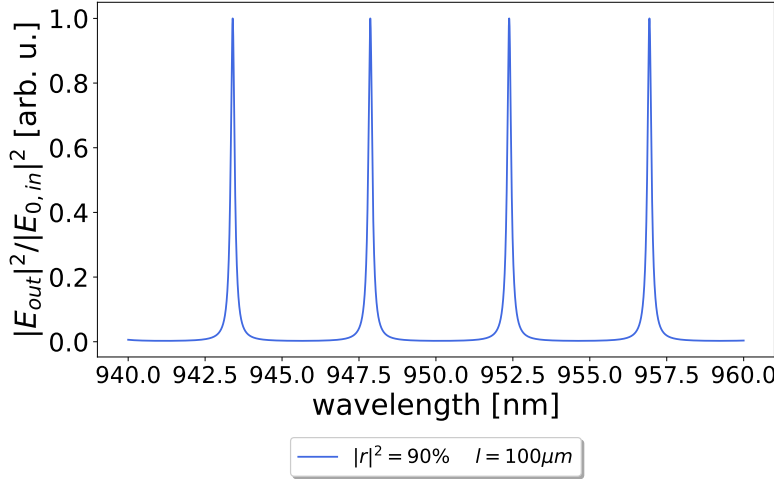


Figure 5: The Fabry-Perot transmission function on the form of an Airy function as seen in eq. (13) as a function of the incident wavelength.

2.1.4 Cavity losses

In eq. (10) we assume the case of a lossless cavity, i.e. eq. (1) is fulfilled. In practice, any cavity will have some amount of losses, which would have to be taken into account when calculating the finesse. When losses are present eq. (1) instead generally reads

$$|r|^2 + |t|^2 + L + L' = 1, \quad (18)$$

where L and L' indicates the fractional losses of each mirror.

In this case the finesse would be given as

$$\mathcal{F} = \frac{2\pi}{|t|^2 + |t'|^2 + L_{total}}, \quad (19)$$

where $L_{total} = L + L'$ are the total additional cavity losses.

The effect on the transmission spectrum of a cavity with losses is that the level of the normalized transmission will not reach unity, as some light is lost to e.g. absorption or scattering for each round trip of the cavity.

2.2 The Fano mirror: a sub wavelength grating

2.2.1 Reflection/transmission spectra and line shape analysis

2.2.2 Lossless grating

We wish to analytically describe the wavelength-dependent spectra for the transmission and reflectivity of an infinite sub-wavelength grating. The wavelength dependence arises from the fact that any incident light will be subject to interactions with the so-called *guided-mode* of the grating. The grating is, in this way, said to act as an effective TM_0 waveguide, ensuring resonant modes will only be reflected in the 0'th order.

By first considering the case where absorption and thermal coupling effects are neglected, i.e. a lossless grating, we can assume conservation of energy and thereby the relations

$$|r_g|^2 + |t_g|^2 = 1 \quad \text{and} \quad |r_d|^2 + |t_d|^2 = 1, \quad (20)$$

where the subscripts g and d indicate the *grating* and *direct* transmissions and reflectivities, respectively. It is implied that the direct coefficients are constants and describe the transmission and reflectivity when the incident wavelength is significantly detuned from any guided-mode resonance of the grating. Furthermore, it is also implied that the grating coefficients are functions of the incident wavelength.

We now assume a normal incident beam on the grating as a linearly polarized monochromatic plane wave, with a wavelength close to a guided-mode resonance of the grating. In order to describe the coefficients r_g and t_g we follow the formalism presented by Fan and Joannopoulos [33] and consider the likely paths of the incident light through the grating. It is quite intuitive to consider the case where the light is simply transmitted, and this shall be our first case hereafter denoted the *direct pathway*. Another case one might consider is the one where the incident light excites the guided-mode resonance in the grating. This case is denoted the *indirect pathway* and decays more slowly than its direct counterpart.

The interference caused when the guided mode is excited is often referred to as *Fano resonances*, due to its physical similarities to the description of interference between a discrete autoionized state and a bound continuum state first reported by Fano [39]. The cross section of inelastic scattering, when measured as a function of energy, showed characteristic asymmetric peaks. These were described as the aforementioned interference pattern between *direct* (the discrete state) and *indirect* (the continuum state) pathways.

By generalizing the model of Fan and Joannopoulos [33] we describe the transmission and reflectivity coefficient amplitudes as

$$r_g = r_d + \frac{a}{k - k_1 + i\gamma} \quad \text{and} \quad t_g = t_d + \frac{b}{k - k_1 + i\gamma}, \quad (21)$$

where $k = 2\pi/\lambda$ is the incident wave number, $k_1 = 2\pi/\lambda_1$ is the wave number according to the guided-mode resonance and γ is the HWHM (half width at half maximum) of the guided-mode resonance. Complex coefficients a and b describe the interference between the directly transmitted or reflected waves and the guided mode of the grating.

Note that in eq. (21) the right side of the expression for each coefficient corresponds to the continuum state i.e. the indirect pathway, while the direct transmission and reflection coefficients take the role of the autoionized discrete state, i.e. the direct pathway[39].

As we are dealing with an ideal, lossless, grating, we assume coefficients a and b to be equal, meaning that we specifically assume vertical symmetry throughout the grating. By considering eq. (20) this in turn leads to

$$a = b = -i\gamma(t_d + r_d), \quad (22)$$

which further yields an expression for the grating transmission amplitude coefficient on the form

$$t_g = t_d \frac{k - k_0}{k - k_1 + i\gamma}. \quad (23)$$

Here, the newly introduced $k_0 = 2\pi/\lambda_0 = k_1 - i\gamma(r_d/t_d)$ is the zero-transmission/unity-reflectivity wave number.

To generalize eq. (23) to include non-unity reflectivity and non-zero transmission, we allow for $a \neq b$ [40][41][42], meaning that the case of vertical asymmetry is

included in the model[43]. By assuming $r_d, t_d \in \mathbb{R}$, eq. (20) leads to the coupled differential equations

$$\begin{aligned} t_d x_a + r_d x_b &= 0, \quad \text{and} \\ x_a^2 + y_a^2 + x_b^2 + y_b^2 + 2t_d\gamma y_a + 2r_d\gamma y_b &= 0, \end{aligned} \tag{24}$$

where $\{x, y\}_{a,b}$ respectively denotes the real and imaginary parts of the coefficients a and b . Solving eqs. (24) leads to the correct complex reflectivity coefficients and the expression for the transmission coefficient amplitudes now reads

$$t_g = t_d \frac{k - k_0 + i\beta}{k - k_1 + i\gamma}, \tag{25}$$

where k_0 and β are defined from the expression for a found by solving eqs. (24), given as

$$a = t_d(k_1 - k_0 - i\gamma + i\beta). \tag{26}$$

Finally, this allows for non-zero transmission and non-unity reflectivity at wave number k_0 .

To show the validity of the model at this point, we introduce a periodic grating which is arbitrarily sketched in figure 6. The sketch indicates the period of the grating Λ , the top finger width w_t , the offset between the finger top and the bottom of the grating x , the total grating thickness t and finger depth d . Furthermore, the grating is patterned on a *silicon nitride (SiN)* membrane of refractive index n_{SiN} .

In order to simulate the transmission and reflectivity profiles as a function of the incident wavelength, we utilize the *Modeled Integrated Scatter Tool (MIST)* developed by the *National Institute of Standards and Technology (NIST)*[44]. The simulation solves Maxwell's equations for any pre-defined infinite periodic structure.

MIST assumes an incident plane-wave, and hence predicts the *ideal* spectra for the transmission and reflectivity, i.e. zero and unity when on resonance, respectively. In order to include effects related to the Gaussian behaviour of a more realistic incident beam, such as collimation and finite-size effects[45], one would have to solve Maxwell's equations for a Gaussian distribution. We safely assume an incident plane-wave for reasons related to the order of magnitude for the *Rayleigh range* of the beam used, compared with that of the spacial range of the conducted experiments.

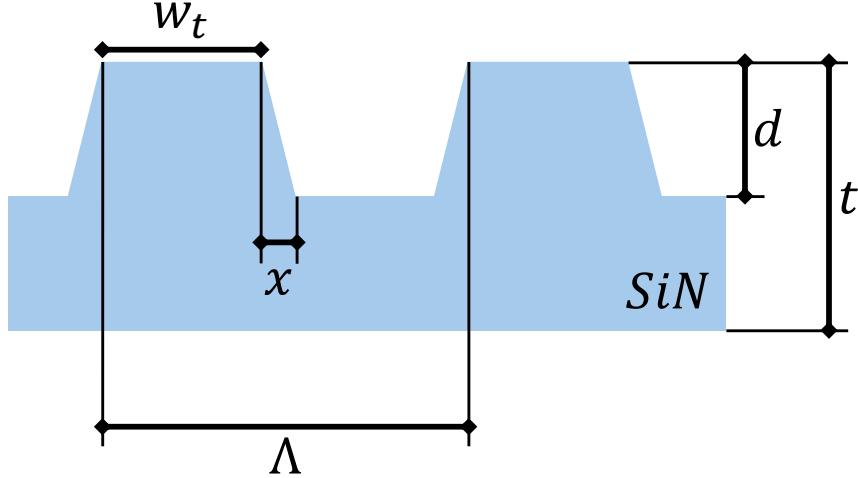


Figure 6: Schematics of a periodic optical SiN grating with physical parameters: $\Lambda = 857\text{nm}$, $w_t = 623\text{nm}$, $h = 55.1\text{nm}$, $t = 152\text{nm}$, $d = 67\text{nm}$, $n_{SiN} = 2.15$.

In reality, the interference inside the cavity however cannot be perfect, as any Gaussian beam can be represented by a number rays, infinitesimal in size, which would all track differently through the grating, resulting in non-unity reflectivity and non-zero transmission. In order to synthetically correct for this we scale each transmission value found by MIST according to

$$t_g = (1 - \varepsilon) \cdot t_{MIST} + \varepsilon, \quad (27)$$

where we define the correction to be arbitrarily small as $\varepsilon = 1\%$.

Figure 7 shows the scaled and unscaled results of the simulation using MIST for the following physical grating parameters:

$$\begin{aligned} \Lambda &= 857\text{nm}, \quad w_t = 623\text{nm}, \quad h = 55.1\text{nm}, \\ t &= 152\text{nm}, \quad d = 67\text{nm} \quad \text{and} \quad n_{SiN} = 2.15, \end{aligned} \quad (28)$$

The reflectivity- and (corrected) transmission values were then fitted to the model in eq. (25) using a least squares fitting method, and plotted along with the simulated values. The resulting grating parameters were found as

$$\begin{aligned} \lambda_0 &= 951.208\text{nm}, \quad \lambda_1 = 951.356\text{nm}, \quad t_d = 0.8094, \\ r_d &= 0.527, \quad \gamma_\lambda = 0.527\text{nm} \quad \text{and} \quad \beta = 4.42 \cdot 10^{-7}, \end{aligned} \quad (29)$$

where λ_0 is the cavity mode resonance wavelength, λ_1 is the guided-mode resonance wavelength, r_d (t_d) is the direct reflectivity (transmission), γ_λ is

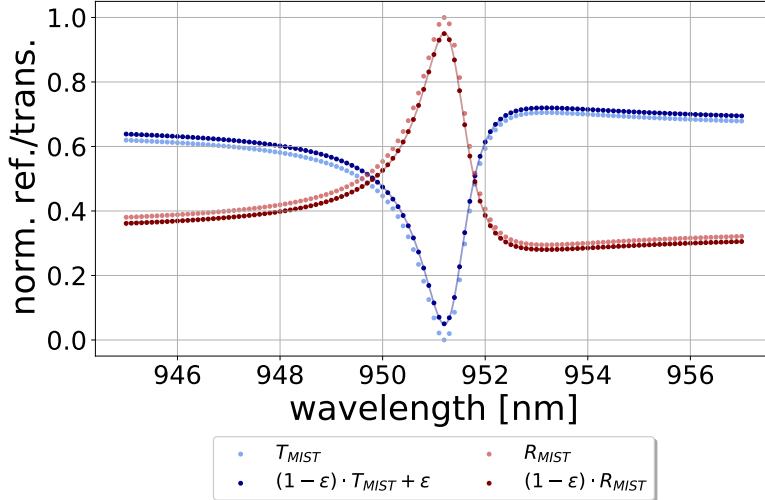


Figure 7: Reflectivity and transmission values (scaled and unscaled) found from a MIST simulation plotted with the corresponding least squares fit to the model in eq. (25). The resulting grating parameters are given as $\lambda_0 = 951.217\text{nm}$, $\lambda_1 = 951.356\text{nm}$, $t_d = 0.818$, $r_d = 0.527$, $\gamma_\lambda = 0.527\text{nm}$, and $\beta = 1.03 \cdot 10^{-6}$.

the width of the guided-mode resonance and β is a constant associated with non-unity reflectivity and non-zero transmission.

2.2.3 Lossy grating

In order to modify the above model such that losses, e.g. due to absorption or thermal coupling effects, are accounted for, we add a resonant loss term to the energy conservation relation in eq. (20). For this we introduce the resonant loss level L , which must be known in order to accurately calculate the complex reflectivity coefficients. The energy conservation relation is modified such that

$$|t_g|^2 + |r_g|^2 + \frac{c^2}{(k - k_1)^2 + \gamma^2} = 1, \quad (30)$$

where the coefficient $c^2 = L((k - k_1)^2 + \gamma^2)$ includes the resonant loss term L . A new set of coupled differential equations are found, using eq. (30), given as

$$\begin{aligned} t_d x_a + r_d x_b &= 0, \quad \text{and} \\ x_a^2 + y_a^2 + x_b^2 + y_b^2 + c^2 + 2t_d \gamma y_a + 2r_d \gamma y_b &= 0. \end{aligned} \quad (31)$$

It is easily identified that eq. (24) and eq. (31) differ only by the addition of coefficient c^2 , and thereby the losses. Solving eq. (31) leads to the correct

complex reflectivity coefficients, except that they now account for any losses associated with the grating.

In conclusion, the complete grating model consists of an expression for the transmission coefficients and a set of coupled differential equations for the reflection coefficients, shown in eq. (25) and eq. (31), respectively. The model on the form used for this project and subsequent thesis is derived in previous work by A. Darki et al. [46] and more recently T. Mitra et al. [35].

Figure 8 shows reflection and transmission spectra of a grating of parameters given in eq. 29 with a synthetic non-zero resonance loss term in order to show the effect of including losses. It is seen from the added *loss curve* that the losses increase when approaching the resonance wavelength, as the interaction with the guided-mode, and thus the grating, gets stronger in this region.

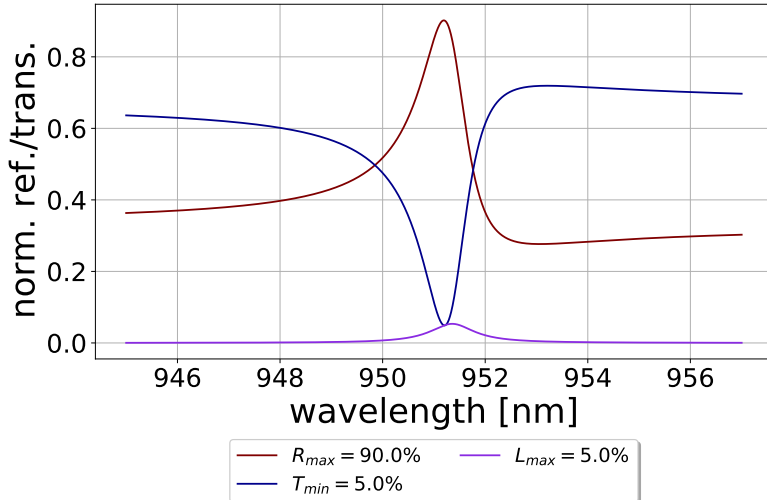


Figure 8: Simulated reflectivity and transmission spectra of a grating of parameters given in eq. (29) with a synthetically added non-zero resonant loss term. The purple line indicate the corresponding grating losses.

2.3 The single Fano cavity

2.3.1 The single Fano cavity model

The single Fano cavity consists of a planar broadband mirror, and a sub-wavelength grating, i.e. a Fano mirror, as described in section 2.2 and seen in figure 9 where schematics of the single Fano and broadband cavity configurations

are shown. While the broadband mirror has fixed optical properties, the Fano mirror has transmission and reflection coefficients dependent on the incident wavelength, according to solutions to the coupled differential equations of eq. (31).

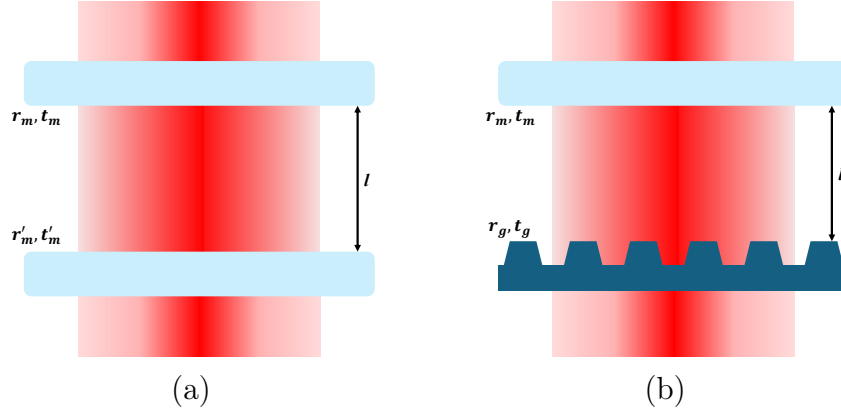


Figure 9: In (a) is seen the schematics of a cavity consisting of two broadband mirrors with transmission and reflectivity coefficients t_m , r_m , t'_m , and r'_m . (b) shows the schematics of a single Fano cavity consisting of one broadband mirror with coefficients t_m , r_m and one Fano mirror with wavelength dependent coefficients t_g , r_g . The reflectors in either cavity are separated by a cavity length l .

In order to model the single Fano cavity transmission spectra, we therefore consider the transmission function of a normal incident and planer Fabry-Perot cavity in eq. (4) with $r, t \rightarrow r_m, t_m$ and $r', t' \rightarrow r_g(\lambda), t_g(\lambda)$ [47]. Here the subscript m indicates the broadband *mirror* coefficients, and g is for *grating*, which indicates the coefficients of the Fano mirror. Rewriting eq. (4) such that it describes the normalized transmission amplitude, through the single Fano cavity, $T_{cav} = |E_{out}|^2/|E_{0,in}|^2$ we get

$$T_{cav} = \left| \frac{t_m t_g(\lambda) e^{i\phi}}{1 - r_m r_g e^{2i\phi}} \right|^2, \quad (32)$$

where $\phi = 2\delta = kl$, $k = 2\pi/\lambda$ and l is the cavity length, as is consistent with the general case described in section 2.2.

2.3.2 Transmission linewidth

We aim to analytically describe how the transmission spectrum at, or close to, the overall resonance behaves as a function of the incident wavelength. The

overall resonance is the term used for the case of $\lambda_g \approx \lambda_c \approx \lambda_l$, where g, c, l stands for grating/guided-mode, cavity and laser, respectively, and the Fano model is hence generalized for this specific scenario. Considering the case where the cavity resonance closely resembles the guided-mode resonance of the Fano mirror (the zero-transmission wavelength), eq. (32) can be approximated well by

$$T_{cav} \approx \frac{A}{1 + \left(\frac{\Delta}{1-\nu\Delta}\right)^2}, \quad (33)$$

where $\Delta = (\lambda - \lambda_c)/\delta\lambda$ is the detuning from the cavity resonance normalized by the HWHM $\delta\lambda$, and ν is a constant describing the asymmetry of the single Fano transmission spectrum. [35][46]

From eq. (33) it can be shown that the HWHM of the Fano transmission profile around the overall resonance wavelength, i.e. when $\lambda_c \approx \lambda_0$, is approximately given as

$$\delta\lambda \approx \frac{1}{\frac{1}{\delta\lambda_c} + \frac{1}{\delta\lambda_g}}, \quad (34)$$

where

$$\delta\lambda_c = \frac{\lambda_0^2}{8\pi l} (|t_g(\lambda_0)|^2 + |t_m|^2 + L) \quad (35)$$

is the HWHM of a broadband cavity and

$$\delta\lambda_g = \frac{\gamma\lambda}{2(1-r_d)} (|t_g(\lambda_0)|^2 + |t_m|^2 + L) \quad (36)$$

is the HWHM of the Fano cavity in the so-called Fano regime.[35][46] In eqs. (34)-(36) λ_0 is the Fano cavity resonance wavelength, l is the cavity length, $L = (1 - |r_g(\lambda_0)|^2 - |t_g(\lambda_0)|^2)$ is the total additional losses of the cavity when on resonance, $\gamma\lambda$ is the width of the guided-mode resonance of the Fano mirror and r_d is the off-resonance, or *direct*, reflectivity of the Fano mirror.

The *Fano regime* and its counterpart the so-called *standard regime* are defined for a given single Fano cavity, by its length l . By inspection of eqs. (35) and (36) it is seen that for $l \rightarrow \infty$ the linewidth in eq. (34) is dominated by the broadband cavity term, while for the opposite case, $l \rightarrow 0$, the linewidth is predominantly given by the Fano cavity term.

Generally the Fano regime describes the cavity lengths for which eq. (34) shows a significant divergence from the broadband linewidth in eq. (35). Oppositely,

when in the standard regime the broadband and Fano cavity produces resonance transmission peaks of comparable, if not equal, linewidths.

We now introduce a single Fano cavity consisting of the Fano mirror introduced in section 2.2 and sketched in figure 6, and a broadband mirror of reflectivity $|r|^2 = 90\%$ and transmission $|t|^2 = 1\%$. Figures 10a and 10b depicts examples of the transmission spectra in the standard and Fano regimes together with their respective complimentary broadband cavity transmission profiles. The reflectiviy amplitude of the Fano mirror is shown in both figures.

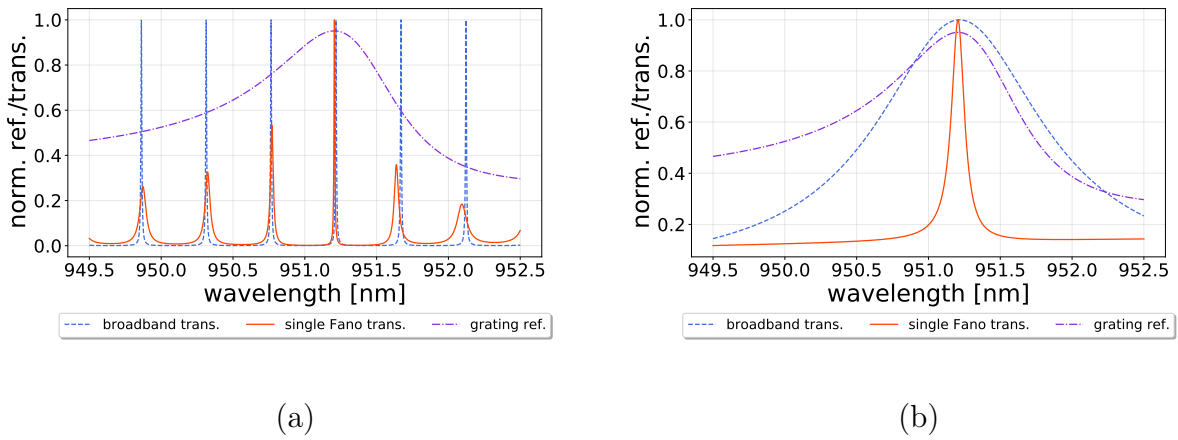
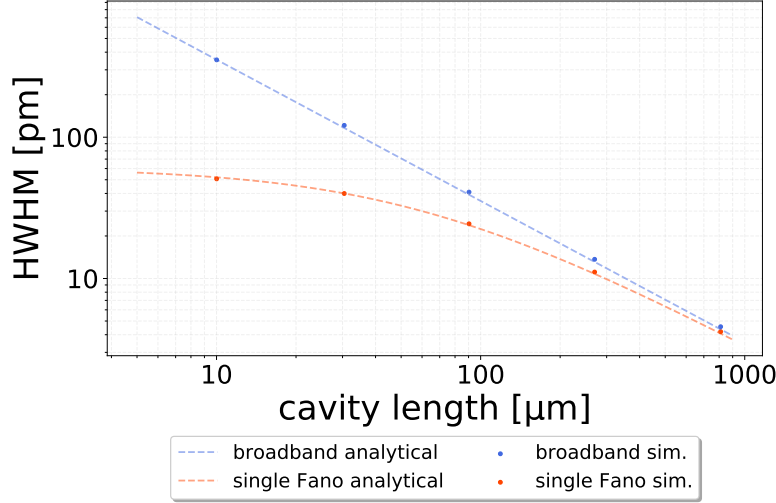


Figure 10: In (a) is seen the comparison of broadband and single Fano cavity transmission spectra for a cavity length of $l \approx 1000\mu\text{m}$, i.e. in the *standard* regime. (b) shows the same comparison, but for a cavity length of $l \approx 5\mu\text{m}$, i.e. in the so-called *Fano* regime.

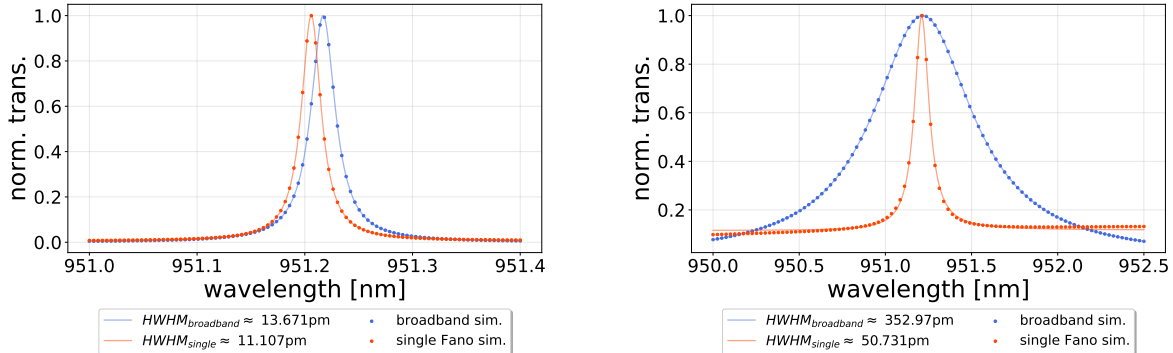
Figure 10a shows the transmission spectra of the two cavities for a length of $l \approx 1000\mu\text{m}$, i.e. in the standard regime. It is clear from inspection of the figure that the resonance transmission profile of the standard broadband cavity is not wavelength dependent, in the sense that all fringes appear to have the same high finesse \mathcal{F} , i.e. ratio between the FSR and HWHM. This is not the case for the Fano cavity which is due to the wavelength dependence of the optical properties of the Fano mirror, as this causes the transmission and reflectivity to *only* match those of the broadband mirror when on resonance. Furthermore, no significant difference in linewidth is seen for the transmission of the two cavities on resonance, as predicted by eq. (34).

In figure 10b, the transmission spectra of both cavities are shown for a length of $l \approx 5\mu\text{m}$, i.e. in the Fano regime. Here it is clearly seen that while the standard

cavity, as expected, experiences broadening for shorter cavity lengths, this is not the case for the Fano cavity transmission peak.



(a)



(b)

(c)

Figure 11: (a) shows the approximate analytical resonance linewidths (eq. (34)) as a function of cavity length for the broadband and single Fano cavities together with linewidths of transmission profiles simulated using eq. (32) and eq. (4), found as parameters of least squares fits, for comparison. In (b) and (c) is seen transmission spectra of broadband and single Fano cavities of lengths $\sim 270\mu\text{m}$ and $\sim 10\mu\text{m}$, respectively. The spectra shown indicate each their respective linewidths, and are examples of the values plotted in (a).

Figure 11a models the behavior of the linewidth of the single Fano cavity compared with the one for a broadband cavity of similar optical properties, as a

function of wavelength. Here it is easily seen where the linewidth of the single Fano transmission begins to saturate, and hence deviate from the one of the broadband cavity. The plotted line in the figure is calculated using eq. (34) while the points depict linewidths found as a fitting parameter from a least squares fit of the general Fano model in eq. (33) to transmission spectra simulated by the Fabry-Perot (eq. (4)) and single Fano (eq. (32)) transmission functions. Finally, it can be concluded that the approximate analytical expression for the linewidth of the broadband and single fano cavities in eq. (34) correlates very well with the values found from the simulated spectra.

2.4 The double Fano cavity

2.4.1 The double Fano cavity model

While the single Fano cavity is usually known in the appropriate litterature as simply a *Fano cavity*, I have insisted on including the fact that it contains only one Fano mirror, and hence denoted it the *single* Fano cavity. This addition is justified by the contents of this section, and namely that we now move on to the *double* Fano cavity, which as the name suggests consists of two Fano mirrors. The schematics of this configuration is shown together with the one for the single Fano cavity in figure 12.

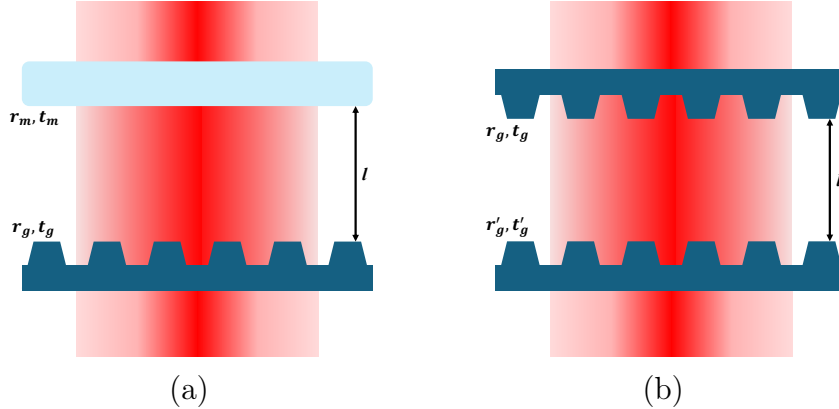


Figure 12: (a) shows schematics of the single Fano cavity consisting of a broadband mirror with transmission and reflectivity coefficients t_m , r_m and a Fano mirror with coefficients t_g , r_g . (b) shows the schematics of the double Fano cavity consisting of two Fano mirrors with coefficients t_g , r_g , t'_g , r'_g . Both cavities are separated by a cavity length l .

Here it is evident that instead of having one set of reflectivity and transmission coefficients that depend on the incident wavelength, we now have two. In order

to model the transmission of the double Fano cavity, we once again consider the transmission function for the normal incident and planar Fabry-Perot cavity in eq. (4), this time with $r, t \rightarrow r_g(\lambda), t_g(\lambda)$ and $r', t' \rightarrow r'_g(\lambda), t'_g(\lambda)$ [47]. We rewrite the Fabry-Perot transmission function with the addressed substitutions of the optical coefficients and such that it describes the normalized transmission amplitudes $T_{cav} = |E_{out}|^2/|E_{0,in}|^2$ and get

$$T_{cav} = \frac{t_g(\lambda)t'_g(\lambda)e^{i\phi}}{1 - r_g(\lambda)r'_g(\lambda)e^{2i\phi}}. \quad (37)$$

The subscript g indicates a grating transmission or reflectivity.

We now introduce a double Fano cavity consisting of two identical Fano mirrors, each as sketched in figure 6 in section 2.2, and thus with optical parameters given in eq. (29). Figure 13 shows an example of the normalized transmission spectrum of this double Fano cavity on- and off-resonance for a cavity length of $l \approx 30\mu m$. The spectrum was found using eq. (37).

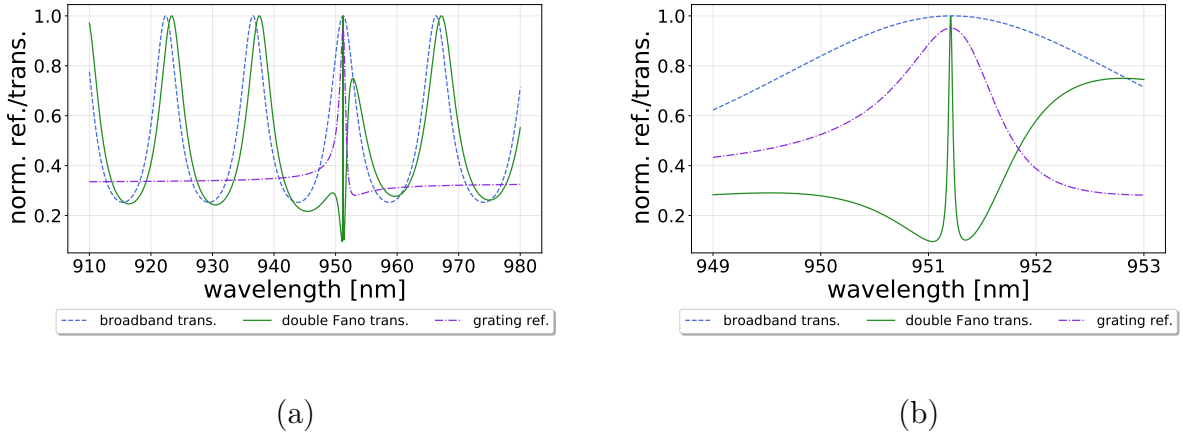


Figure 13: An example of a normalized double Fano transmission spectrum of a cavity of length $l \approx 30\mu m$. (a) shows a long-range wavelength scan, depicting both the on- and off-resonance behaviour of the double Fano cavity transmission. Note that the broadband cavity transmission for a cavity of optical properties given by the direct reflectivity r_d and direct transmission t_d of the Fano mirror is shown. It is readily seen that the resonance peak is placed on a "background" consisting of this function, displaced by a small phase. (b) shows the transmission focussed specifically around the resonance wavelength. Both examples are shown together with the reflectivity of the Fano mirror used to model them.

2.4.2 Transmission linewidth

In order to describe the analytical linewidth of the transmission profile of the double Fano cavity, we take a similar approach as in the single Fano case outlined in section 2.3.2. It can be shown from eq. (34) when including the wavelength dependence of the optical coefficients of both Fano mirrors, that the HWHM $\delta\lambda$ of the double Fano cavity transmission profile is approximately given as

$$\delta\lambda^{double} \approx \frac{1}{\frac{1}{\delta\lambda_c} + \frac{1}{\delta\lambda_g^{double}}}, \quad (38)$$

where

$$\delta\lambda_c = \frac{\lambda_0^2}{8\pi l}(|t_g(\lambda_0)|^2 + |t'_g(\lambda_0)|^2 + L) \quad (39)$$

is still the HWHM of a broadband cavity and

$$\delta\lambda_g^{double} = \frac{\gamma\lambda}{4(1 - r_d)}(|t_g(\lambda_0)|^2 + |t'_g(\lambda_0)|^2 + L). \quad (40)$$

is the HWHM of the double Fano cavity in the Fano regime. Note that $\delta\lambda^{double} = \delta\lambda^{single}/2$ for $l \rightarrow 0$ when eq. (38) is predominantly given by eq. (40). In this brief evaluation of the estimated analytical linewidth of the double Fano transmission profile it is assumed that all defining parameters of the two Fano mirrors are identical, except for the cavity and guided-mode resonance wavelengths $\lambda_{0,1}$. Namely the following relevant parameters are assumed identical,

$$r_d = r'_d \text{ and } \gamma\lambda = \gamma\lambda'. \quad (41)$$

In this way any spectral detuning of the two Fano mirrors used to make a cavity is included in the analytical expression. The spectral detuning, and the effect hereof, will be further described in section 2.4.5.

2.4.3 Single and double Fano cavity comparison

Using the analytical expression for the double Fano cavity transmission in eq. (38) we are now in a position to compare the single and double Fano cavities. Note that we at this point only consider the ideal case of the double Fano cavity where additional cavity losses are neglected and the two Fano mirrors used are identical, i.e. the cavity is said to be *symmetrical*. The additional cavity losses are explicitly set to be given as

$$L = 1 - |r_g|^2 - |t_g|^2 = 0. \quad (42)$$

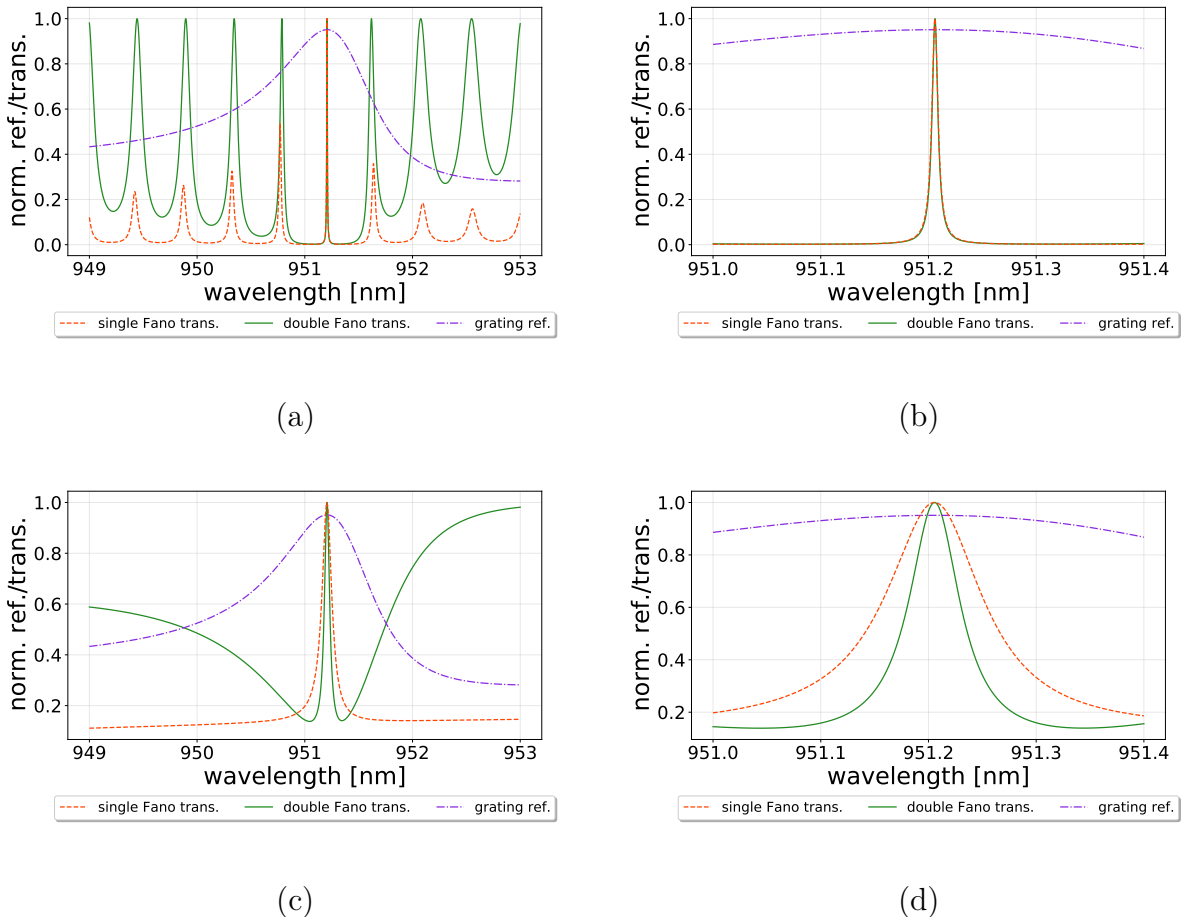


Figure 14: Comparison of the single and double Fano transmission spectra in the *standard* and *Fano* regimes. (a) and (b) shows the spectral comparison for a cavity of length $l \approx 1000\mu\text{m}$, i.e. in the *standard* regime, while (c) and (d) shows the same for a cavity of length $l \approx 5\mu\text{m}$, i.e. in the *Fano* regime. (b) and (c) show spectra zoomed around the resonance peak, and the Fano mirror reflectivity is depicted in all figures.

Figure 14 shows the transmission of the ideal double Fano cavity and the corresponding single Fano cavity for comparison.

Figures 14a and 14b shows the transmission for a cavity length of $l \approx 1000\mu\text{m}$ which is well-inside the standard regime outlined in section 2.3.2, where the standard, broadband and single Fano cavities produce transmission spectra of roughly identical linewidths. In this regime, due to the $1/l$ proportionality of the FSR, the off-resonance behavior of the double Fano cavity transmission is visible in the range plotted. It is seen, contrary to the single Fano cavity, that the transmission at each cavity resonance reaches a normalized transmission of

$|E_{out}|^2/|E_{0,in}|^2 = 1$. This is due to the fact that the two Fano mirrors, while they have wavelength dependent transmission and reflectivity coefficients, always have identical ones for the ideal case. This maximizes the Fabry-Perot transmission function and ensures unity transmission at any cavity resonance. The minimum level of the cavity changes according to the coefficient of finesse, and thus only the Fano mirror reflectivity, hence the HWHM also changes as we move further from the guided-mode resonance. Both the minimum transmission level and the HWHM converge when moving away from the resonance wavelength, when $r \rightarrow r_d$ becomes constant.

Figures 14c and 14d shows the transmission of a double Fano cavity of length $l \approx 5\mu m$, i.e. well within the Fano regime. It is seen that the double Fano cavity transmission produces a resonance peak with a HWHM narrower than the one for the single Fano cavity, as is predicted in eq. (40). Furthermore, the immediate off-resonance behavior of the double Fano cavity transmission in the Fano regime, is drastically different than for the single Fano cavity. This is due to the collective higher transmission in this region compared with the single Fano case where the broadband mirror has a constant, and often high, reflectivity and hence a correspondingly low transmission.

Figure 15a shows the analytical linewidth calculated and compared for the broadband, single Fano, and double Fano cavities, calculated using eqs. (35), (34), (38). These are compared with linewidths found as fitting parameters from a least squares fit of the general Fano transmission formula given in eq. (33) to transmission spectra calculated using eqs. (4), (32), and (37). According to eq. (38) the linewidth of the double Fano cavity transmission should converge to exactly half that of the single Fano cavity, meaning that

$$\delta\lambda_{double} = \frac{\delta\lambda_{single}}{2}, \quad \text{for } l \rightarrow 0. \quad (43)$$

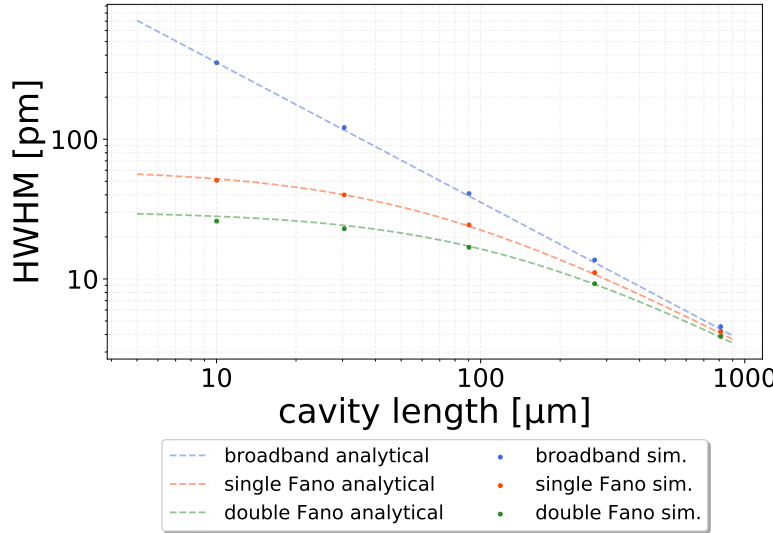
This is supported well by the simulation depicted in figure 15a.

Figures 15b and 15c contain examples of transmission spectra of single- and double Fano cavities and corresponding least squares fits to the general Fano model in order to determine their linewidths.

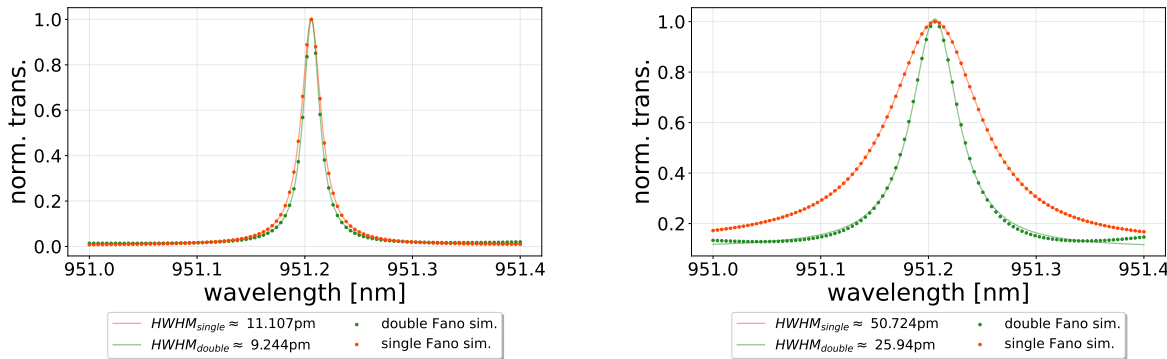
2.4.4 Additional cavity losses

Thus far we have only examined a lossless double Fano cavity where

$$|r_g|^2 + |t_g|^2 = 1 \quad (44)$$



(a)



(b)

(c)

Figure 15: (a) shows the analytical resonance linewidths (eqs. (34), (38), and (35)) as a function of the cavity length for the broadband, single and double Fano cavities together with linewidths of corresponding profiles simulated using eqs. (32), (37), and (4) for comparison. In (b) and (c) is seen transmission spectra of single and double Fano cavities of lengths $l \approx 270\mu m$, and $l \approx 10\mu m$, respectively. The spectra shown indicate each their respective linewidths, and are examples of the values plotted in (a). Note however, that the broadband cavity peak has been left out of (b) and (c).

is fulfilled for both Fano mirrors used to construct the cavity.

In this section we will investigate what happens when we introduce *additional* cavity losses, not to be confused with the often used definition of cavity losses

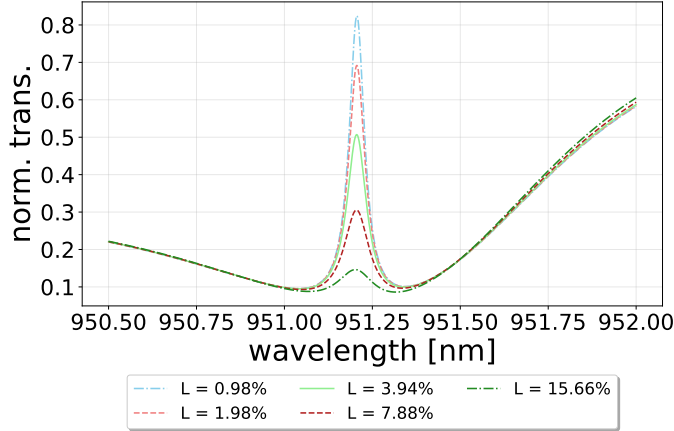


Figure 16: Resonant transmission spectra for different values of the additional resonant loss term L , of a symmetric double Fano cavity of length $l \approx 30\mu m$.

defined as $L = 1 - |r|^2$ where anything not being reflected back into the cavity is considered as "losses". Additional cavity losses, as described in this section, is given as

$$L = 1 - |r_g|^2 - |t_g|^2, \quad (45)$$

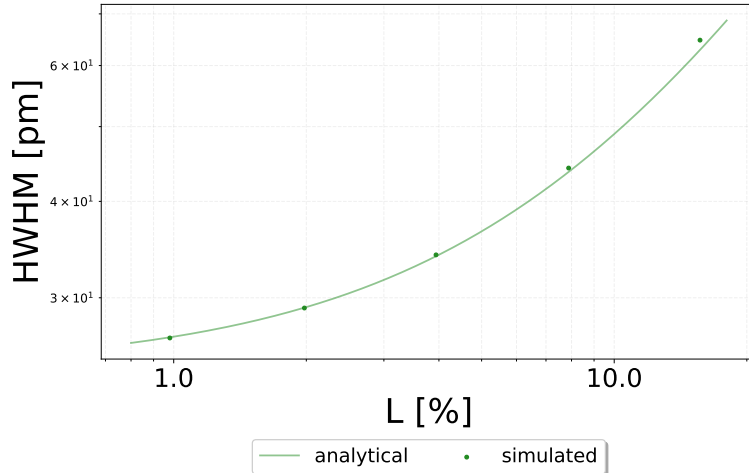
leading to the modified conservation condition

$$|r_g|^2 + |t_g|^2 + L = 1. \quad (46)$$

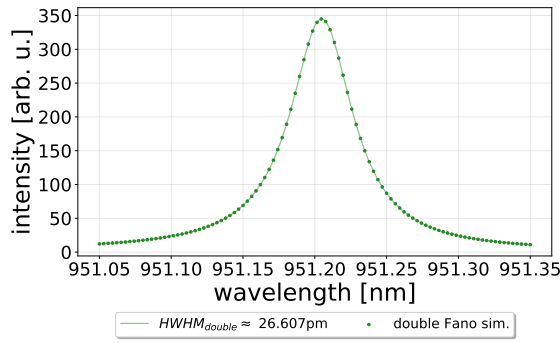
Figure 16 shows double Fano transmission spectra for a symmetric cavity with varying values for the additional cavity losses. It is readily seen that the maximum value reached in each spectrum is rapidly reduced with the introduction of these losses.

Since the linewidth is defined as the HWHM of the transmission profile, this will naturally vary as a function of additional cavity losses. This is depicted in figure 17a where the HWHM is shown for different values of L . Examples of transmission spectra taken for different values of L are shown in figures 17b and 17c, along with their respective least squares fits to the general Fano model in eq. (33) and linewidths found as fitting parameters hereof.

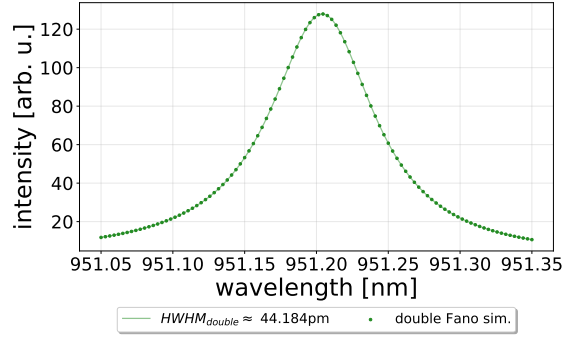
Figure 17a shows the simulated linewidths of resonance transmission spectra as a function of the total additional cavity losses L , and is compared with the analytical formula for the double Fano linewidth in eq. (38).



(a)



(b)



(c)

Figure 17: (a) shows the linewidth (HWHM) of a symmetric double Fano cavity of length $l \approx 30\mu m$ as a function of additional cavity losses $L = 2(1 - |r_g|^2 - |t_g|^2)$. Each point is found as a fitting parameter of a least squares fit of the double Fano intracavity spectrum for a certain value of L to the general Fano model. The plotted line indicates the analytical value of the linewidth (eq. 34) as a function of L , for comparison. In (b) and (c) are seen examples of double Fano transmission spectra, with their respective linewidths, for cavities of $L = 1\%$ and $L = 8\%$, respectively.

2.4.5 Spectral detuning (lossless)

Up until this point, it has been assumed that the Fano mirrors making up the double Fano cavity has been identical, namely the cavity has been *symmetrical*.

However, in practice this is very unlikely to be the case, as any Fano mirror constructed is bound to have some uncertainties attached to the physical parameters describing it (see eq. (28)). For that reason we investigate the effect of an *assymmetric* cavity on the resulting transmission profile. Here we remember that each Fano mirror is described by a set of parameters, λ_0 , λ_1 , t_d , $\gamma\lambda$ and β , which respectively describe the cavity resonance wavelength, guided-mode resonance wavelength, direct transmission, guided-mode resonance linewidth and additional losses of each grating. In order to model only a spectral detuning, we therefore simply change the parameters regarding the cavity and guided-mode resonance wavelengths, λ_0 and λ_1 by an amount corresponding to the detuning we wish to study. For this section the parameters will be given by the ones for the Fano mirror sketched in figure 6, and thus given in eq. (29) for the unchanged Fano mirror, and

$$\begin{aligned}\lambda'_0 &= \lambda_0 + \Delta, \quad \lambda'_1 = \lambda_1 + \Delta, \quad t'_d = t_d, \\ \gamma\lambda' &= \gamma\lambda \quad \text{and} \quad \beta' = \beta\end{aligned}\tag{47}$$

for the *detuned* Fano mirror, where Δ is the detuning given by $\Delta = |\lambda_0 - \lambda'_0|$. Figure 18 shows the normalized reflectivity and transmission spectra of the unchanged Fano mirror (eq. (29)) and the detuned Fano mirror (eq. (47)) for a detuning of $\Delta = 0.3\text{nm}$.

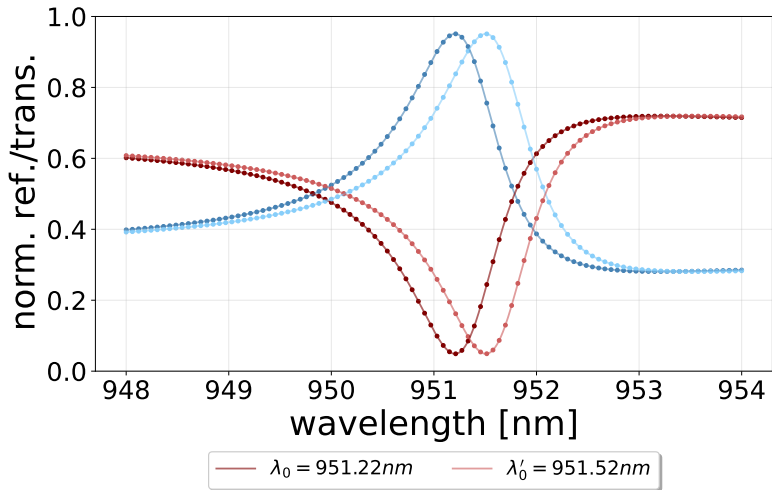


Figure 18: The normalized reflectivity and transmission spectra of the Fano mirrors described in eqs. (29) and (47) for detuning $\Delta = 0.3\text{nm}$.

As has been observed in previous sections, the Fano resonance transmission

peak is present at the point where the grating reflectivity $r_g(\lambda)$ is maximized and transmission $t_g(\lambda)$ minimized. However, when $\lambda_0 \neq \lambda'_0$ and $\lambda_1 \neq \lambda'_1$, this is no longer a trivial conclusion to draw. The question of whether the cavity resonance should be tuned to match the guided-mode resonance wavelength of one grating or the other, or maybe somewhere in between does not have an obvious answer. This will be further expanded upon later in section 2.4.6, but in order to move forward with the investigation of the spectral detuning we, for now, accept that the optimal cavity length, is the one corresponding to a cavity resonance λ_t given, exactly between the two guided-mode resonance wavelengths, as

$$\lambda_t = \frac{\lambda_0 + \lambda'_0}{2}. \quad (48)$$

Where t is for *transmission* as this is, later on, to be used experimentally as the *transmission wavelength*.

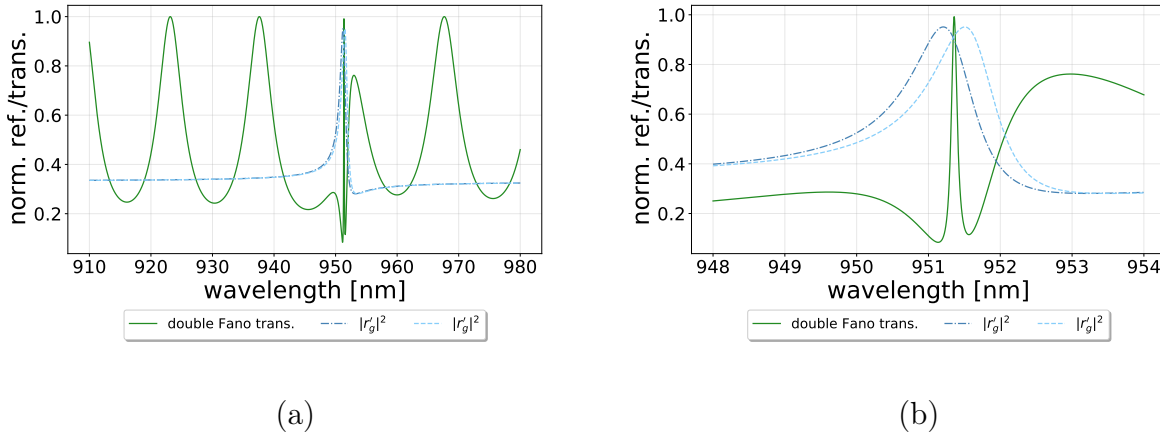


Figure 19: The double Fano transmission spectra of a cavity of length $l \approx 30\mu m$ and detuned by $\Delta = 0.3\text{nm}$, as seen in figure 18, together with the reflectivity spectra of the Fano mirrors used for the simulation.

Figure 19 shows the transmission spectrum of a detuned double Fano cavity with parameters corresponding to the transmission and reflectivity spectra in figure 18, meaning that $\Delta = 0.3\text{nm}$. The transmission wavelength λ_t is chosen such that eq. (48) is fulfilled, and correspondingly it is seen that the transmission peak is placed exactly between the maximum (minimum) reflectivities (transmissions) of the two grating, i.e. between the two guided-mode resonance wavelengths. Furthermore, it can be concluded that the detuning is chosen such that the overlap between the guided-mode resonances is still substantial enough for them to couple and hence for the overall Fano resonance to be excited.

While knowing that a detuning of 0.3nm is acceptable in terms of exciting the Fano resonance in the lossless case is a nice result, it does not provide much in terms of estimating the acceptable detuning for any experimental purposes. In figure 20a the double Fano transmission is shown for increasing detuning Δ and transmission wavelength $\lambda_t = (\lambda_0 + \lambda'_0(\Delta))/2$.

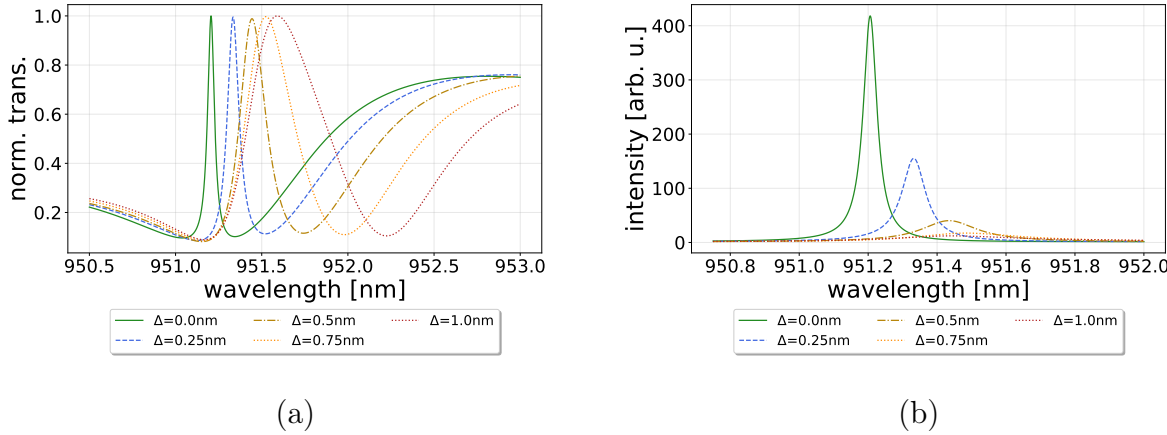


Figure 20: In (a) is seen lossless double Fano transmission spectra for increasing value of the detuning $\Delta = |\lambda_0 - \lambda'_0|$. It is readily seen that the transmission wavelength $\lambda_t = (\lambda_0 + \lambda'_0)/2$ becomes higher, and that the linewidth likewise becomes larger with increasing detuning. (b) shows the intracavity spectra corresponding to the transmission spectra in (a) normalized by each their maximum value, shown in (c), in order to preserve readability.

It is readily seen that with increasing positive detuning, relative to the resonant wavelength of the unchanged Fano mirror, the peak shifts to higher wavelengths, which in itself is easily seen from eq. (48). The linewidth is also seen to increase with the detuning, and the peak will eventually collapse when the overlap between the guided-mode resonance profiles of the two Fano mirrors becomes too small to sustain the Fano resonance. This collapse was seen for examples of higher losses, and will be evident in later sections. Figure ?? shows the intracavity spectra corresponding to the transmission spectra in figure 20a normalized by their respective maximum values plotted in figure ?? in order to preserve readability. The intracavity spectra provides valuable insight into the mode density inside the cavity for the different values of Δ , and considering the significant difference of $\propto 10^4$ in the maximum value for the intensity, a mode density decrease is, though qualitative, clearly shown by figure ??.

It is clearly demonstrated by figures 20a, ?? and ?? that the spectral overlap

is a very crucial parameter of the double Fano cavity, and is paramount in describing the cavity's ability to produce narrow Fano resonant structures.

2.4.6 Spacial detuning (lossless)

As mentioned above in section 2.4.5, any spectral detuning gives rise to the potential of a spacial detuning as $2l = m\lambda$ must be fulfilled for any sustained plane-wave mode inside a normal incident optical cavity. We denote the length corresponding to the resonance wavelength of the unchanged Fano mirror as simply l , while the one for the detuned Fano mirror will be denoted as l' . Previously we assumed that the optimal length of a detuned double Fano cavity is the one where the so-called transmission wavelength is given as

$$\lambda_t = \frac{\lambda_0 + \lambda'_0}{2}. \quad (49)$$

And while this does turn out to be a good empirically justified assumption in the experimental part of this project, we will model and investigate the resonant length-dependence of the linewidth of the Fano resonance profile.

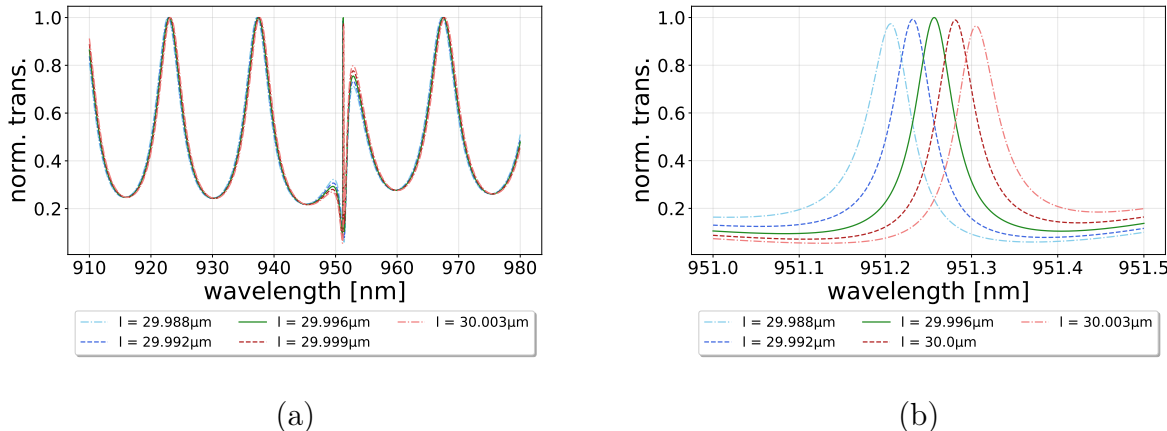


Figure 21: (a) shows lossless long-range transmission spectra of double Fano cavities of lengths $l \rightarrow l' \approx 30\mu\text{m}$ with $\Delta = 0.1\text{nm}$. (b) shows the same spectra as seen in (a), zoomed in on the range around the transmission wavelength λ_t .

Figure 21 shows double Fano resonance transmission profiles plotted for varying cavity length $l \rightarrow l'$ with detuning $\Delta = 0.1\text{nm}$. The long range wavelength scan in figure 21a shows a well-defined off-resonance behavior, as the detuning is barely visible on this scale, while the peak height on resonance is already visibly affected. The immediate off-resonance spectra also shows visible changes

as the peak "background" level depend heavily on the location of the overall resonance.

Figure 21b shows the same spectra, but enhanced around the resonance wavelength. This shows that the substantial guided-mode overlap, and thus small detuning, is enough to detect significant changes in the resonance spectra. The shifting of the peak position is evident, but the most prominent change is seen in the peak height, which is reduced from 1 when $\lambda_t = (\lambda_0 + \lambda'_0)/2$ to around 0.8 when $\lambda_t = \lambda_0$ or $\lambda_t = \lambda'_0$.

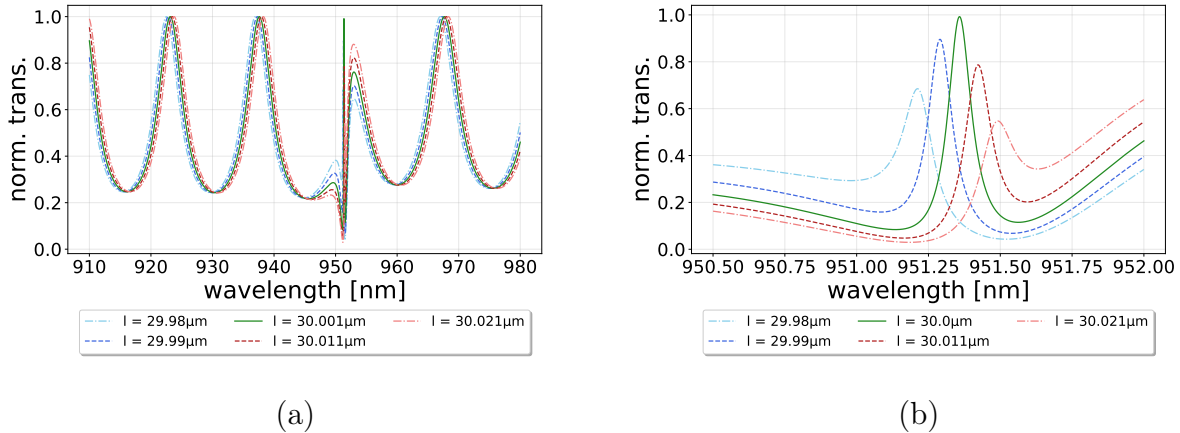


Figure 22: (a) shows lossless long-range transmission spectra of double Fano cavities of lengths $l \rightarrow l' \approx 30\mu\text{m}$ with $\Delta = 0.3\text{nm}$. (b) shows the same spectra as seen in (a), zoomed in on the range around the transmission wavelength λ_t .

Figure 22 shows similar transmission profiles as in figure 21, only with an increased detuning of $\Delta = 0.3\text{nm}$. Looking at the long range scan in figure 22a and comparing with the one in figure 21a, it is seen that the displacement of the off-resonance Fabry-Perot like fringes have increased with the slightly higher detuning. This is not surprising as the Fabry-Perot cavity modes, like any other interference pattern inside a cavity must fulfill the brightness identity $2l = m\lambda$. Furthermore, the immediate off-resonance regime shows an increase in the intensity displacement when compared with the less detuned example.

Figure 22b, which shows the spectra enhanced around the resonance position, provides a more detailed image of what happens to the transmission profiles as a function of the cavity length. Here it is seen that the peaks at the edges of the length interval have varied even more in shape, height and linewidth than in figure 22b. In short, the increased detuning has also increased the fractional length-dependence of the double Fano cavity transmission profile. Here it must

however be noted here that the range in which the cavity length is scanned is increased with the detuning. So the length-dependence is fractional in the sense that the step size is here defined by the size of the interval.

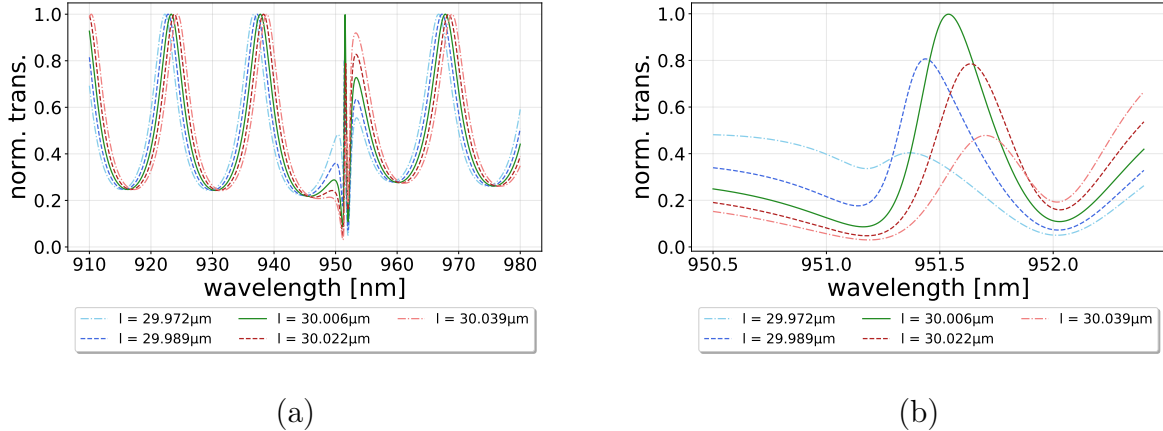


Figure 23: (a) shows lossless long-range transmission spectra of double Fano cavities of lengths $l \rightarrow l' \approx 30\mu\text{m}$ with $\Delta = 0.8\text{nm}$. (b) shows the same spectra as seen in (a), zoomed in on the range around the transmission wavelength λ_t .

Figure 23 shows the effect of a relatively large detuning of $\Delta = 0.8\text{nm}$. This is simply included for a visual representation of a detuning which is considered "too large" for any practical use. The long range scan in figure 23a shows that the Fabry-Perot like fringes are now even more displaced, and figure 23b showing the spectra enhanced around the resonance wavelength shows roughly the same trend as in figure 22b, only that this example is greatly broadened in comparison. It is though noted, that while broadened, the Fano resonance mode is sustained even for the relatively large detuning.

In order to get a clear qualitative picture of the double Fano cavity transmission profile as a function of both cavity length and wavelength, we visualize the varying of both in a heat map and let the color indicate the transmission intensity. This is shown in figure 24 which depicts a lossless cavity of length $l \approx 30\mu\text{m}$ and detuning $\Delta = 0.3\text{nm}$. Here the movement of the resonance peak as a function of the cavity length is clearly seen as a slope of the "line" representing the high intensity region due to the Fano resonance.

Considering only the heat map, it is not easily visible which cavity length is the optimal one, however, the *magenta*, *cyan*, and *limegreen* lines across the heat map indicate slices which are depicted separately in figure 25. It is seen by analysing the transmission profiles of the three cavities of specific lengths,

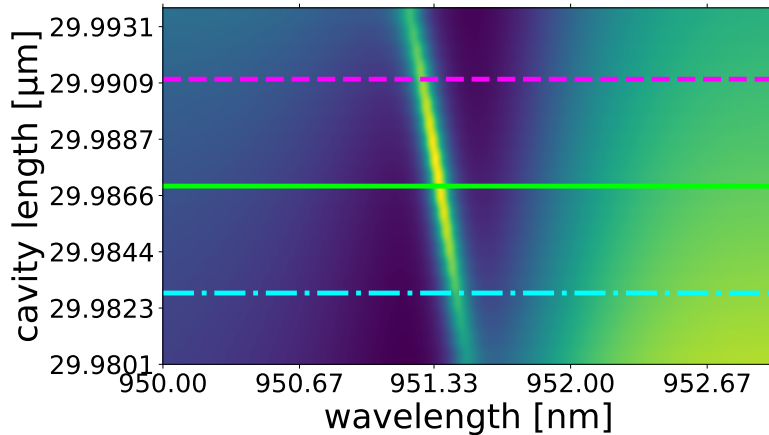


Figure 24: Heat map of the lossless double Fano cavity transmission as a function of wavelength and cavity lengths ranging $l \rightarrow l' \approx 30\mu m$ for $\Delta = 0.3\text{nm}$

how they vary in both position and linewidth. The lengths and corresponding linewidths are given as

$$\begin{aligned} l_{magenta} &= 0.2l + 0.8l' \rightarrow HWHM_{magenta} = 40.5pm \\ l_{cyan} &= 0.8l + 0.2l' \rightarrow HWHM_{cyan} = 31.9pm \\ l_{lime} &= (l + l')/2 \rightarrow HWHM_{lime} = 29.7pm. \end{aligned} \quad (50)$$

It turns out that of the three cases, the *lime* transmission profile seems optimal as it is the narrowest of the three, and seems to be more preferably positioned, i.e. it is more centered in and thus separated from the Fabry-Perot-like background.

This trend is further examined in figure 26 where the linewidths of intracavity spectra are shown as a function of the cavity length. The parameters used are the same as in figure 24 and the figure indicates that the optimal cavity length is definitely "somewhere in between" the two guided-,mode resonance lengths. However, it is also evident that the previous assumption for λ_t is too simple to be general in this case.

As a visual and qualitative representation of the effect of increasing the detuning Δ , figure 27 shows heat maps similar to the one in figure 24, but for a range of values for the detuning $\Delta = 0.01\text{nm} \rightarrow \Delta = 1.21\text{nm}$. It is readily seen that the aforementioned slope of the high intensity region, indicating the resonance peak, increases with the detuning. This is a representation of the peak moving to higher wavelengths, both for the optimal transmission wavelength and for the

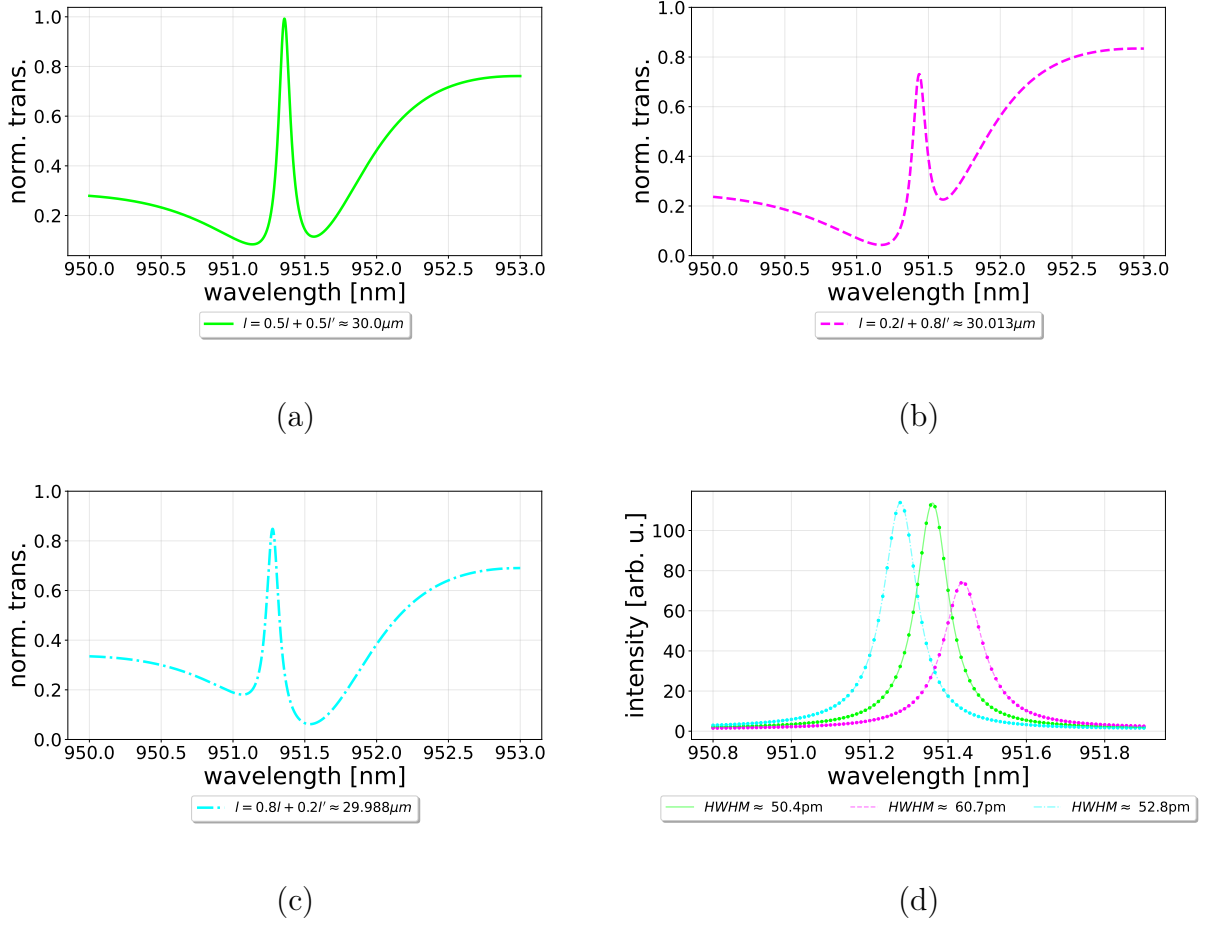


Figure 25: (a), (b) and (c) show slices of the heat map in figure 24 indicated by their respective color and line type in order to compare different cavity lengths. (d) shows intracavity spectra of the peaks in (a), (b) and (c) with corresponding least squares fits and linewidths found as parameters hereof.

one closer to the detuned Fano mirror guided-mode resonance. The broadening of the peak is also displayed in a way that is, while only qualitative, convincing.

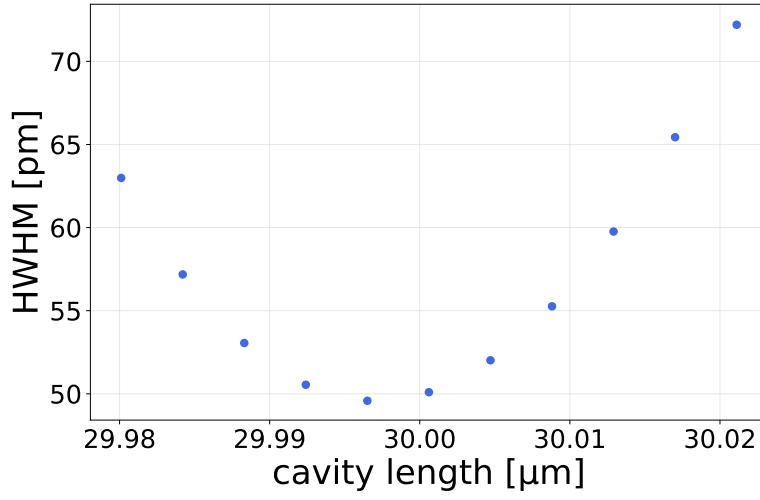


Figure 26: Linewidth as a function of cavity length $l \rightarrow l'$. Each point is found as a fitting parameter from a least squares fit to the generalized Fano model in eq. (33) of lossless intracavity double Fano spectra.

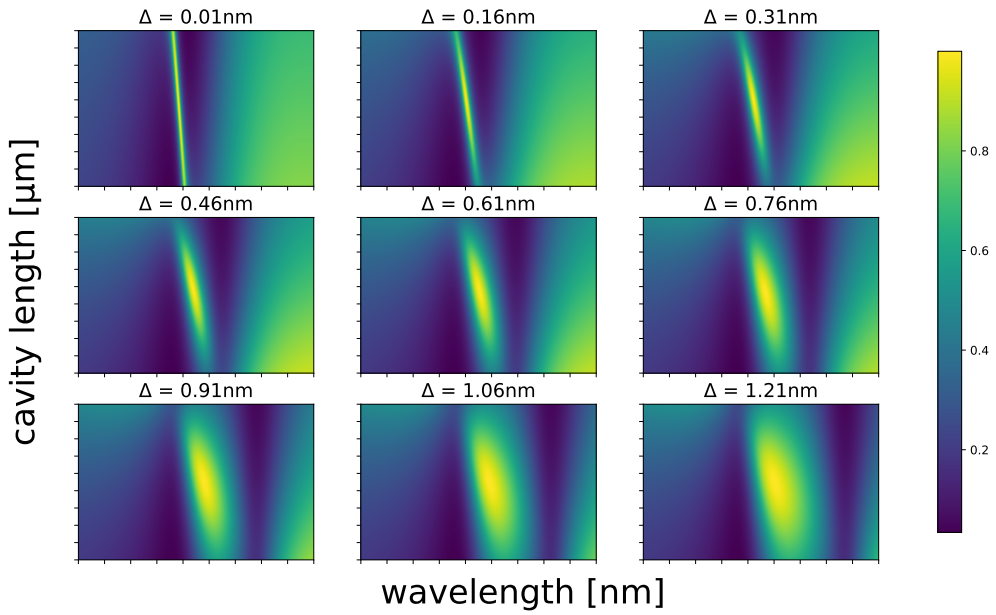


Figure 27: Series of heat maps showing lossless double Fano transmission spectra as a function of the cavity length, for increasing detuning Δ .

3 Method

3.1 The experimental setup

The experimental setup used to optically characterize the Fano mirrors, single- and double Fano cavities is illustrated in figure 28. The specific part of the setup surrounding the cavity, outlined by the dashed line in figure 28, is subsequently shown in figure 29a.

In order to effectively conduct the experiments in this project, it is imperative to be able to control certain parameters. Each element in the experimental setup is thoroughly considered for each their purpose in this regard, these will be outlined in this section.

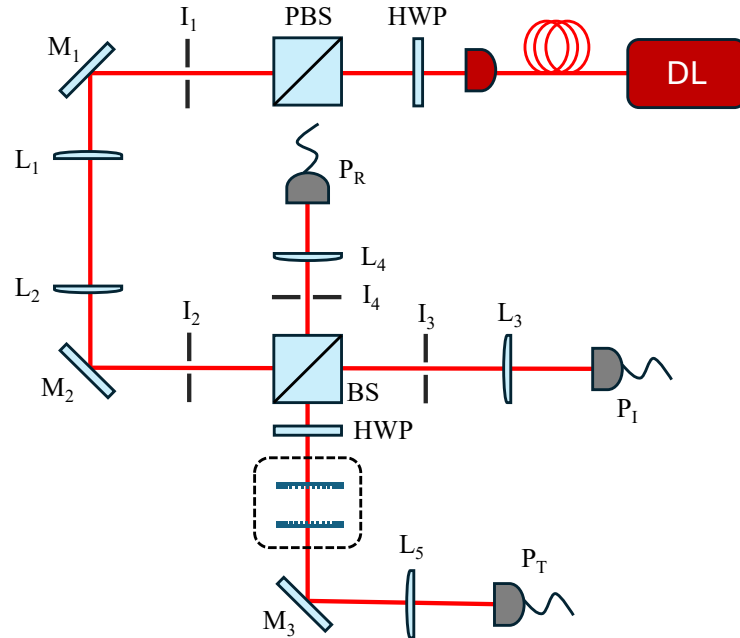


Figure 28: Schematics of the experimental setup for measuring Fano cavity transmission- and Fano mirror transmission/reflection spectra. The diode laser DL emits light into the setup through the optical fiber, the $\lambda/2$ -waveplate HWP and polarizing beam splitter PBS ensures the light is linearly polarized and the optical telescope consisting of lenses $L_{1,2}$ modifies the beam waist to fit the given purpose. Detectors $P_{T,R,I}$ records the transmitted, reflected and incident light, respectively and the second HWP makes it possible to tune the polarization of the light just before the light is incident on the Fano cavity/mirror. The dashed line indicates the cavity setup seen in detail in figure 29. I_{1-4} and M_{1-3} indicate apertures/iris' and mirrors, respectively.

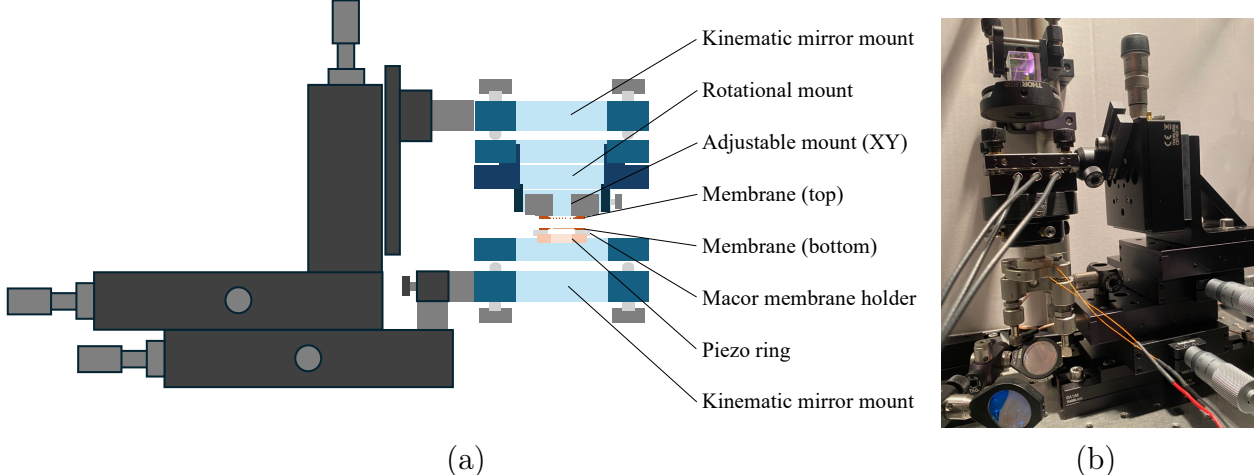


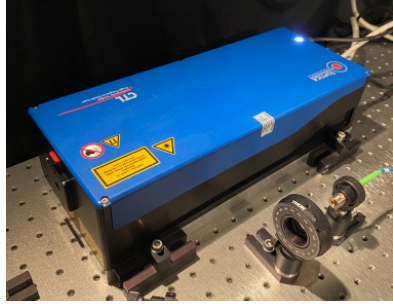
Figure 29: (a) shows a sketch of the schematics of the Fano cavity setup located inside the dashed line in figure 28. The stages attached to both the top and bottom of the cavity are used to spatially align the Fano mirrors of the cavity, while the kinematics mirrors are used to adjust for the angular degrees of freedom. The piezo ring is used to scan for and tune the optimal length of the cavity and the rotational and adjustable xy-mounts are used for aligning the top of the cavity, when the bottom is aligned with respect to the laser, and both are hence fixed. (b) shows a picture of the cavity setup depicted schematically in (a). Note that the setup, both in (a) and (b), depicted is the one used to measure double Fano cavity transmission, and would thus be modified for a Fano mirror characterization.

3.1.1 Tunable diode laser

As shown in figure 28 the laser source used for the optical characterizations is coupled into the setup through an optical fiber. The laser used is a *Toptica DLC Pro* tunable CW diode laser with a range for the transmission wavelength of $910 - 980\text{nm}$. The laser and controller are both depicted in figure 30. The optical fiber is a *P3-780PM-FC-10* fiber from Thorlabs which is a single mode¹ polarization-maintaining optical fiber with an effective range of $770 - 1100\text{nm}$. Between the Toptica laser and the incoupling end of the fiber, a $\lambda/2$ -plate (HWP) and *polarizing beam splitter* (PBS) is placed in order to be able to control the incident power of the laser and to only couple linearly polarized light into the setup.

The light being emitted from the optical fiber is sent through another HWP

¹A single mode fiber can only sustain the TEM00 mode, which means that the output is known to be perfectly Gaussian.



(a)



(b)

Figure 30: The Toptica DLC Pro tunable CW diode laser (a) and the controller (b) used to tune the wavelength of the output beam.

and PBS in order to be able to control the resulting polarization in the setup even more precisely, should there be any discrepancies of the light coupled into the fiber. The out-coupling fiber with the HWP and PBS is shown in figure 31.

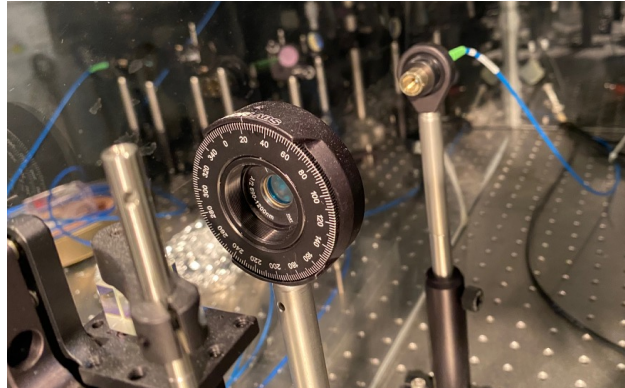


Figure 31: The out-coupling end of the P3-780PM-FC-10 polarization maintaining optical fiber from Thorlabs along with the HWP and PBS ensuring linear polarized light incident on the cavity or Fano mirror.

3.1.2 $\lambda/2$ - waveplate

A $\lambda/2$ -waveplate, or HWP, is constructed of a so-called bi-refringent material (most commonly crystalline quartz), which means that it has slightly different refractive indices for incident light of different polarization axis'. Generally a HWP will have a *fast-* and *slow axis*, where it is understood that light polarized along the fast axis experiences a lower refractive index (and hence moves faster), than that along the slow axis. In this way the HWP separates the components of unpolarized light that has perpendicular and parallel polarizations with respect to the fast axis.

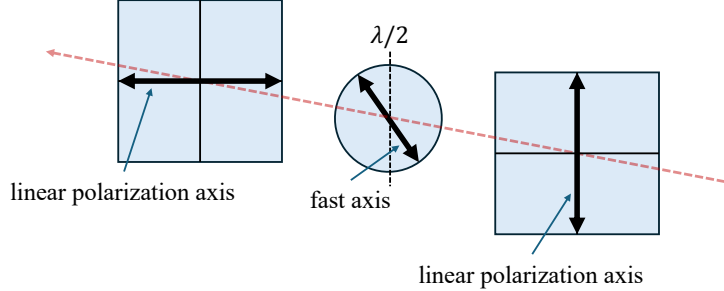


Figure 32: A simple sketch of the effect of a HWP on linearly polarized light.

The effect of the HWP on linearly polarized light, is an effective rotation of the polarization axis, this is sketched simply in figure 32. It can be shown that the polarization axis is rotated according to the angle between the fast axis of the HWP and the incident polarization axis. A relative angle θ will thus result in a rotation of 2θ , e.g. if $\theta = 45^\circ$, this will constitute a rotation from completely p-polarized light to completely s-polarized light. This is the specific scenario sketched in figure 32[48]. In this way a rotating HWP can allow one to alter an incident linearly polarized beam to be polarized along any axis, and is thus a necessary component for this particular setup.

3.1.3 Optical telescope

The linearly polarized light transmitted through the PBS passes through plano-convex lenses of positive focal lengths f and f' , L_1 and L_2 , which together makes up an optical telescope used to manipulate the beam waist w_0 incident on the cavity or Fano mirror.

Figure 33a shows schematics of the general way an optical telescope is utilized to manipulate the beam waist of a laser beam.

When the incident beam hits L_1 it is focused according to its focal length f , and by inserting another lens L_2 of a relatively longer focal length one can *catch* the beam at the desired beam waist. If the focal length f' of L_2 is sufficiently long, compared to the path of the beam after the lenses, the beam will be approximately collimated and remain at the waist obtained when incident on L_2 .

3.1.4 Transmission, reflection and incident photo-detectors

After passing the optical telescope the beam reaches a simple 50/50 beam splitter (BS) which transmits 50% of the light while reflecting another 50%. The

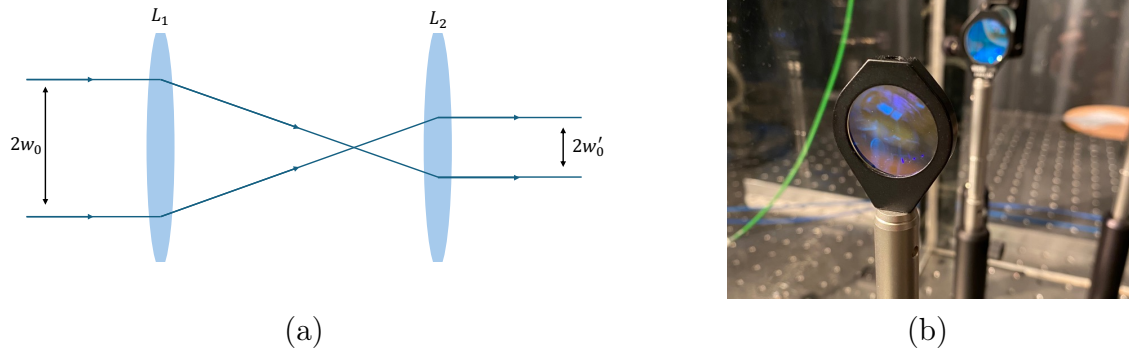


Figure 33: (a) shows simple schematics of an optical telescope used to alter the waist of an incoming collimated beam, while (b) shows a picture taken of the actual optical telescope used in the setup.

reflected light is then incident on the cavity or Fano mirror (target).

The transmitted light passes through a lens L_3 , which is focused on a photodetector P_I used for reference measurements and later normalization. Since the tunable laser in nature varies in power with the wavelength, it is necessary to keep track of these fluctuations and correct for them in data analysis.

The transmitted light is sent through, yet another, HWP which in this case is used only to alter the polarization of the light incident on the target. After the beam, or a portion of it, has passed the target it is sent through a lens L_5 focused onto the transmission detector P_T .

The part of the light incident on the target that is *not* transmitted, is reflected back onto the BS which then transmits 50% once again, and thus reflects the other 50%. The transmitted part here is focused through the lens L_4 onto the reflection detector P_R .

3.1.5 The double Fano cavity measurement setup

The cavity measurement setup shown in figure 29a is the one used to measure the transmission spectrum of a double Fano cavity consisting of two Fano mirrors. This part of the setup consists of two sets of standard $PT1 \mu\text{m}$ -stages from Thorlabs combined to provide precise movement of each Fano mirror in the xy-plane.

Examining the structure from the bottom (as it is built), a kinematic mirror mount is attached to the lower set of xy-stages, this is used to control the angular degrees of freedom of the Fano mirror which makes up the bottom of the cavity.

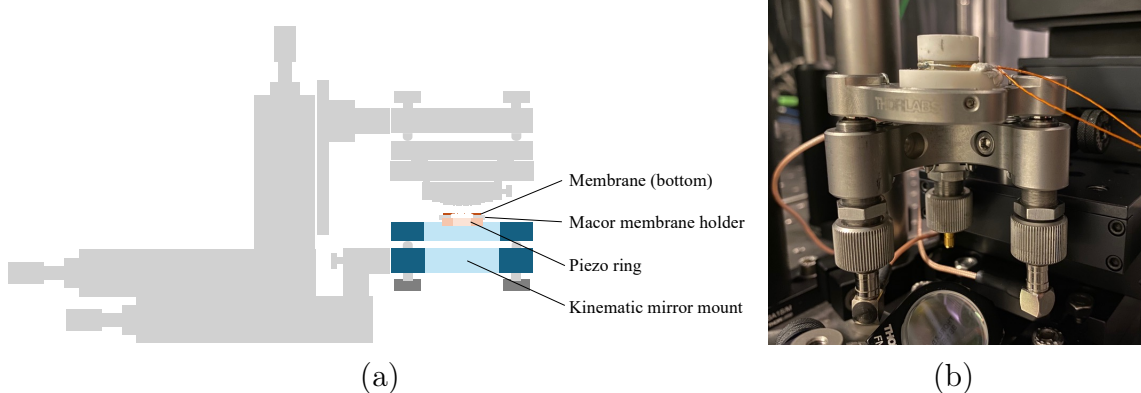


Figure 34: (b) shows a picture taken of the *bottom* part of the double Fano cavity setup, while (a) depicts the corresponding schematics.

On the mirror mount, a *NAC2123* piezo ring actuator from Noliac is firmly attached and connected to a piezo driver. The driver is capable of applying a fixed current, and thus manually controlling the piezo expansion, but is also connected to a frequency generator. The signal from the frequency generator can be used to modulate the piezo expansion by an alternating current, which practically scans the cavity length in a range according to the effective free stroke of the piezo ring². Lastly, in order to be able to place the Fano mirror on the piezo ring, a ceramic Macor membrane holder is used. The bottom part of the cavity setup is highlighted in figure 34a.

The part of the setup built to control the Fano mirror making up the top of the cavity is slightly more complicated, as this is the Fano mirror that is, for practical reasons, aligned last. This means that additional degrees of freedom must be controlled by movement of the Fano mirror itself. The alignment procedure will be explained in detail in sections 3.2 and 3.3.

The top part of the cavity setup is attached to the second set of xy-stages and additionally to an *NFL5DP20* stage from Thorlabs in the z-direction in order to be able to change the length of the cavity. As for the bottom part of the cavity setup, a kinematic mirror mount acts as the base of the construction. This is, once again, to control the angular degrees of freedom of the corresponding Fano mirror. This mirror mount is equipped with piezo elements to control the angular degrees of freedom, by applied voltage, with higher resolution than for

²The NAC2123 piezo ring has an outer/inner diameter of 12mm/6mm and a height of 2mm. Its listed free stroke is $3.3\mu m$, which practically is likely slightly limited in the configuration used. To obtain the precise free stroke one can simply count the number of fringes resolved during one period as the length-dependent FSR is known to be $\lambda/2$.

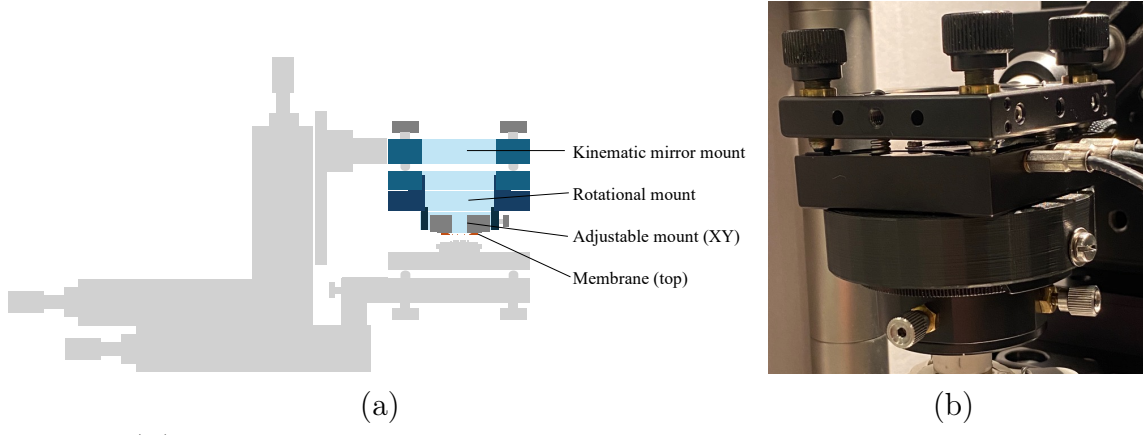


Figure 35: (b) shows a picture taken of the *top* part of the *double Fano cavity* setup, while (a) depicts the corresponding schematics.

the manual adjustments. On the mirror mount, a standard rotational mount with a 1 inch inner winding is attached in order to be able to control the rotational degree of freedom of the Fano mirror. An additional xy-adjustable mount is then used in order to effectively place the Fano mirror in the center of the rotational mount to ensure the rotational axis is in the center of the membrane. Finally, the Fano mirror is taped to a costume mount created to fit into the xy-adjustable mount. The top part of the cavity setup is highlighted in figure 35a, and presented separate from the setup to show how the Fano mirror is attached in figure 36.

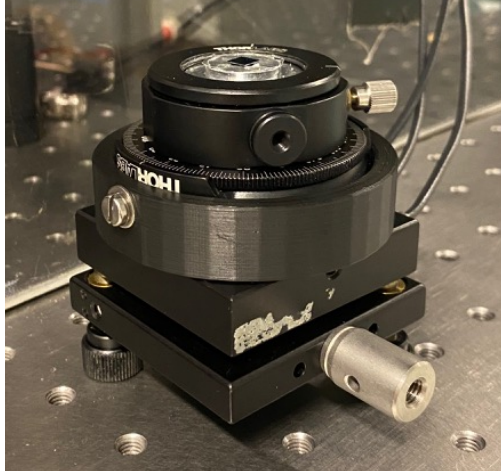


Figure 36: The top part of the cavity setup separated from the rest and flipped. Note that the Fano mirror attached with the tape is shown. The three wires visible are then ones that connect the piezo elements with a driver.

What has been outlined here is the setup utilized to optically characterize the double Fano cavity. If one wishes to do so for the single Fano cavity instead,

the setup would be modified such that the top part of the setup, highlighted in figure 35a, would only consist of the kinematic mirror mount. Inside the mirror mount would then be placed a broadband mirror. The rotational- and xy-adjustable mounts would here be redundant due to the rotational symmetry of any standard broadband mirror.

3.1.6 Vibrational noise reduction

When the cavity measurements were conducted it was apparent that the double Fano cavity was particularly prone to noise. While noise is not a very precise definition in its own, it did seem that the most prominent source was associated with the length of the cavity l . When applying a constant voltage to the piezo element depicted in figure 34, in order to achieve the correct length for sustaining the Fano resonance, the level started to fluctuate dramatically when approaching the resonance.

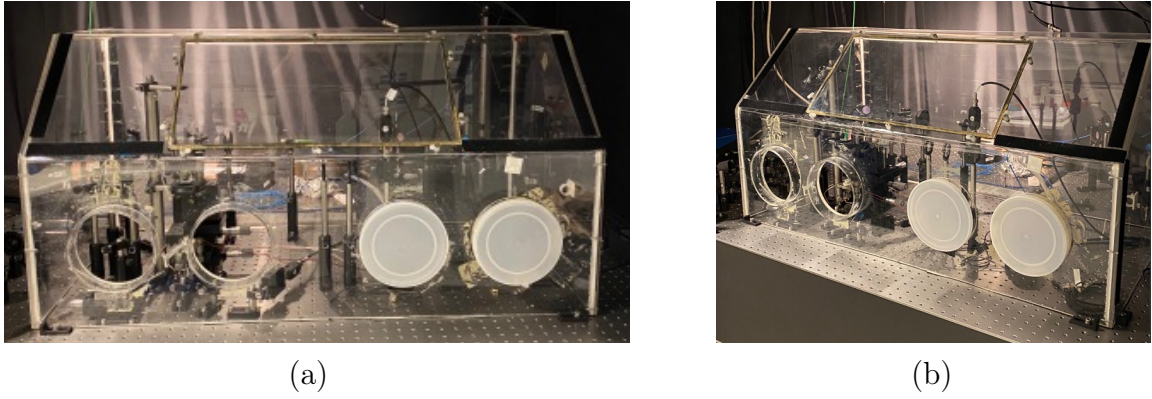


Figure 37: Front- (a) and side (b) views of the plexi-glass box used to reduce the acoustic noise in the setup.

By examining the characteristics of the noise when apparent, the source appeared to be acoustic in origin, i.e. making a sudden sound in close vicinity of the setup caused a spike in the noise level.

In order to reduce the acoustic noise, a plexi-glas box was placed around the entire setup as seen in figure 37. This proved to reduce the noise, and this improve the signal-to-noise, ratio substantially.

3.1.7 Additional equipment used

In order to record a measurement of any kind in the setup, a *Keysight Infini-iVision DSOX2024A* oscilloscope was connected with all the detectors P_T , P_R

and P_I in the setup. The oscilloscope, along with the Toptica laser, was then controlled by a Matlab script implemented by previous students/researchers of the lab.

Scanning the piezo element, by application of an alternating current also required additional equipment, and more specifically a frequency generator capable of generating a triangular signal with an offset. The frequency generator used was a *Keysight 33500B Waveform Generator*. Insight on scanning the cavity length using the piezo will be provided in section 3.3. The oscilloscope and frequency generator are shown in figure 38.



Figure 38: Pictures of the oscilloscope (a) and frequency generator (b) used during experimental investigations in this project.

3.2 Characterization of sub-wavelength grating

The sub-wavelength gratings, or Fano mirrors, used are commercially available high-quality silicone nitride *SiN* membranes suspended on a *Si* frame, which have been patterned into a grating. Figure 39a shows a packaged membrane from Norcada, which is the company who has provided all gratings/membranes used in this project. Figure 39b is a close-up picture of a bare membrane which have not yet been patterned, and includes a scale to provide perspective regarding the physical dimensions.

The patterned area of the Fano mirrors used throughout this project is $400 \times 400\mu m$, and this along with detailed dimensions of the whole membrane is sketched in figure 40.

3.2.1 The alignment procedure

In order to align the Fano mirror for its optical characterization only, the setup utilized is a simplified one, compared with the double Fano cavity setup shown

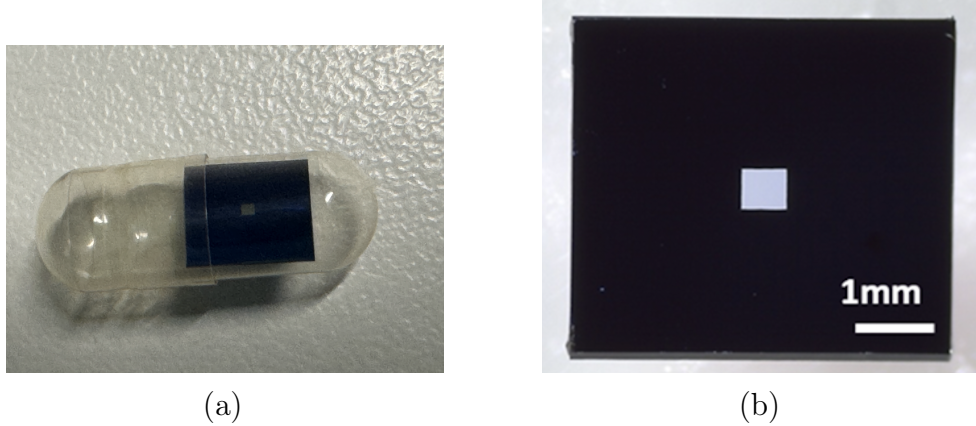


Figure 39: (a) shows an image of a packaged bare membrane, which has not yet been patterned, from Norcada. (b) is a close-up image of a bare membrane like the one in figure 39a.

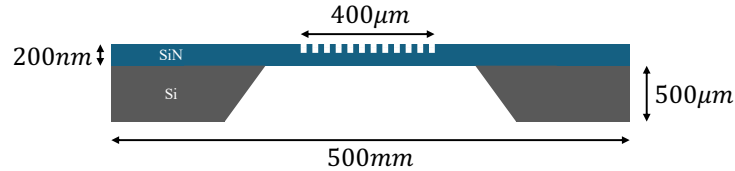


Figure 40: A simple sketch of the profile of a patterned membrane, i.e. a Fano mirror. It is seen that the width of the patterned area is $400\mu m$.

in figure 29a. This setup corresponds to one where only the *bottom* part is included, i.e. corresponding to the one highlighted in figure 34a. It must here be noted, that if the purpose of the Fano mirror alignment is to create a cavity, the top part shown in figure 35a must of course be utilized as well.

The goal of the alignment procedure is to ensure that the coupling between the guided-mode and the mode of the laser is maximized, this is outlined in section 2.2. The transmission of the Fano mirror is measured during alignment with a *PM100D* digital handheld optical power meter from Thorlabs, and progression of the alignment procedure is understood as minimizing the transmission. The behavior of the Fano mirror transmission, when perfectly aligned, can be seen in figure 8, where it has been simulated for a Fano mirror of arbitrary parameters. When aligned, the guided-mode resonance wavelength can thus be found. This is practically done by scanning the expected wavelength range using the Toptica laser and recording the wavelength at which the transmission is minimized.

The three degrees of freedom, in which the alignment of the Fano mirror is optimized, are the spacial coordinates (x, y), the rotational degree of freedom,

and the two angular degrees of freedom. It is assumed at this point that the waist of the beam incident on the Fano mirror is optimal, this will be expanded upon in section 3.2.2.

The general order in which the alignment is done is given as:

1. xy-plane alignment.
2. Alignment of the angular degrees of freedom (adjusting the kinematic mirror mount).
3. Rotational alignment (adjusting the HWP placed prior to the cavity setup).

xy-plane alignment

The spacial alignment of the Fano mirror in the xy-plane is simply done by movement of the xy-stages (linear μm -stages from Thorlabs) shown in figure 29a. Here it is crucial to know how the transmission level behaves qualitatively as a function of the xy-positions when the wavelength of the laser is off-resonance with respect to the guided-mode of the Fano mirror. Due to the effective thickness of the membrane in patterned and un-patterned areas being different, the transmission properties will vary slightly. This can be utilized in order to align these parameters effectively. Assuming one of the coordinates, x or y , is optimal, and one scans across the other as indicated in figure 41, it will be evident that the transmission is constant when the entire beam is incident on the bare membrane, while it will experience a slight decrease in the patterned area, simply due to the lower effective thickness of the structure in this area. For this reason the optimal alignment in this direction is found as the minimum transmission as a function hereof.

Angular alignment

Adjusting the angular alignment, which is done by adjusting the screws on the kinematic mirror mount holding the piezo ring and the Macor membrane holder, is crucial for the evaluation of the guided-mode resonance wavelength. As reported by Parthenopoulos et al. in [42] the resonance wavelength of the guided-mode depends strongly on the angle of incidence.

In figure 28 the components I_{1-4} indicate apertures (iris') used for the angular alignment. Specifically I_1 and I_2 are used to track the back-reflection of the

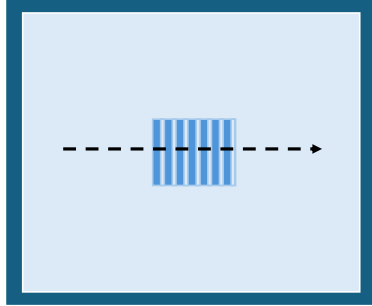


Figure 41: Simple sketch of a patterned membrane, i.e. a Fano mirror. The darker area surrounding the *SiN* membrane is the *Si* frame and the dark blue lines in the center indicate the $400 \times 400\mu m$ patterned area. The black dotted arrow is indicative of scanning across the membrane, by moving it relative to the beam, using one of the linear stages.

beam incident on the Fano mirror to ensure a high degree of overlap as possible. A complete overlap indicates that the incident beam is normal to the Fano mirror surface.

Rotational alignment

The Fano mirrors provided by Norcada are of so-called TM polarization, meaning that the magnetic field is parallel to the grating lines, and is thus perpendicular to the electric field. Since the polarization is defined along the axis of the electric field, this means that the polarization axis must also be perpendicular to the grating lines, as this ensures the interaction is maximized[49].

For this reason the rotational alignment is vital to achieving the correct minimum transmission wavelength of the Fano mirror.

Since no rotaitonal degree of freedom is appointed the Fano mirror itself, and that this would greatly complicate the alignment procedure, the rotational alignment is achieved by changing the polarization of the incident light. This done by adjusting hte rotating HWP placed immediately before the light hits the Fano mirror surface and is possible due to its effect on linearly polarized light illustrated in figure 32.

3.2.2 Adjusting and measuring the beam waist

In section 3.2.1 we assumed an optimal beam waist as the alignment procedure was outlined. This was due to the fact that the beam waist optimization is unnecessary unless the entire setup is rebuilt or if the size of the Fano mirror

is changed. Since the patterned area of the Fano mirrors characterized in this project was only $400 \times 400\mu m$, the beam waist optimization was only done once.

As is evident from figure 33a how an optical telescope was utilized to tune the waist size w_0 of the collimated laser beam. In order to determine the optimal value of w_0 the second lens L_2 was moved back and forth without diverging from the position where the optical axis passed through the center of the lens. The minimum transmission was recorded for each iteration, and the transmission would converge towards its minimum value (or at least the lowest achievable value). When the minimum transmission as a function of w_0 was found, this was measured using the *razor blade method*. The razor blade method is a simple tool to, fairly accurately, measure the beam waist of a Gaussian laser beam by *cutting* the beam gradually with a blade. The distance the blade moves is recorded along with the transmitted intensity, and the two are thus directly correlated[50].

An arbitrary Gaussian distribution, corresponding to a laser beam in the TEM00 mode, is shown on the left in figure 42, while the right plot shows the integral of the distribution as a function of the razor blade position, which corresponds to an error function.

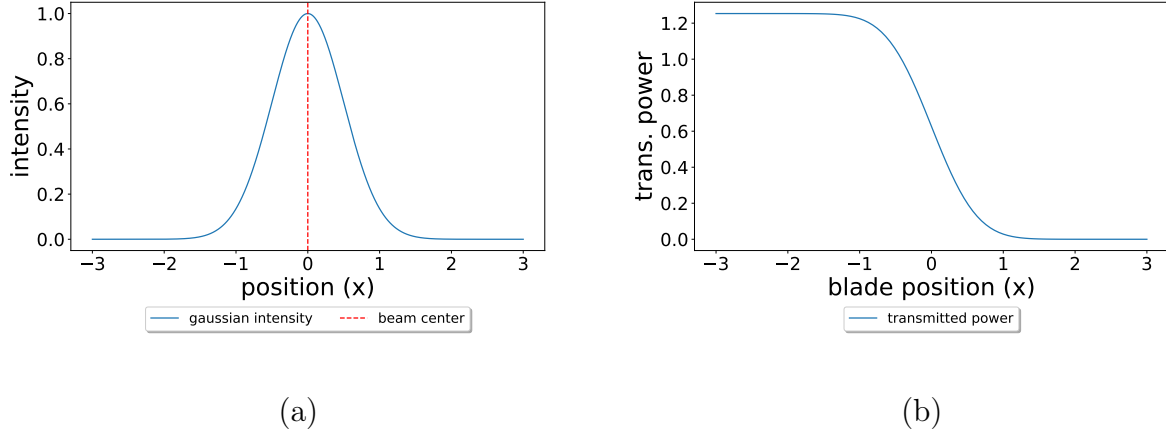


Figure 42: The left plot (a) shows an arbitrary Gaussian distribution, and the red dashed line indicate the placement of the maximum value. The right plot (b) shows the transmitted intensity as a function of the position of the razor blade, as the razor blade method is simulated, i.e. the beam is gradually covered with the blade.

In practice the blade position was recorded by counting the turns made on a

linear μm -stage with the razor blade attached, and the transmitted intensity was recorded live by a power meter from Thorlabs. The power of the laser beam without being *cut* by the blade was tuned to $\sim 1\text{mW}$ such that the percentile change was intuitively seen. The linewidth of the Gaussian beam is then approximately given as the distance between the two cut-off points where the transmitted intensity is given as 16% and 84%³. The optimal value for the linewidth was found to be

$$\delta\lambda_{400\mu\text{m}} \approx 160\mu\text{m}. \quad (51)$$

3.2.3 Obtaining normalized transmission/reflection spectra

When the Fano mirror and the surrounding setup is completely aligned, it is time for the optical characterization. In order to do so, a series of measurements is necessary to obtain normalized transmission and reflection spectra which rightfully represent the optical properties of the Fano mirror.

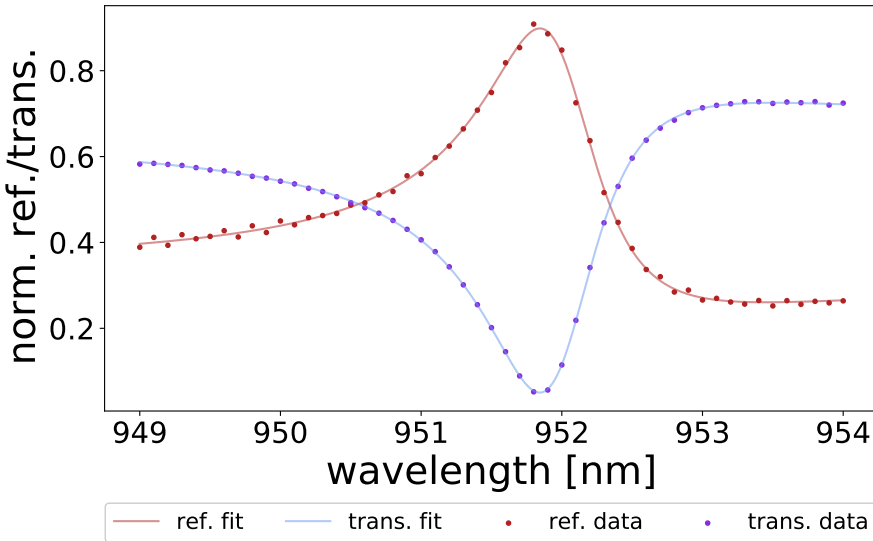


Figure 43: Normalized transmission and reflection spectra of $400 \times 400\mu\text{m}$ Fano mirror *G2* (*M3*).

The structure of such measurements is given as follows:

³In reality this interval corresponds to the width according to two standard deviations 2σ , which is only approximately equal to the linewidth.

1. The transmission and reflection intensities as a function of wavelength are measured using the reflection detector P_R and the transmission detector P_T , while the signal measured in detector P_I is recorded as a reference measurement. The positions of all detectors are shown in figure 28.
2. The Fano mirror is removed and identical measurements are done for an "empty" setup. The purpose of this measurement is to measure the signal when *all* the incident light is transmitted, and *no* light is reflected. This data is used to normalize the transmission intensities obtained in the first measurement.
3. On the former position of the Fano mirror, a highly reflective (HR) mirror is now placed, and all measurements are repeated. This is corresponding to *all* the incident light being reflected, and *no* light being transmitted. This data is used to normalize the reflection intensities obtained in the first measurement.
4. Lastly, a measurement of the background signal is taken, by simply blocking the laser before it enters the setup and repeating the measurements.

The normalized values are then given as

$$T_{norm} = \frac{(T - bg)/(T_I - bg)}{(T' - bg)/(T'_I - bg)} \quad (52)$$

for the transmission amplitudes, and

$$R_{norm} = \frac{(R - bg)/(R_I - bg)}{(R' - bg)/(R'_I - bg)} \quad (53)$$

for the reflection amplitudes. Here $T = |t|^2$ and $R = |r|^2$ denote the transmission and reflection amplitudes measured by P_T and P_R in step (1), T' and R' are the values measured for the transmission- and reflection amplitudes in steps (2) and (3), respectively, and the subscript I indicates values obtained by the incident detector P_I for its corresponding measurement type. The background values obtained in step (4) are subtracted, these are labeled bg . Figure 43 shows an example of normalized spectra obtained by measurements (1)-(4) and calculations of eqs. (52) and (53).

3.3 Cavity measurements

The cavity measurements here, primarily, outlined will be that of the double Fano cavity. The single Fano cavity measurement procedure will secondarily be

clear as a simplification of the one for the double Fano cavity.

Very simply put for the cavity measurement procedure, is that one must go through the Fano mirror alignment process outlined in section 3.2 twice. One time for the bottom of the cavity, and then once for the top of the cavity, whereafter the two Fano mirrors are broad together according to the wanted cavity length and the transmission is recorded. However, this procedure contains many degrees of freedom and practicalities making it difficult to simply align each Fano mirror independently of each other. This section will go through each step of the process of arriving at a meaningful measurement of the transmission of the double Fano cavity. The reflections of improving the used method will be included in the discussion section.

3.3.1 Aligning the double Fano cavity

Before considering beginning to align the double Fano cavity, it is imperative to have two Fano mirrors which have similar physical dimensions, and thus be described by similar parameters as presented in section 2.2. In order to find a *match*, the only valid method is to use brute force and simply characterize Fano mirrors until a match is found. The batch of tested Fano mirrors in this project all came from the same order delivered by Norcada, as this was assumed to provide the best chances for a match. The condition for the spectral detuning $\Delta = |\lambda_{0,1} - \lambda'_{0,1}|$ of otherwise identical and lossless Fano mirrors is outlined in section 2.4.5.

Assuming a match is found, which we denote G_1 and G_2 ⁴, the alignment process is given as follows:

1. The bottom, i.e. the arbitrary Fano mirror G_1 , of the cavity is aligned according to the procedure outlined in section 3.2. This means that the incident beam is centered on and normal⁵ to G_1 , and the polarization of the light is aligned such that the electric field is perpendicular to the grating lines. The wavelength of the laser is scanned, and the one corresponding to the guided-mode resonance of G_1 is recorded.
2. The bottom grating position is marked and the macor membrane holder

⁴ G here stands for *grating* while 1, 2 is indicative of the distinction between the two arbitrary Fano mirrors.

⁵A trick to determine the degree of accuracy of the angular alignment is to periodically block the light reflected from the Fano mirror, and thus make this flicker. This way the flickering light is easily distinguishable from the incoming light and by examining the light at apertures I_2 and I_1 from all sides perpendicular to the propagation direction, the needed angular adjustments become clear.

(the macor membrane holder can be seen in figure 29a) containing G_1 is removed and stored safely. Now the laser polarization and spacial coordinates of G_1 are fixed and must not be changed in the following steps of the alignment procedure. The marks used to indicate the position of G_1 is shown in figure 44.

3. The top part of the cavity is inserted, but *without* the other Fano mirror G_2 in place, as the kinetic mirror- and rotational mounts first need to be centered in the beam. This is done by inserting a $100\mu m$ pinhole, specifically designed for the purpose, into the rotational mount. The spacial and angular coordinates of the top mount is thus changed to maximize the signal through the pinhole. The centering is then tested by rotating the pinhole and ensuring that the signal does not change, i.e. that the center of the rotational mount does not move out of the beam by rotating it. When this is satisfied, the top mount is removed and the spacial coordinates are considered aligned and thus fixed. The so-called *pinhole alignment method* will be explained in greater detail in section 3.3.5.
4. The Fano mirror G_2 is placed, with tape, onto the xy-adjustable mount (see figure 29a), which is then fastened to the rotational mount. The top mount now completely resembles the one shown in figure 36. G_2 is now aligned following a similar structure as the one outlined in section 3.2, but with the constraint of the above parameters being fixed. G_2 is moved into a position where it is centered with respect to the incident beam by adjusting the xy-adjustable mount, and the Fano mirror itself is now rotated to match the polarization of the laser. The angular alignment is done very similarly to that of G_1 , as the kinetic mirror mount is here used. When G_2 is aligned, the wavelength is once again scanned, and the one matching the guided-mode of G_2 is recorded.
5. The top mount, including G_2 , is now removed from the setup and all degrees of freedom are expected to be aligned. The trick to make sure that the angular alignment is preserved when re-inserting the top mount is that the back reflection is centered in the aperture I_4 depicted in figure 28, this way one can quite easily regain the approximate angular alignment.
6. The macor mebrane holder, with G_1 placed on it, is now re-inserted into the bottom of the setup and the Toptica laser is set to the guided-mode resonance wavelength according to G_1 . In this way G_1 is carefully placed

according to the marked position (see figure 44) and adjusted, by hand, to achieve the same minimum transmission as before it was removed.

7. The top mount, including G_2 , is now too re-inserted, and adjusted by hand such that the back-reflected beam overlaps with the aperture I_4 .
8. The wavelength of the Toptica laser is now set to the transmission wavelength given in eq. (48), the wavelength exactly between the guided-mode resonance wavelengths of G_1 and G_2 , i.e. $\lambda_t = (\lambda_{0,G_1} + \lambda_{0,G_2})/2$.

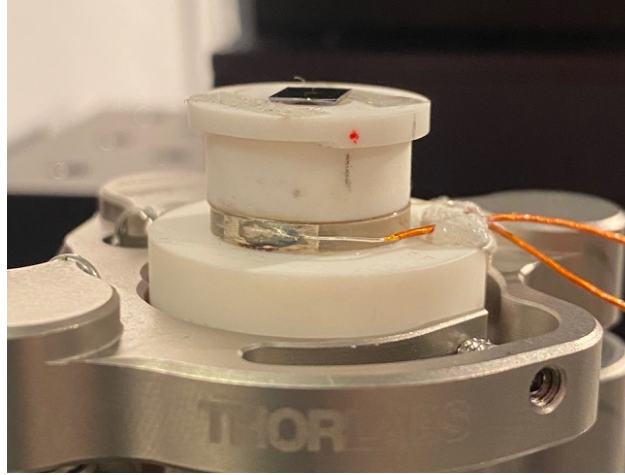


Figure 44: A close-up of the bottom part of the cavity with a Fano mirror placed on the macor membrane holder. Note the marks used to re-insert the bottom part of the cavity as mentioned in steps 2 and 6.

3.3.2 Cavity resonance - the piezo ring

Once the double Fano cavity is successfully aligned with respect to the individual guided-modes of G_1 and G_2 , the cavity mode (i.e. the cavity length) must be made to coincide in order to excite the Fano resonance mode. Here we remember that the cavity length is related to the cavity mode through the general Fabry-Perot cavity brightness condition $2l = m\lambda$.

In order to tune the cavity length on the scale necessary, it is scanned by periodically varying the length of the cavity using the piezo ring and applying an alternating current specified with the frequency generator shown in figure 38b. In this way the resulting signal recorded with photo detector P_T and seen in the oscilloscope shown in figure 38a is time-dependent and seen as fringes. Figure 45 shows the corresponding fringes for an approximate cavity length of $100\mu\text{m}$, both simulated and as data obtained directly from the oscilloscope screen.

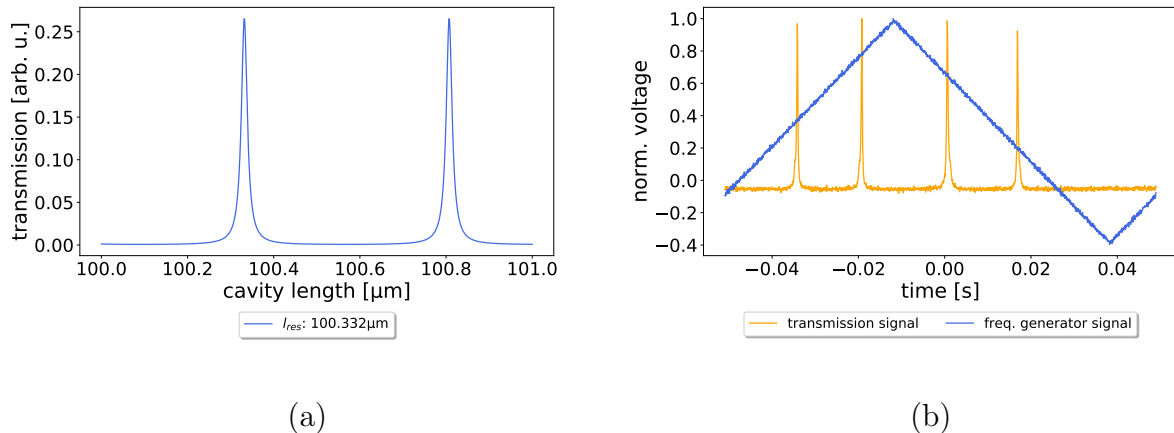


Figure 45: (a) shows a simulated length scan of range $1\mu m$ for a symmetric lossless double Fano cavity of length $\sim 100\mu m$. The labeled resonant length l_{res} in the figure indicates the first length found that fulfills the brightness condition. (b) is a plot of raw data logged from the oscilloscope used to record cavity transmission data. The blue line shows the signal from a frequency generator which is applied to the piezo ring, i.e. it correlates to the piezo expansion and thus a change in the cavity length. The orange line represents normalized cavity transmission intensity as a function of time, i.e. the cavity length. Note that the triangular signal is necessary in order to uniformly expand and compress the piezo ring. This ensures that the FSR stems from a linear expansion and that the piezo ring does not break from non-linear stress across the crystal structure.

When the fringes on the time-dependent length scan are visible while scanning with the piezo ring, they can be optimized by making small adjustments of the angular degrees of freedom of the top of the cavity, i.e. of G_2 . The parallelism of the cavity is an important parameter for a cavity of high finesse, and while normal incidence have here been achieved for G_1 and G_2 individually, both Fano mirrors have since been removed and re-inserted into the setup, which introduces uncertainty regarding the fine-tuning of the alignment. Especially the top of the cavity, which is fastened on nothing more than an optical post from Thorlabs and thus have only approximate reproducibility of the angular alignment (this is seen in figure 36), is prone to uncertainties hereof after re-insertion. For this reason the parallelism is optimized using the fringes on the oscilloscope. The parallelism is outlined in greater detail in section 3.3.6.

When the fringes of the time-dependent signal have been optimized fully, the frequency generator is then turned off and the fringes disappear. The piezo driver

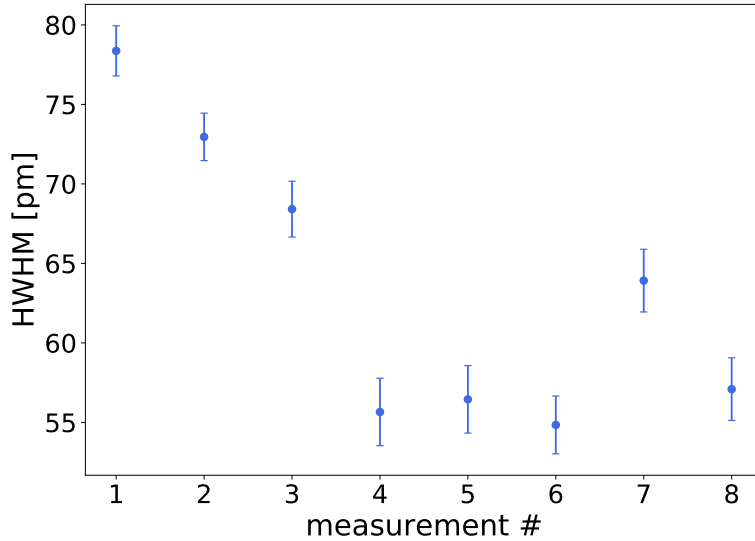


Figure 46: Linewidth as a function of "time" of an approximately $452\mu m$ double Fano cavity. It is clear that the linewidth generally decreases with time as a baseline for the HWHM is reached. This is assumed to be due to the drift of the piezo ring, while it must be noted that this is not possible to conclude indefinitely from the presented data. "Time" is to be understood as the chronological order in time, as the measurements are presented in the order in which they were recorded in the lab.

is now used to manually apply a constant voltage to expand the piezo gradually until the signal through the Fano cavity is maximized. This corresponds to the point where the cavity length and thus the cavity mode is resonant with the guided-modes of G_1 and G_2 .

The piezo ring, while capable of tuning the cavity length on a very small scale, tends to drift with time. This drift is apparent when the constant voltage is applied as the signal tends to decrease with time after optimization of the transmission. The piezo drift is more pronounced when the measurement session is first started and the time it takes for the piezo to lengthen or shorten becomes longer when a constant voltage have been applied to the piezo for some time. For this reason the measurements of the Fano resonance transmission profiles tend to be broader at first, and then gradually converge to the optimal value as more measurements are conducted. Note however, that this varies greatly depending on the adjustments made throughout a measurement session. Figure 46 shows linewidths of the resonance transmission profile, of an arbitrarily chosen double Fano cavity, as a function of "time". "Time" is referring to the fact that the

measurements are plotted in chronological order with respect to the time of measurement.

3.3.3 Determining the cavity length

Now the double Fano cavity is aligned and the cavity-, laser- and guided-modes all coincide to a high enough degree to sustain a Fano resonance mode. However, before doing the actual optical characterization, the cavity length must first be determined. In the end we want to plot the linewidth of the double Fano resonance spectra as a function of the cavity length, and in order to do so we must measure both.

Here we remember that the Fano cavity, when off-resonance, acts simply as a Fabry-Perot interferometer, which means that the off-resonance spectrum abides by the relations outlined in section 2.1. More specifically we know that the FSR relates to the cavity length according to eq. (??), which can be re-interpreted, and re-written, as

$$l = \frac{\lambda_0^2}{2FSR}, \quad (54)$$

where λ_0 is the cavity resonance wavelength.

So, to have a qualitative measure of the cavity length while doing measurements in the lab, off-resonance spectra are recorded and by estimating the FSR from the live data the approximate cavity length is determined.

In order to obtain precise information on the length of a given cavity, we conduct more precise data analysis on the recorded off-resonance spectra. Figure 47 shows two examples of off-resonance spectra for two cavities of different length. The lengths are found as a fitting parameters from a least squares fit of the recorded data to the Fabry-Perot transmission function found in eq. (4).

3.3.4 Recording normalized spectra

The normalized spectra are now recorded in largely the same way as for the individual Fano mirrors in section 3.2, a series of measurements is necessary in order to obtain meaningful spectra that are normalized with respect to the light incident on the cavity. The needed measurements are the following:

1. The transmission through the Fano cavity recorded in photo detector P_T where the corresponding values for the measured amplitudes are denoted

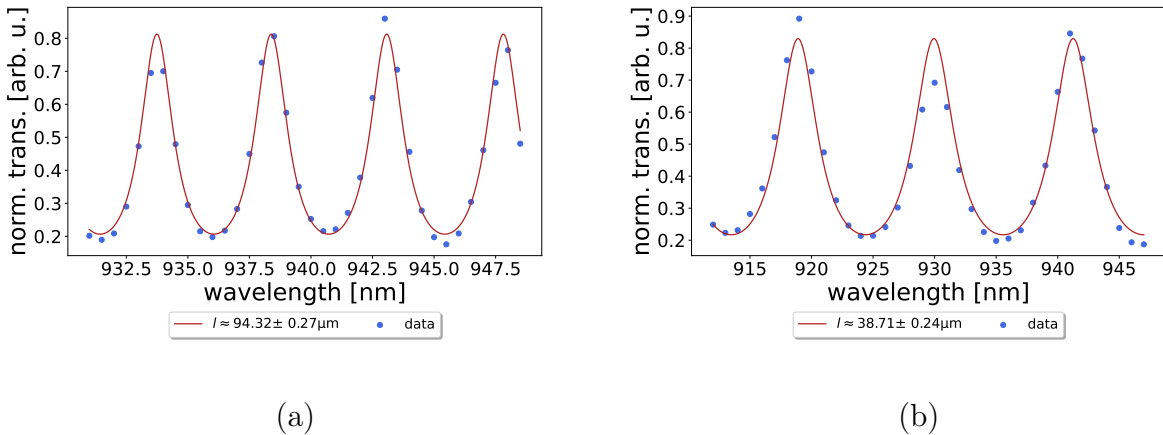


Figure 47: Off-resonance spectra of double Fano cavities of lengths $94.32 \pm 0.27\mu m$ (a) and $38.71 \pm 0.24\mu m$ (b). The lengths are found as fitting parameters from a least square fit of the recorded data to the Fabry-Perot transmission function in eq. (4), and the errors presented are found as the square root of the diagonal of the covarians matrix corresponding to the fit [51]. Note that the FSR increases when the cavity length decreases, as predicted in eq. (??).

T .

2. The light recorded in photo detector P_I during the transmission measurement. The corresponding values for the measured amplitudes are denoted T_I .
3. The light recorded in photo detector P_T when no cavity is present in the setup. This is denoted P'_T . The corresponding values for the measured amplitudes are denoted T' .
4. The light recorded in detector P_I during the transmission measurement with no cavity present. This is similarly denoted P'_I . The corresponding values for the measured amplitudes are denoted T'_I .

The normalized transmission values are then given as

$$T_{norm} = \frac{T/T_I}{T'/T'_I}, \quad (55)$$

which is the exact formula used for the Fano mirror characterization, except for the subtraction of the background which has here been assumed negligible. Examples of the four measurements are seen in figure 48, and the normalized spectrum is correspondingly seen in figure 49.

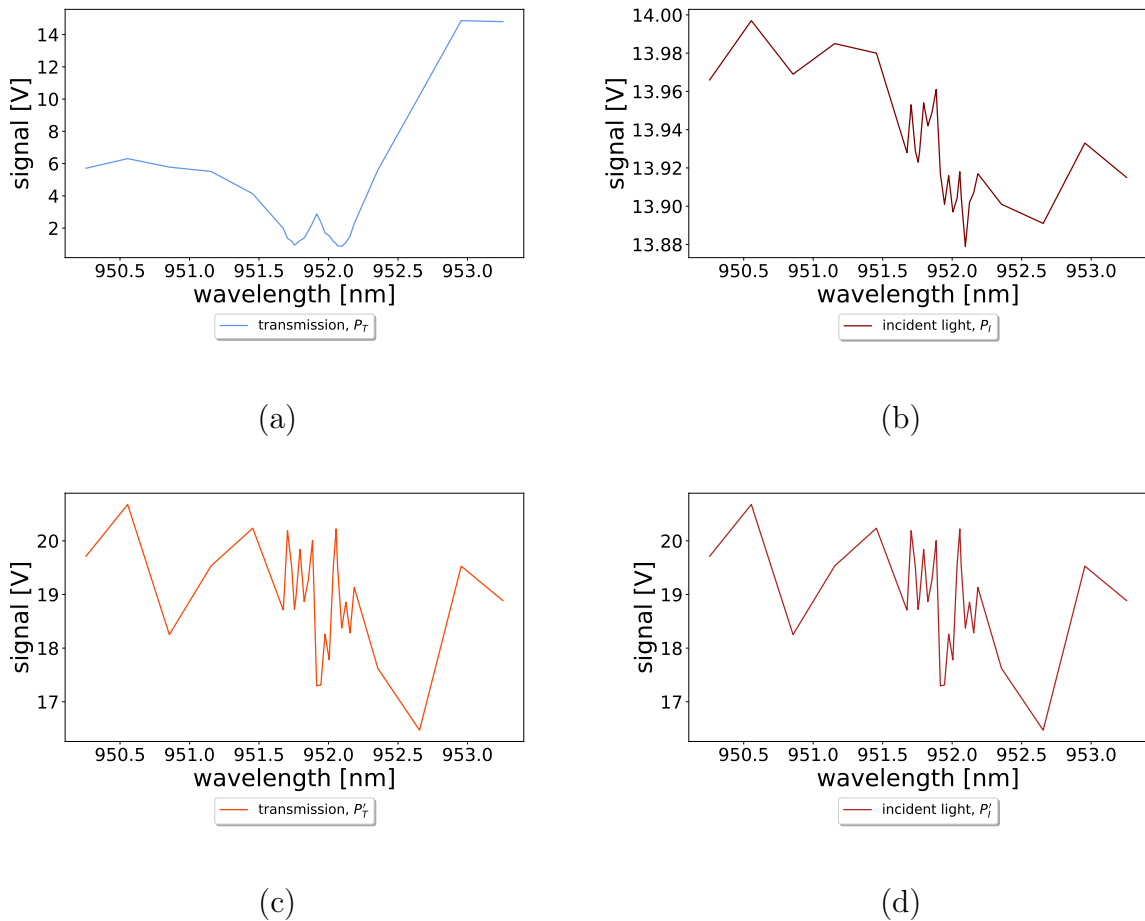


Figure 48: Examples of the four measurements used to produce the normalized transmission spectrum of the double Fano cavity (the same naturally applies for the single Fano cavity transmission). (a) shows the transmission through the double Fano cavity, (b) shows the incident light on the cavity, (c) shows the "transmission" when no cavity is present and (d) shows the light recorded by the incidence detector with no cavity present. All data is recorded for the same cavity of length $l = 21.390 \pm 0.119\mu m$. Note that the spectra in (c) and (d) seem identical. This is to be expected as they are simply measurements of a beam in each arm of a 50/50 beam splitter.

3.3.5 Centering of the top grating

When aligning the top part of the cavity setup seen in figure 35, it is crucial to ensure that the beam passes through the center of the rotational mount. Even the slightest deviation from the center can cause the alignment to be tedious at best, but likely practically impossible. The reason for this is the need for invariance in the xy-plane when aligning the Fano mirror for the fixed

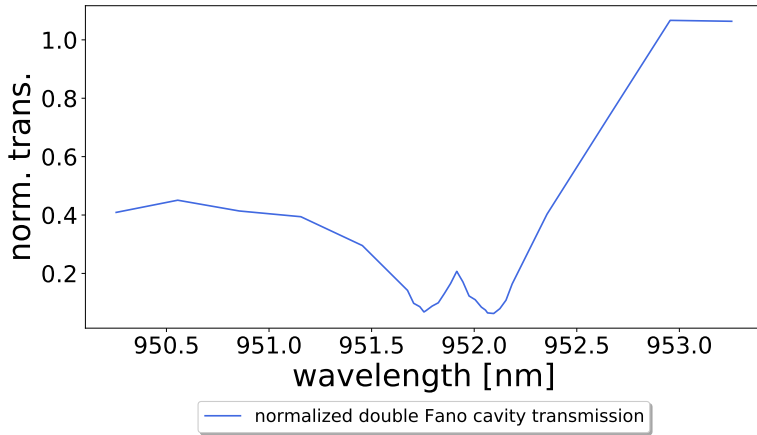


Figure 49: The normalized transmission spectrum for a double Fano cavity of length $l = 21.390 \pm 0.119\mu m$ calculated from the data depicted in figures 48a-d using eq. (55).

polarization of the laser. If the deviation from the center is too large, it might be impossible to tell whether the change in the transmitted intensity stems from moving further or closer to the optimal polarization, or if the Fano mirror is simply moving in and out of the beam. For this alignment a pinhole was designed to fit with high precision into the rotational mount in which it was fastened with a one inch (*SM1*) retainer ring from Thorlabs. A simple sketch of the pinhole is seen in figure 50a.

By moving the xy-stages in the cavity setup, it proved possible to achieve the centering of the rotational mount by moving the setup, with the pinhole inserted, until the transmission signal was maximized. Another test of the alignment was here to rotate the mount and thus pinhole and ensure that the signal intensity was as close to rotationally invariant as possible. Figure 51 shows an arbitrary gaussian distribution resembling the transverse distribution of a laser beam in the TEM00 mode and two shaded regions imitating the position of the pinhole. The red shaded region shows an *unaligned* pinhole position while the green one is perfectly *aligned* in the center of the beam. It is shown on the figure that the red area covers an intensity corresponding to 15.8% of the maximum intensity, while this value for the aligned green region is approximately double at 30.53%.

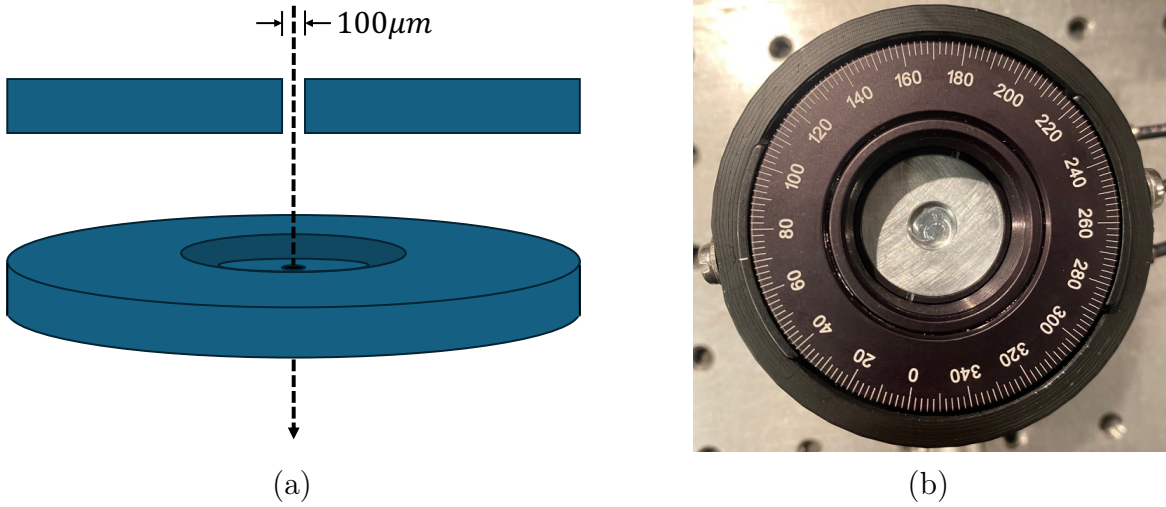


Figure 50: In (a) is a sketch of the pinhole used for centering the rotational- and kinetic mirror mounts in the incident beam. The side view of the pinhole is included to mark the pinhole diameter clearly while the angled view provides a visual representation of the actual component. (b) shows a picture of the rotational mount, seen from the top, with the pinhole inserted.

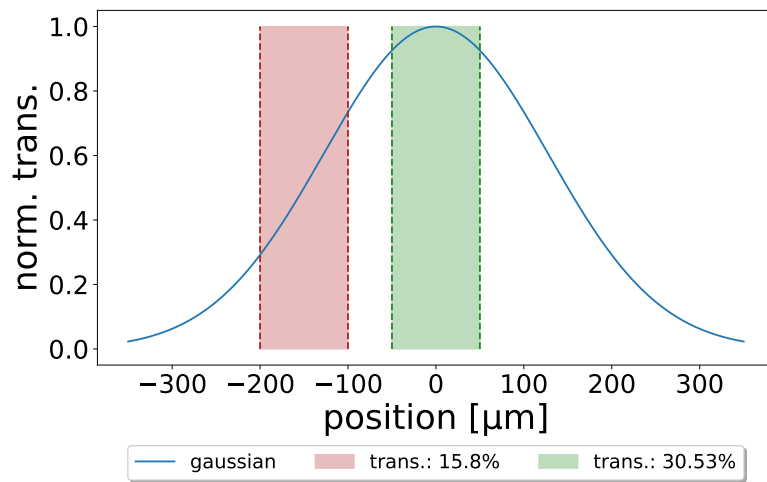


Figure 51: A gaussian distribution corresponding to the transverse distribution of a laser in the TEM00 mode. The red shaded region indicates a position for the pinhole with a transmission of 15.8% while the green one indicates a position with a transmission of 30.53%. The spacial dependence of the transmission through the pinhole is thus clearly displayed.

3.3.6 Estimating parallelism

A key difference between the single and double Fano cavity transmission spectra, is the off-resonance behavior. While the maximum transmission intensity for the single Fano will generally be lower than the Fano resonance peak, the opposite tends to be the case for the double Fano cavity. The direct reflectivities and transmissions r_d and t_d are similar, if not identical, for the two Fano mirrors, which means that the off-resonance Fabry-Perot-like transmission reaches a maximum of close to unity. The initial alignment of the cavity can thus be done by maximizing the off-resonance fringes. Due to the much broader peaks in this spectral regime, the fringes will be much less sensitive than the resonance peak. For this reason additional optimization is likely necessary.

Nair et al. [52] has proposed an analytical formula to estimate the wedge angle by considering the maximum transmission T_{MAX} of these Fabry-Perot fringes. T_{MAX} is given as

$$T_{MAX} \approx 1 - \left(\frac{F\pi w_0}{\lambda} \right)^2 \varepsilon^2, \quad (56)$$

for a cavity of identical resonators, and as this is not necessarily the case for an arbitrary double Fano cavity we make the substitution $1 \rightarrow T_{MAX}^{optimal}$ to include the highest possible transmission given a set of compatible Fano mirrors. The expression now simply reads

$$T_{MAX} \approx T_{MAX}^{optimal} - \left(\frac{F\pi w_0}{\lambda} \right)^2 \varepsilon^2, \quad (57)$$

where $T_{MAX}^{optimal}$ is the maximum transmission for a wedge angle of 0, w_0 is the beam waist, λ is the wavelength, ε is the wedge angle in radians and F is the coefficient of finesse [38] given as

$$F = \frac{4R}{(1-R)^2}. \quad (58)$$

Rearranging this, for the wedge angle ε we get

$$\varepsilon \approx \sqrt{\left(T_{MAX}^{optimal} - T_{MAX} \right)} \left(\frac{\lambda}{F\pi w_0} \right). \quad (59)$$

An example of a normalized off-resonance transmission spectrum of a double Fano cavity is shown in figure 52. The blue line indicates a least squares fit of

the data points to the Fabry-Perot transmission function seen in eq. (4), while the red line indicates the optimal transmission for the same Fano mirrors as was used for the measurement. The maximum transmission recorded and the optimal value was found as

$$T_{MAX} = 83.3\% \quad \text{and} \quad T_{MAX}^{optimal} = 97.1\%, \quad (60)$$

which yields for the wedge angle

$$\varepsilon \approx 0.24 \text{ mrad} = 0.014^\circ, \quad (61)$$

assuming a beam waist of $w_0 = 160 \mu\text{m}$ and direct reflectivities and transmissions $r_d = 57\%$, $r'_d = 57.5\%$ and $t_d = t'_d = 81.4\%$.

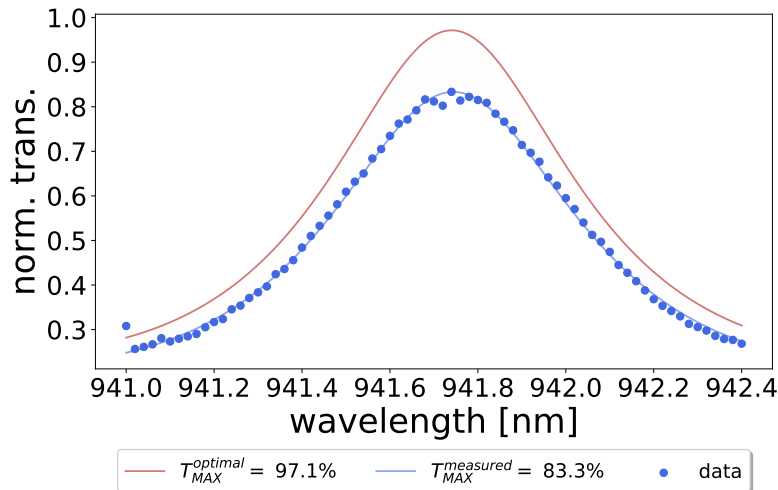


Figure 52: Example of a normalized off-resonance transmission peak of a double Fano cavity of direct reflectivities $r_d = 57\%$ and $r'_d = 57.5\%$ and direct transmissions $t_d = t'_d = 81.4\%$. The blue line is a least squares fit of the data to the Fabry-Perot transmission function while the red line is the optimal value of the same function. The red shaded area indicate the differnce between the two.

It is thus clear that while the sensitivity is of the off-resonance Fabry-Perot fringes is lower than that of the Fano resonance peak, they still provide a significant measure of the parallelism and is thus useful for initial cavity alignment.

4 Results

The aim of this project has been to realize the double Fano cavity experimentally and investigate its transmission profile as a function of the incident wavelength. In this section I present the best results obtained and comment on these. Furthermore, I will outline challenges and obstacles that have been encountered, their implications on the data presented and my thoughts on immediate improvements for future experiments.

The results obtained have been so through an iterative process realizing the theory presented in previous sections. For this reason, the structure of this section will outline this process and thus begin by an in depth spectral analysis of the Fano mirrors used, as a pair matching in optical parameters, and especially the guided-mode resonance wavelength, is crucial in order to realize the Fano resonance. When moving on to the results regarding cavity characterization I will begin by briefly verifying the results for the single Fano cavity presented by Mitra et al. in [35]. Finally, I will show experimental results of the optical characterization of the double Fano cavity.

4.1 Fano mirror characterization

The first important step in realizing the double Fano cavity, is to locate a matching pair of Fano mirrors, as a substantial spectral overlap is necessary in order to excite a Fano resonance including both guided-modes, as explained in section 2.4.5. For this reason the Fano mirrors considered were all fabricated externally by *Norcada* and furthermore from the same batch, as these were initially considered to have a greater probability of having similar physical attributes. Many Fano mirrors were thus characterized during the process of finding a match, and the pair eventually chosen to move forward with were denoted *G1* and *G2*.

Figure 53 show the individual measured normalized reflection and transmission spectra of G1 and G2 together with a least squares fit to the model derived in section 2.2. The corresponding optical parameters for each Fano mirror were found as the following.

Fitting parameters for G1:

$$\begin{aligned} \lambda_{0,G1} &= 951.764\text{nm}, \quad \lambda_{1,G1} = 951.901\text{nm}, \quad t_d = 0.814, \\ r_d &= 0.575, \quad \gamma_\lambda = 0.462\text{nm}, \quad \beta = 9 \cdot 10^{-7}\text{m}^{-1}. \end{aligned} \tag{62}$$

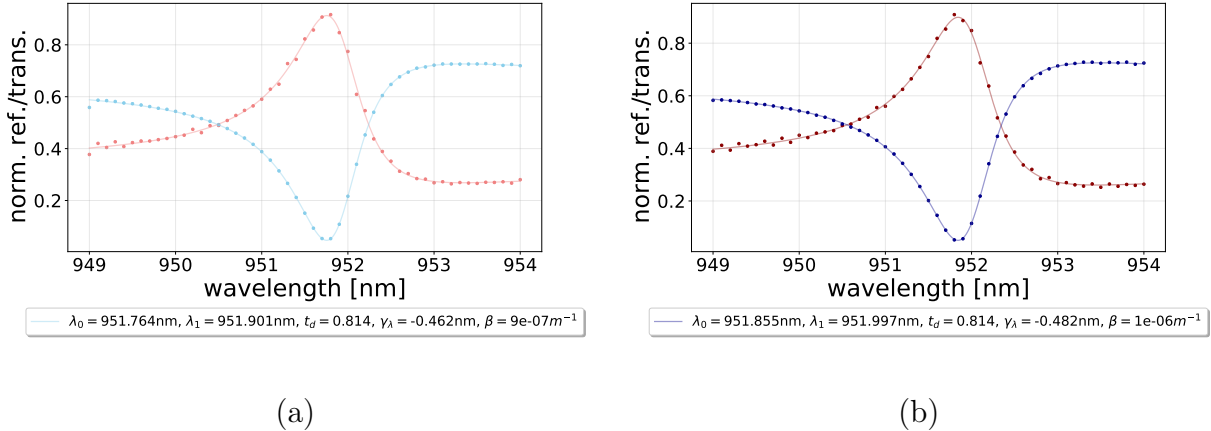


Figure 53: (a) shows the normalized reflection and transmission spectra of Fano mirror G1 along with its optical parameters found as fitting parameters from a least squares fit to the model derived in section 2.2. (b) shows the same for Fano mirror G2.

Fitting parameters for G2:

$$\begin{aligned} \lambda_{0,G2} &= 951.855 \text{ nm}, \quad \lambda_{1,G2} = 951.997 \text{ nm}, \quad t_d = 0.814, \\ r_d &= 0.570, \quad \gamma_\lambda = 0.482 \text{ nm}, \quad \beta = 1 \cdot 10^{-6} \text{ m}^{-1}. \end{aligned} \quad (63)$$

In order to evaluate and compare the parameters to determine whether the two Fano mirrors are in fact a good match, they are both shown alongside each other in figure 54 for spectral comparison. Each their resonance wavelengths λ_0 are indicated on the figure and the detuning can thus be estimated as

$$\Delta = |\lambda_{0,G2} - \lambda_{0,G1}| = 951.855 \text{ nm} - 951.764 \text{ nm} = 0.091 \text{ nm}. \quad (64)$$

Here we remember that the additional fitting parameters, namely t_d , r_d , γ_λ and β , are assumed identical in the model for the double Fano cavity outlined in section 2.4.2 and these are thus compared in a more qualitative manner. Whether the parameters in eqs. (62) and (63) can be assumed identical is completely individual to the given experiment and the corresponding acceptable margins. In order to move forward, G1 and G2 are assumed to only differ in guided-mode resonance wavelength.

As is shown in section 2.4.6, a spectral detuning leads to a spacial detuning, meaning that the cavity length corresponding to the guided-mode resonance wavelength for G1 and G2 are not identical as they have a non-zero detuning

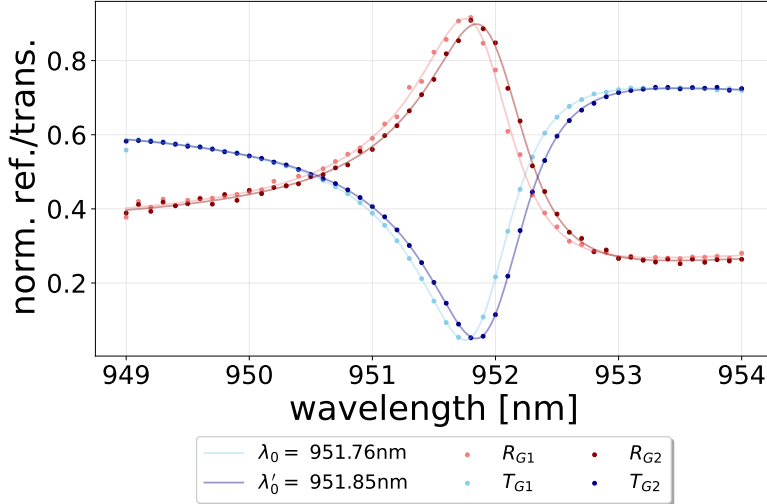


Figure 54: Spectral comparison of Fano mirrors G1 and G2. The spectra are the same shown in figure 53.

Δ . In order to sustain a Fano resonance it is equally important that the Fano mirrors have overlapping cavity transmission profiles as a function of the cavity length. Figure 55 shows the simulated double Fano transmission of a cavity consisting of G1 and G2 for length corresponding to their guided-mode resonance wavelengths. It is readily seen that the two transmission profiles overlap for the included example of a cavity of length $l \approx 30\mu m$.

4.2 The single Fano cavity

We recall that the single fano cavity consists of a Fano mirror and a broadband mirror in a plane-plane configurations where each mirror is perpendicular to the optical axis. The single Fano cavity configuration is briefly outlined in section 3.3 and otherwise shown in [35], it however resembles the double Fano cavity setup shown in figure 29, except only the bottom two xy-stages are used, and the top ones are therefore removed.

The mirror used is a high reflective (HR) broadband mirror with a reflectivity of 99.7%, meaning that effectively all intrinsic cavity losses can be assumed to be associated with the Fano mirror. The Fano mirror used is G1 characterized in section 4.1.

Figure 56 shows examples of off-resonance scans of the single Fano cavity, with corresponding fits to the Fabry-Perot transmission function, in order to

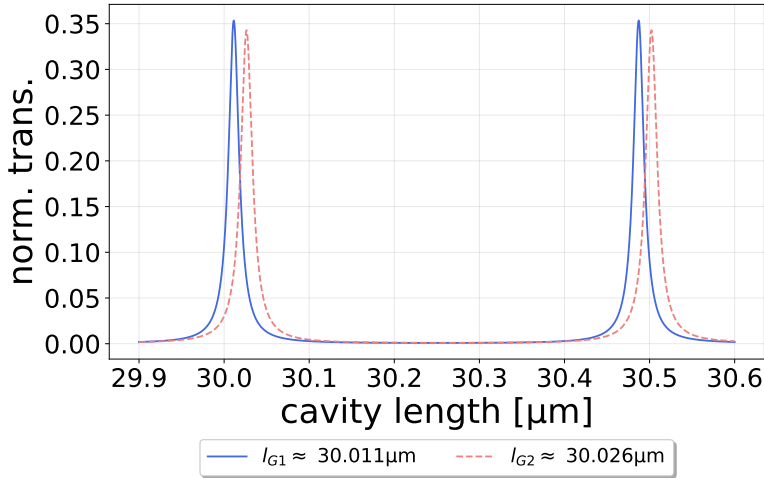


Figure 55: Simulated length scans of double Fano cavities with incident wavelengths of $\lambda_{0,G1}$ and $\lambda_{0,G2}$. The corresponding lengths determined from the scans are denoted l_{G1} and l_{G2} , respectively.

determine the cavity length from the measured FSR. Figure 56a shows the off-resonance spectrum for a cavity of length $l = 57.40 \pm 1.55\mu m$, while figure 56b shows the same for a cavity length of $l = 211.98 \pm 3.16\mu m$. The errors are determined as the errors of the fit, found as the squareroot of the diagonal of the corresponding covariance matrices.

Figure 57 shows examples of resonance transmission spectra of the single Fano cavity. The examples are taken for length corresponding to the ones found from the off-resonance spectra shown in figure 56 above. The figures are depicted with each their corresponding least squares fits to the generalized Fano model shown in eq. (33) in order to determine the linewidth (HWHM) of the profile. The errors of the linewidths are found from the error of the fit and are mainly used to determine the quality of the measurement.

At each cavity length, the resonance transmission profile was recorded a number of times and the average value was taken to be the found true value of the linewidth. Figure ?? shows the result of a measurement series consisting of five cavity lengths approximately ranging from $20\mu m \leq l \leq 400\mu m$, where the error of each measurement is given as the standard deviation of the values of all measurements recorded at each cavity length[51]. The error depicted in the x-direction is found from the error of the fit of the Fabry-Perot transmission

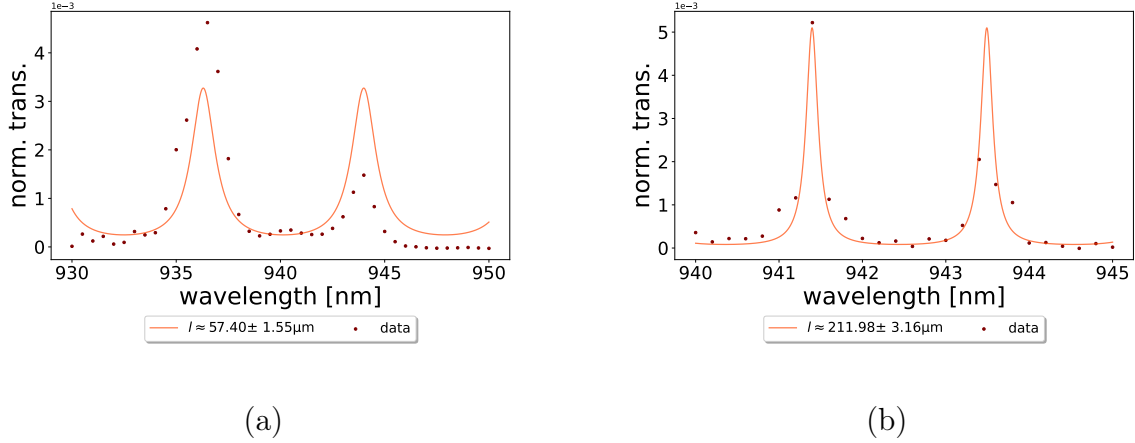


Figure 56: (a) shows an off-resonance wavelength scan of single Fano cavity consisting of a HR broadband mirror and G1 for a cavity length of $l = 57.40 \pm 1.55\mu m$. (b) shows this for a single Fano cavity of length $l = 211.98 \pm 3.16\mu m$. Each length is determined from these measurements by measuring the FSR and utilizing that $l = \lambda_0^2 / (2 \cdot FSR)$.

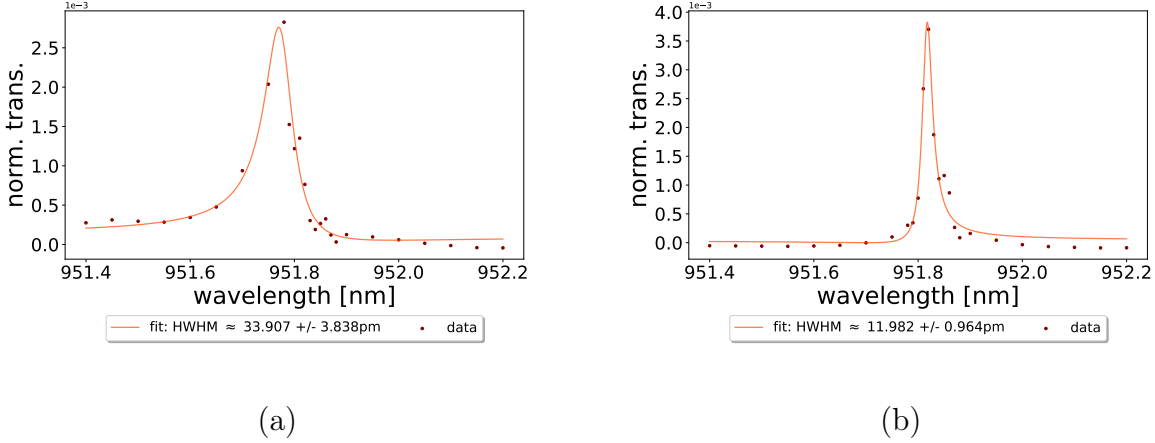


Figure 57: Single Fano resonance transmission profiles of a cavity consisting of a HR broadband mirror of reflectvitiy intensity $R = 99.7\%$ and Fano mirror G1. (a) shows the profile of a cavity of length $l = 57.40 \pm 1.55\mu m$ and displays a linewidth of $HWHM = 33.907 \pm 3.838\text{pm}$. (b) shows the profile of a cavity of length $l = 211.98 \pm 3.16\mu m$, with a linewidth of $HWHM = 11.982 \pm 0.964\text{pm}$.

function to the off-resonance spectra. The blue dashed line indicate the linewidth of a broadband cavity of similar losses according to eq. (35) and the orange dashed line thus indicate the analytical linewidth of the single Fano cavity considered consisting of G1 and the HR broadband mirror estimated using eq.

(36). The black points are linewidths found by fitting single Fano transmission profiles simulated using eq. (32) to the generalized Fano model in eq. (33) for comparison.

It is seen that the analytical model, the theoretically found linewidths and the measured linewidths coincide very well for the cavity lengths that are well-within the Fano regime and deviates slightly for longer lengths. This trend agrees nicely with what has previously been found for the single Fano cavity transmission[35] and is likely a consequence of the very narrow linewidths of the cavity in the standard regime, as this increases the sensitivity to any noise regarding the cavity length, e.g. mechanical vibrations in the setup.

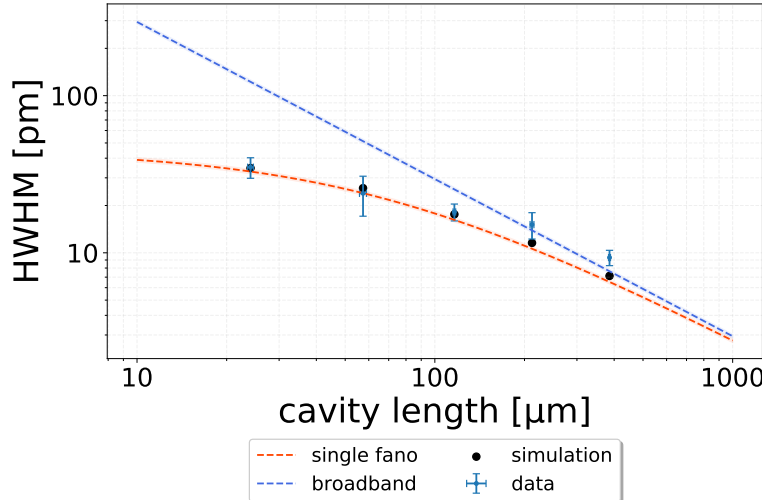


Figure 58: The linewidth (HWHM) as a function of resonant cavity length. The blue dashed line indicates the analytical linewidth for broadband cavity, and the orange dashed line shows the corresponding analytical linewidth for a single Fano cavity of similar losses to the one realized experimentally. The blue points and corresponding errorbars shows the measured linewidths found as averages of all recorded values at each length and the error is found as the standard deviation of these. The black points are the linewidths of simulated spectra.

4.3 The double Fano cavity

In this section I will give an account of the results for the characterization of a double Fano cavity consisting of Fano mirrors G1 and G2. First we look at the simulated spectra of the double Fano transmission intensity profile as a function of the incident wavelength simulated with the parameters for G1 given in eq. (62) and for G2 given in eq. (63). Figures 59 and 60 shows the simulated spectra for cavity lengths according to $l = l_{G1}$, $l = l_{G2}$ and $l = (l_{G1} + l_{G2})/2$ together with the reflectivity spectra for G1 and G2 also shown in figure 54.

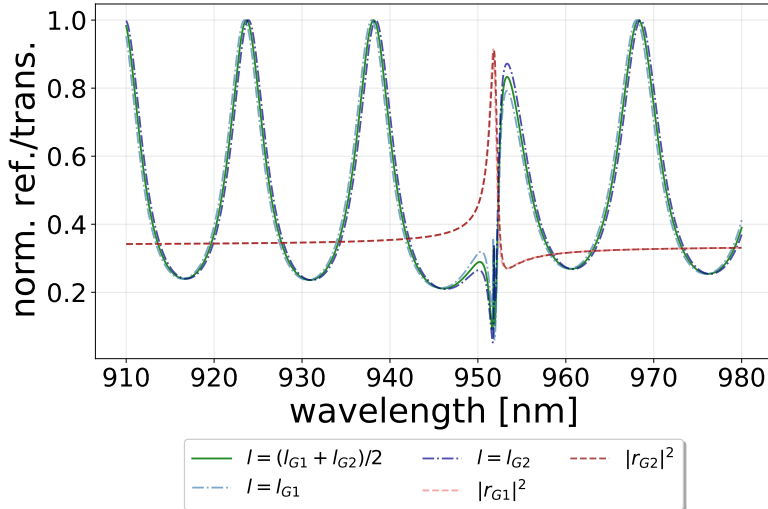


Figure 59: The simulated spectra of a double Fano cavity consisting of G1 and G2 for lengths $l = l_{G1}$, $l = l_{G2}$ and $l = (l_{G1} + l_{G2})/2$. The two red dashed lines are the fractional reflectivities of G1 and G2, respectively, shown in figure 54. The range plotted is chosen as it resembles the tunable range of the Toptica laser used for the experiments of this project.

It is seen in figure 59 that the off-resonance level is expected to almost reach unity for a perfectly aligned cavity, for the given direct transmission amplitude coefficients t_d , t'_d and the same for the direct reflectivities r_d , r'_d . This result for the simulated spectra is indicative of the validity of the assumption that these are at identical meaning that $t_{d,G1} \approx t_{d,G2}$ and $r_{d,G1} \approx r_{d,G2}$. Furthermore, the background perfectly resembles a low finesse Fabry-Perot cavity, as is expected from the theory.

Figure 60 shows the transmission spectra of the double Fano cavity zoomed on the resonance wavelengths considered according to the depicted cavity lengths.

Here it is seen how the transmission peak at resonance is expected to shift with the cavity length, and that the estimated detuning Δ of the two Fano mirrors seems to be sufficiently small in order to realize the double Fano resonance profile. Lastly, it is seen what to expect in terms of the peak height of the resonance profile as this is an important merit when practically estimating the losses, and by extension the alignment, of the cavity in the lab.

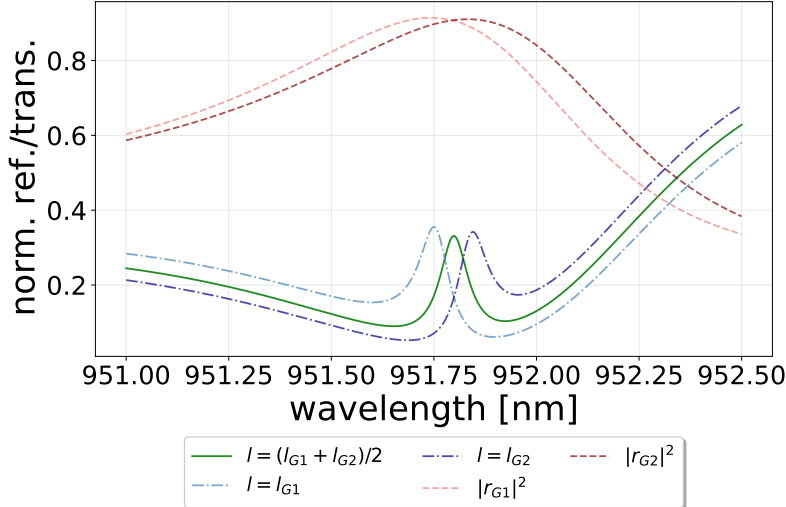


Figure 60: The simulated spectra of a double Fano cavity consisting of G1 and G2 for lengths $l = l_{G1}$, $l = l_{G2}$ and $l = (l_{G1} + l_{G2})/2$ focused around the corresponding resonance wavelengths. The two red dashed lines are the fractional reflectivities of G1 and G2, respectively, shown in figure 54.

I simulate the transmission profile for different cavity length in order to determine the optimal one. Figure 61 shows a colormap of the resonance profile as a function of wavelength and cavity lengths ranging $l_{G1} \leq l \leq l_{G2}$. The peak height is indicated by the brightness of the colormap, such that the resonance wavelength and cavity length is indicated by the "line" showing the resonance peak moving in terms of both parameters.

The colormap provides a qualitative and intuitive image of the behaviour of the double Fano transmission profile, but the optimal cavity length in order to optimize with respect to the linewidth is nearly impossible to determine. Figure 62 instead shows the linewidth of intracavity spectra as a function of the cavity length and shows that the optimal cavity length is approximately given as $l \approx (l_{G1} + l_{G2})/2$. In reality, the assymetric structure of the Fano

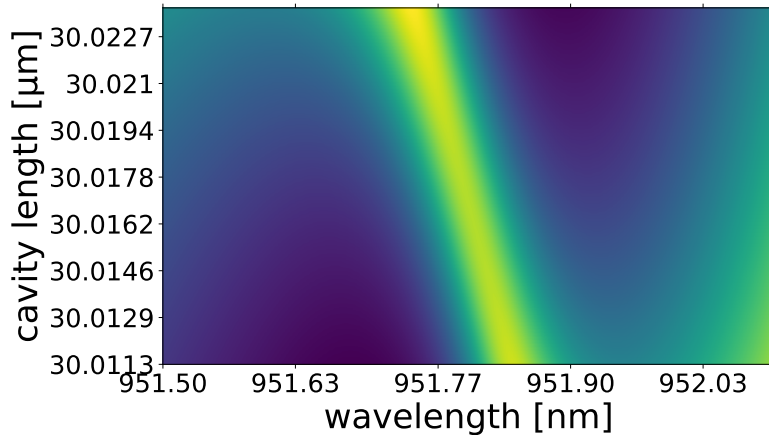


Figure 61: Colormap of the resonance transmission profile of the double Fano cavity consisting of G1 and G2. The brightness of the colormap indicate the intensity/peak height while the varied parameters are the wavelength and cavity length ranging $l_{G1} \leq l \leq l_{G2}$.

mirror spectra results in an exact answer to the optimal cavity that is more complicated, and likely impossible to realize in the lab. For this reason the approximate interpretation of the cavity length analysis is sufficient for practical purposes.

4.3.1 Realizing the double fano model

In order to realize the double Fano model in a satisfying way the whole spectrum is examined as the off-resonance profile resembling a low-finesse Fabry-Perot transmission spectrum, with near-unity transmission levels at each "Fabry-Perot" peak, is considered a defining feature of the double Fano cavity. In this section I will present three spectra obtained experimentally and compared with their corresponding simulated spectra for lengths $l = l_{G1}$, $l = l_{G2}$ and $l = (l_{G1} + l_{G2})/2$. Furthermore, I present the same spectra fitted to the double Fano cavity transmission model with fitting parameters given as the two sets of Fano mirror parameters, the cavity length and the resonant loss term L . The Fano mirror parameters found by the fitting function will thus be those that produce the reflection and transmission amplitude coefficients that best fit the data.

Figure 63a show the comparison of data and simulation for a cavity of lengths given as $l_{G1} = 239.3975\mu m$, $l_{G2} = 239.4317\mu m$, $(l_{G1} + l_{G2})/2 = 239.4146\mu m$.

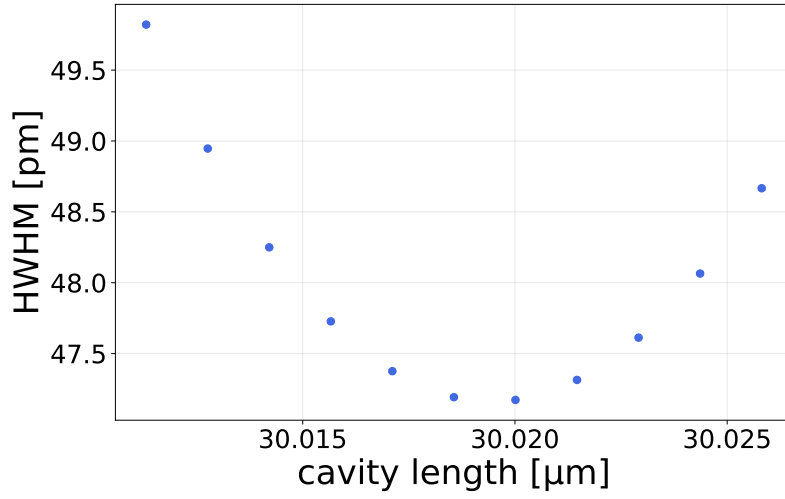


Figure 62: The simulated intracavity linewidth as a function of cavity length ranging $l_{G1} \leq l \leq l_{G2}$. Each linewidth is found by fitting simulated spectra to the generalized Fano model in eq. (33).

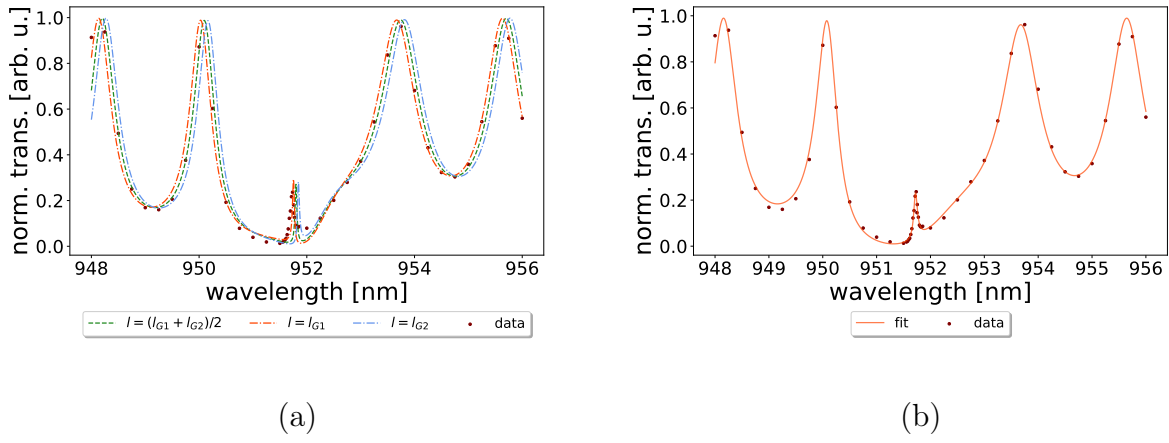


Figure 63: (a) shows recorded data of the double Fano cavity transmission compared with simulated spectra for cavity lengths of $l_{G1} = 239.3975\mu m$, $l_{G2} = 239.4317\mu m$, $(l_{G1} + l_{G2})/2 = 239.4146\mu m$. (b) shows a least squares fit of the recorded data to the double Fano cavity transmission model in eq. (37).

Figure 63b shows a least squares fit of the data to the double Fano transmission function with fitting parameters related to each Fano mirror, and the cavity as follows.

Fitting parameters related to Fano mirror G1:

$$\begin{aligned}\lambda_0 &= 951.330 \pm 0.072\text{nm}, \quad \lambda_1 = 951.328 \pm 0.110\text{nm}, \quad t_d = 0.827 \pm 0.016, \\ \gamma_\lambda &= 0.641 \pm 0.131\text{nm}, \quad \beta = 1.819 \cdot 10^{-6} \pm 9.314 \cdot 10^{-7}\text{m}^{-1}.\end{aligned}\tag{65}$$

Fitting parameters related to Fano mirror G2:

$$\begin{aligned}\lambda_0 &= 951.728 \pm 0.027\text{nm}, \quad \lambda_1 = 951.943 \pm 0.0428\text{nm}, \quad t_d = 0.823 \pm 0.015, \\ \gamma_\lambda &= 0.535 \pm 0.056\text{nm}, \quad \beta = 7.788 \cdot 10^{-7} \pm 1.480 \cdot 10^{-7}\text{m}^{-1}.\end{aligned}\tag{66}$$

Fitting parameters related to the cavity configuration:

$$l = 238.924 \pm 0.002\mu\text{m}, \quad L = 0.039 \pm 0.099.\tag{67}$$

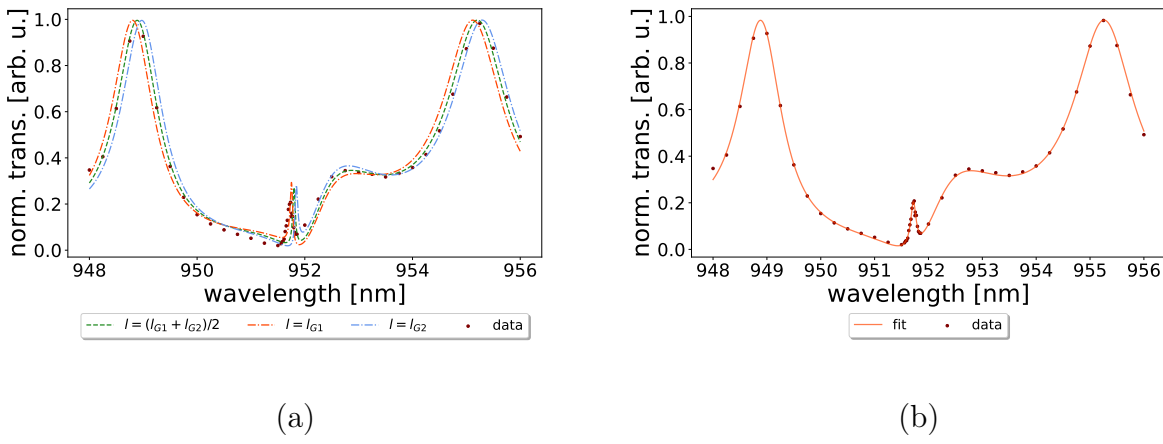


Figure 64: (a) shows recorded data of the double Fano cavity transmission compared with simulated spectra for cavity lengths of $l_{G1} = 140.4152\mu\text{m}$, $l_{G2} = 140.4401\mu\text{m}$, $(l_{G1} + l_{G2})/2 = 140.4277\mu\text{m}$. (b) shows a least squares fit of the recorded data to the double Fano cavity transmission function with fitting parameters related to each Fano mirror, and the cavity as follows.

Figure 64a show the comparison of data and simulation for a cavity of lengths given as $l_{G1} = 140.4152\mu\text{m}$, $l_{G2} = 140.4401\mu\text{m}$, $(l_{G1} + l_{G2})/2 = 140.4277\mu\text{m}$. Figure 64b shows a least squares fit of the data to the double Fano transmission function with fitting parameters related to each Fano mirror, and the cavity as follows.

Fitting parameters related to Fano mirror G1:

$$\begin{aligned}\lambda_0 &= 951.485 \pm 0.035\text{nm}, \quad \lambda_1 = 951.709 \pm 0.036\text{nm}, \quad t_d = 0.823 \pm 0.009, \\ \gamma_\lambda &= 0.549 \pm 0.039\text{nm}, \quad \beta = 1.187 \cdot 10^{-6} \pm 2.810 \cdot 10^{-7}\text{m}^{-1}.\end{aligned}\tag{68}$$

Fitting parameters related to Fano mirror G2:

$$\begin{aligned}\lambda_0 &= 951.799 \pm 0.020\text{nm}, \quad \lambda_1 = 951.852 \pm 0.0433\text{nm}, \quad t_d = 0.816 \pm 0.010, \\ \gamma_\lambda &= 0.548 \pm 0.043\text{nm}, \quad \beta = 8.335 \cdot 10^{-7} \pm 1.105 \cdot 10^{-7}\text{m}^{-1}.\end{aligned}\tag{69}$$

Fitting parameters related to the cavity configuration:

$$l = 139.003 \pm 0.001\mu\text{m}, \quad L = 0.143 \pm 0.037.\tag{70}$$

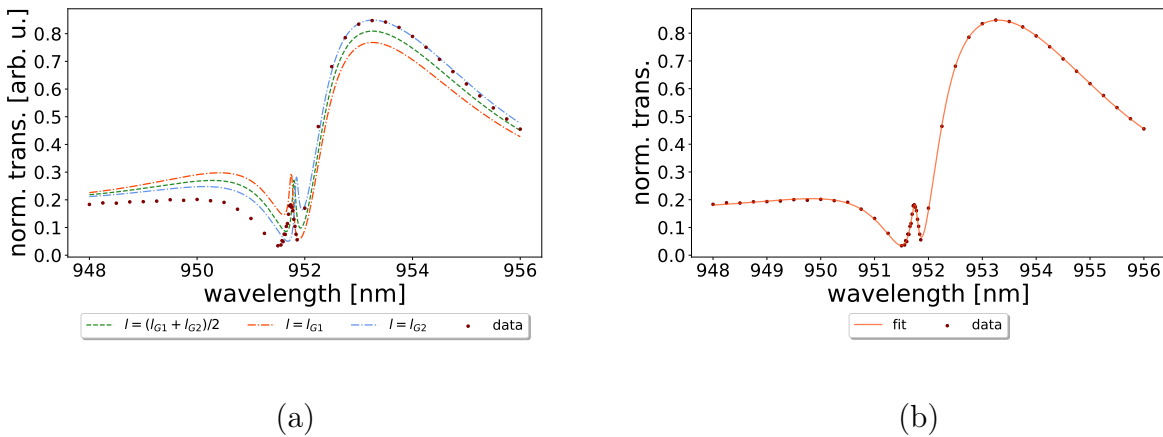


Figure 65: (a) shows recorded data of the double Fano cavity transmission compared with simulated spectra for cavity lengths of $l_{G1} = 33.3424\mu\text{m}$, $l_{G2} = 33.3573\mu\text{m}$, $(l_{G1} + l_{G2})/2 = 33.3499\mu\text{m}$. (b) shows a least squares fit of the recorded data to the double Fano cavity transmission model in eq. (37).

Figure 65a show the comparison of data and simulation for a cavity of lengths given as $l_{G1} = 33.3424\mu\text{m}$, $l_{G2} = 33.3573\mu\text{m}$, $(l_{G1} + l_{G2})/2 = 33.3499\mu\text{m}$. Figure 65b shows a least squares fit of the data to the double Fano transmission function with fitting parameters related to each Fano mirror, and the cavity as follows.

Fano mirror $G1$ fitting parameters:

$$\begin{aligned}\lambda_0 &= 951.532 \pm 0.008\text{nm}, \quad \lambda_1 = 951.689 \pm 0.074\text{nm}, \quad t_d = 0.817 \pm 0.027, \\ \gamma_\lambda &= 0.421 \pm 0.134\text{nm}, \quad \beta = 1.047 \cdot 10^{-6} \pm 4.947 \cdot 10^{-8}\text{m}^{-1}.\end{aligned}\tag{71}$$

Fano mirror $G2$ fitting parameters:

$$\begin{aligned}\lambda_0 &= 951.853 \pm 0.004\text{nm}, \quad \lambda_1 = 951.919 \pm 0.017\text{nm}, \quad t_d = 0.754 \pm 0.033, \\ \gamma_\lambda &= 0.563 \pm 0.079\text{nm}, \quad \beta = 5.245 \cdot 10^{-7} \pm 2.823 \cdot 10^{-8}\text{m}^{-1}.\end{aligned}\tag{72}$$

Cavity parameters:

$$l = 30.984 \pm 0.006\mu\text{m}, \quad L = 0.017 \pm 0.184.\tag{73}$$

Comparison with simulations

In all cases shown above the data and corresponding simulation shows remarkable overlap and agreement, as most data points are placed within, or very close to, the area enclosed by the simulations for the three considered cavity lengths. While this is only a qualitative measure, it indicates a high level of predictive strength of the model outlined in section 2.2 and eq. (37) and likewise for the experimental method used shown in section 3.3.

Fits to the double Fano model

All optical parameters for G1 and G2 found as fitting parameters of the double Fano model are approximately in agreement with the ones found for G1 and G2 in section 4.1 which are the used to simulate the transmission spectra and assumed the baseline for determining the validity of the values found in this section. While they are only approximately in agreement, the values tend to shift a little but based on the alignment of the experimental setup. With this in mind the optical parameters found provide a satisfactory foundation, along with the comparisons to the simulations, to conclude that the data recorded and analysed in fact realize the double Fano model proposed. Furthermore, the *coefficient of determination*, or r^2 -value of each of the fits are all >0.99 . The r^2 -value can also be credited to the large number of free parameters in the fitting function, but it is nonetheless strongly indicative that the data is well-described by the model.

4.3.2 The double fano linewidth

As for the single Fano cavity in section 4.2 I present resonance transmission spectra and compare the found linewidths with the ones of simulated spectra and the analytical model presented in eq. (38). The double Fano cavity realized is one comprised of Fano mirrors G1 and G2, characterized in section 4.1, in a plane-plane configuration placed normal to the optical axis. As the single Fano cavity was comprised of G1 and a HR broadband mirror, it is expected that the double Fano cavity produces spectra with broader linewidths due to the relatively higher losses. When comparing with the single Fano cavity linewidths, it must thus be noted that this is a single Fano cavity of similar losses as the double Fano cavity, and *not* the one presented in section 4.2.

Figure 66 show examples of off-resonance spectra of the double Fano cavity, with corresponding fits to the Fabry-Perot transmission function in order to determine the cavity length from the measured FSR. Figure 66a shows the off-resonance spectrum for a cavity of length $l = 17.04 \pm 0.23\mu m$, while figure 66b shows the same for a cavity of length $l = 539.10 \pm 2.33\mu m$. The errors are determined as the errors of the fit, found as the squareroot of the diagonal of the corresponding covariance matrices.

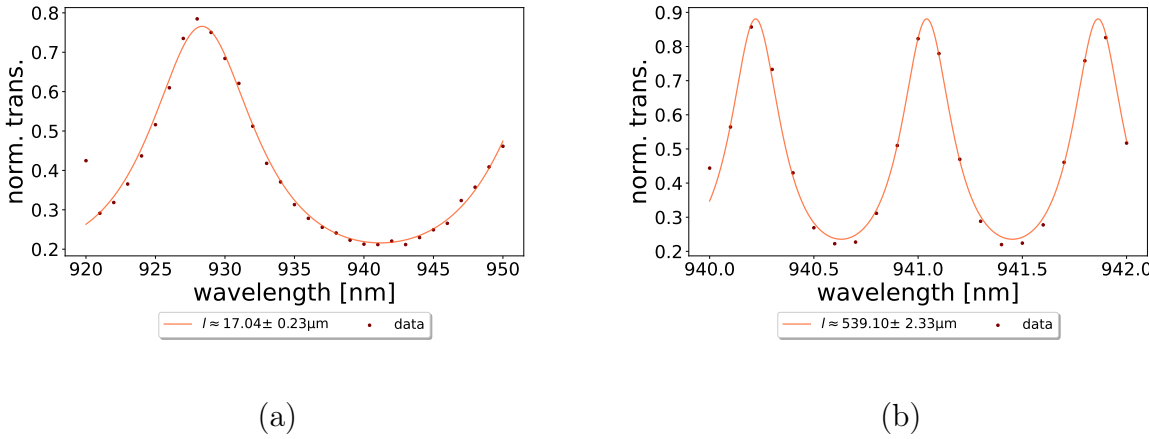


Figure 66: (a) shows an off-resonance wavelength scan of the double Fano cavity consisting of a G1 and G2 for a cavity length of $l = 17.04 \pm 0.23\mu m$. (b) shows this for a double Fano cavity of length $l = 539.10 \pm 2.33\mu m$. Each length is determined from these measurements by measuring the FSR and utilizing that $l = \lambda_0^2 / (2 \cdot FSR)$.

Figure 67 shows examples of resonance transmission spectra of the double Fano cavity. The examples are taken for length corresponding to the ones found from

the off-resonance spectra shown in figure 66 above. The figures are depicted with each their corresponding least squares fits to the generalized Fano model shown in eq. (33) in order to determine the linewidth (HWHM) of the profile. The errors of the linewidths are found from the error of each fit and are mainly used to determine the quality of the measurement.

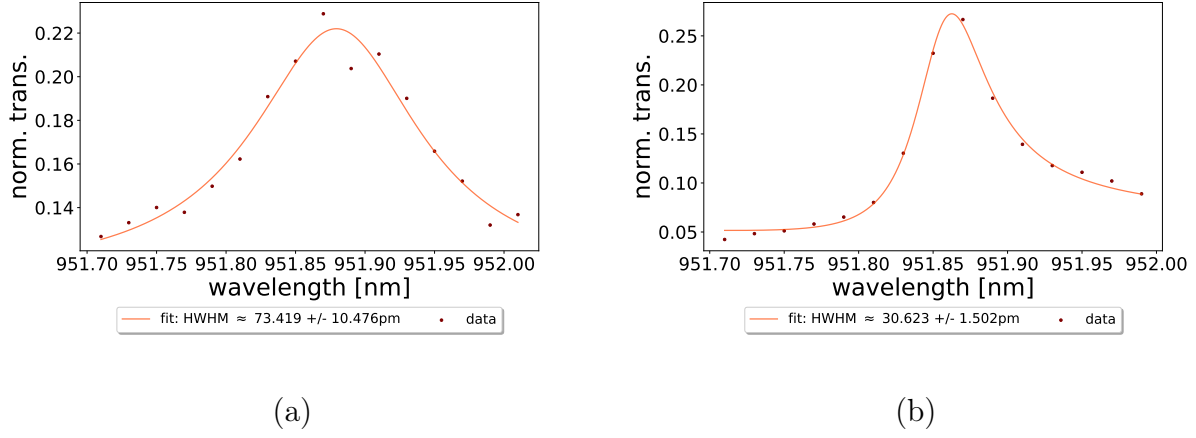


Figure 67: Double Fano resonance transmission profiles of a cavity consisting of Fano mirrors G1 and G2. (a) shows the profile of a cavity of length $l = 17.04 \pm 0.23\mu m$ and displays a linewidth of $HWHM = 73.419 \pm 10.476\text{pm}$. (b) shows the profile of a cavity of length $l = 539.10 \pm 2.33\mu m$, with a linewidth of $HWHM = 30.623 \pm 1.502\text{pm}$.

Figure 68 shows the average of results for the linewidths of a number of recorded spectra taken for cavity lengths in the approximate range $15\mu m \leq l \leq 1000\mu m$. The error of each data point depicted is determined as the standard deviation of all values found for the HWHM. The error in the x-direction, i.e. for the cavity lengths found from fits as the ones shown in figure 66 were of negligible size and are thus indicated rightly in the size of the data points themselves. The blue dashed line depict the analytical linewidth of a broadband cavity of losses similar to the double Fano cavity realized experimentally, the line is representative of eq. (35). The orange dashed line similarly shows the analytical linewidth of the single Fano cavity calculated using eq. (36) for a cavity of similar losses. Lastly, the green dashed line indicate the analytical linewidth of the double Fano cavity transmission spectra comparable with the data points depicted. The black points are linewidths found by fitting double Fano transmission profiles simulated using eq. (37) to the generalized Fano model in eq. (33) for comparison.

It is seen that the analytical and simulated linewidths are strongly correlated,

which indicates that both describe the transmission spectra well. This is also indicated in section 4.3.1 where the realization of the double Fano model is shown to correlate well with the spectra produced.

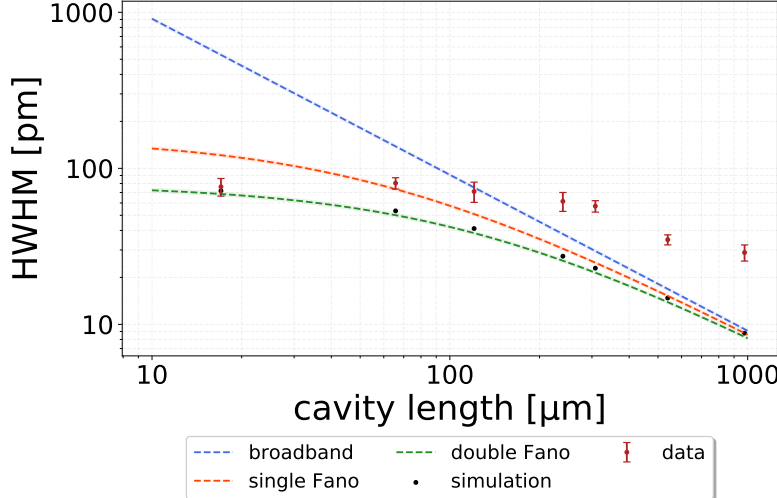


Figure 68: The linewidth (HWHM) as a function of resonant cavity length. The blue, orange and green dashed lines show the analytical linewidths of a broadband-, single Fano- and double Fano cavity of similar losses calculated using eqs. (35), (36) and (38) with the optical parameters for G1 and G2, respectively. The dark red point and corresponding errorbars shows the measured linewidths found as averages of all recorded values at each length and the error is found as the standard deviation of these. The black points are the linewidths of simulated spectra.

However, when examining the measured linewidths of the double Fano cavity resonance transmission profile, it is clear that it deviates from the analytical and simulated ones. The double Fano cavity has shown to be very sensitive to vibrational and acoustic noise, and this becomes more apparent when increasing the cavity length. Note that the correlation between the analytical and measured linewidths becomes correspondingly stronger for decreasing linewidths, and that they overlap almost completely when considering the spectra at $l \approx 17\mu m$. This indicates that analytical double Fano cavity linewidths are roughly realizable inside the Fano regime. It is also noted that the behavior of the measured linewidth as a function of cavity length follows the trend of the analytical one, indicating that the Fano- and standard regimes are still applicable for the double Fano cavity.

While vibrational and acoustic noise definitely claims their part of the reason for the experienced broadening, the method used in order to align the double Fano cavity outlined in section 3.2.1 has potential for improvement. When going through the process of aligning the cavity, one relies on the assumption that the top and bottom parts of the cavity setup can be removed and re-inserted without loss of alignment in either of the numerous degrees of freedom. This is of course not always the case and is therefore a cause of misalignment of the cavity and thus broadening.

Designing a setup with complete independent control of all degrees of freedom is therefore an area of improvement that could drastically reduce the discrepancy of the analytical/simulated and measured linewidths of the double Fano cavity resonance transmission spectra.

4.4 Additional discussion

4.4.1 Vibrational noise

The aforementioned vibrational noise was apparent from the intial iteration of the double Fano cavity setup and it was quickly concluded that it was specifically related to the modifications made to the single Fano cavity setup in order to be able to control additional degrees of freedom needed (spacial and rotational of the top part of the cavity setup seen in figure 35).

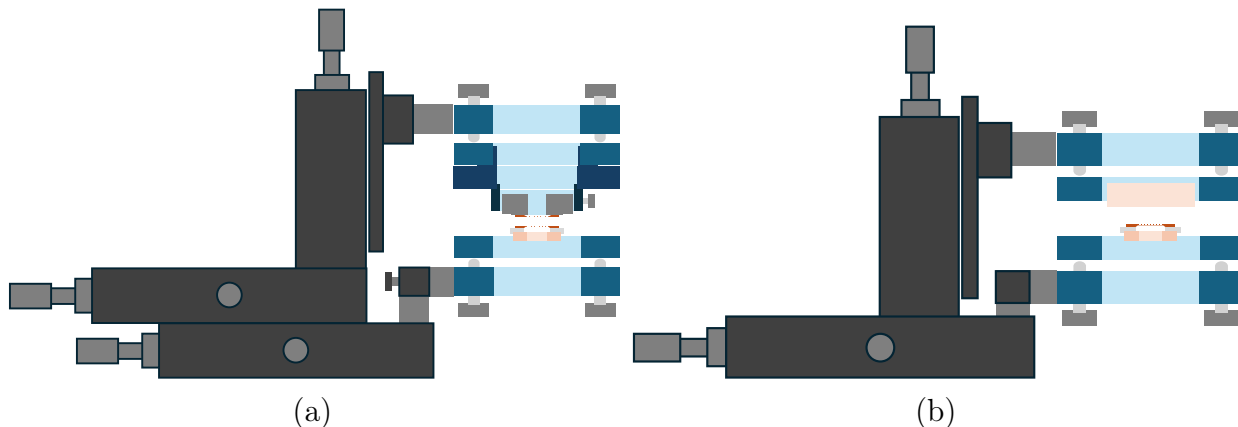


Figure 69: Simple sketches of the setups used to record the data shown in sections 4.2 and 4.3. (a) shows the double Fano cavity setup, and (b) shows the single Fano cavity setup.

Especially the spacial degrees of freedom seemed to be the source of the vibrations, as the need to control these for the bottom and top Fano mirrors

independently introduced the possibility of *uncoupled mechanical vibrations*. It is assumed that the noise was always apparent in the setup, but since the broadband- and Fano mirrors of the single Fano cavity only ever had the need for relative motion in the z-direction, this was never expressed as a change in the cavity length, and this was thus constant during measurements. The linear stage used in the z-direction (*NFL5DP20*) was specifically chosen to include a piezo actuator for high resolution motion control for very short cavity lengths, and this proved to be virtually stable in terms of vibrations. While a number of different stages, with a longer maximum travel range, was tested for the xy-directions, none proved stable enough to completely cancel the uncoupled vibrations. Figures 69 shows sketches of the single- and double Fano cavity setups and it is here shown how the top and bottom of the setup was *uncoupled* through the addition of the xy-stages for aligning the top Fano mirror, while for the single Fano setup they were *coupled* as they were both attached to the same set of xy-stages.

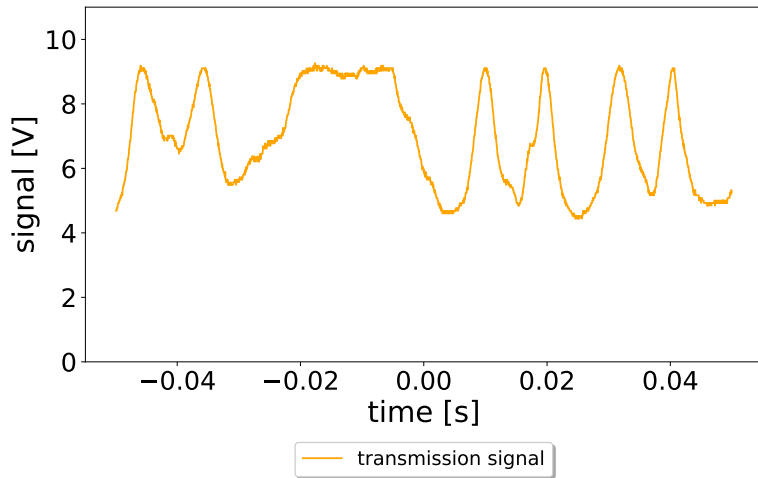


Figure 70: An example of the signal measured of the double Fano cavity transmission when manually scanning the piezo actuator to tune the cavity and guided-mode resonances. It is assumed that the cavity is resonant when the signal is maximized and the fluctuations is due to vibrational noise. This causes broadening and its effect is therefore apparent in the results presented.

Initially, the vibrations had an amplitude comparable with the free stroke of the piezo actuator. This means that the fringes stemming from scanning the cavity length would hardly change when turning off the alternating current applied

to the actuator, and thus a stable measurement was deemed impossible. At this point it was unclear whether the noise was acoustic in nature or if the vibrations originated somehow from the optical table. In order to rule out, or reduce, acoustic vibrations the setup was enclosed inside a plexi-glas box which was further equipped with a piece of noise reducing foam. This addition proved helpful as it roughly reduced the noise by a factor of 2, thus making the spectral profile resolvable and measurements possible.

Additional measures were taken in order to reduce any vibrations originating from the optical table by the addition of teflon slabs between the optical table and the first set of xy-stages, and between these and the second set of xy-stages. This further reduced the noise slightly and the resulting signal, shown as the raw data from the oscilloscope screen, is seen in figure 70.

It is assumed that the optimal cavity length is the one that produces the highest signal when the cavity length is constant. Keeping this in mind it is easily deduced from the figure that further noise reduction will increase the quality of the measured spectra. Since the intrinsically narrower linewidths of the longer optical cavity (both standard- and Fano cavities) makes these more sensitive to noise as the kind depicted in figure 70, this hints toward an explanation for the increased deviation from the analytical linewidth for longer cavity lengths seen in figure 68.

A brief decription of the plexi-glas box and teflon slabs are found in section 3.1.6.

Figure 71 shows the best obtained measurement series taken with the setup *without* teflon slabs, and while the cavity lengths considered does not range as far as the measurement series in figure 68, the trend of increased broadening in the standard regime is apparent. It also shows that even for the case of increased vibrational noise, it is possible to record spectra of linewidths in agreement with the analytical prediction, when inside the Fano regime. Note here that the errorbars on the figure are representative of the standard deviations of all values recorded at each cavity length, and thus the noisy measurement is seen to fluctuate more resulting in higher uncertainties.

4.4.2 Guided-mode resonance shift

The spectra for G1 and G2 shown in figure 54 are taken individually and in the intial part of the project where finding a matching pair of Fano mirrors was the

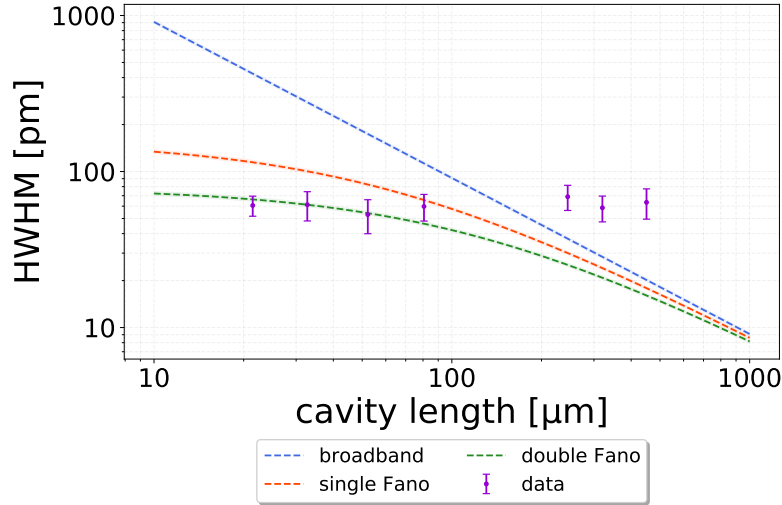


Figure 71: A measurement series showing the best obtained results for the double Fano cavity transmission linewidth as a function of resonant cavity length. This measurement series was recorded (before) the addition of the teflon slabs, which were added in an attempt to create a reflective interface to shield the cavity from vibrations propagating through the optical table.

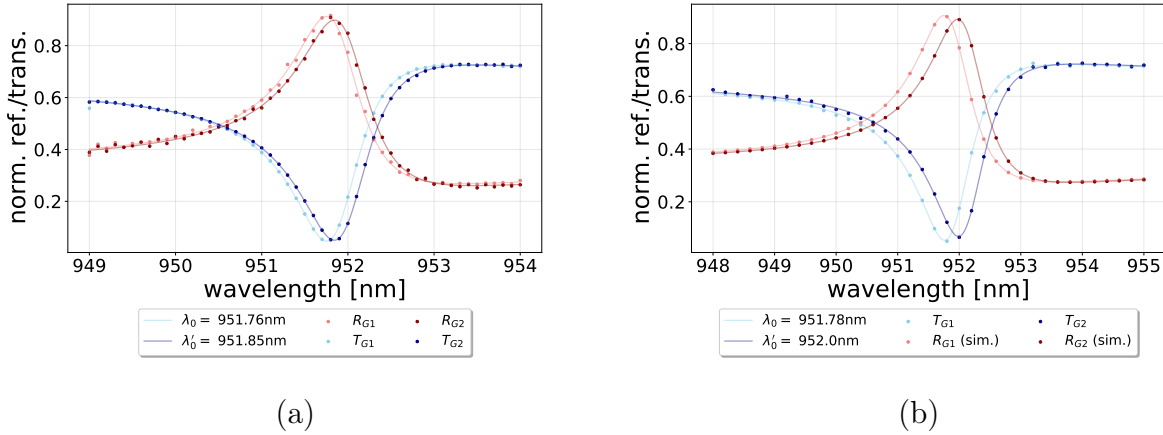


Figure 72: (a) shows spectra of G1 and G2 measured individually. (b) shows spectra of G1 and G2 in the double Fano configuration i.e. where G2 is upside down.

task at hand. Figure 72a shows, once again, the spectra of G1 and G2 taken individually, while figure 72b shows spectra taken for the two in the double Fano configuration, i.e. where G2 is placed upside down.

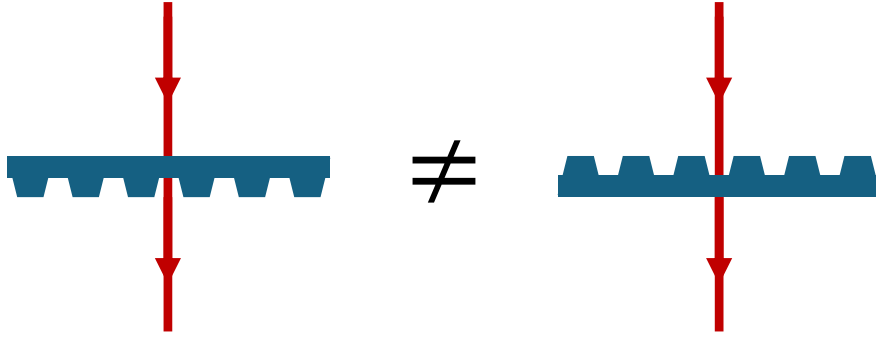


Figure 73: Sketch illustrating the discrepancy between measuring the spectra of a given Fano mirror for the scenario where the beam enters the bare SiN membrane first, then patterned SiN membrane, and the opposite scenario. It seems that the direction of incidence when characterizing the Fano mirrors shifts the guided-mode resonance wavelength slightly.

It is apparent that while the spectra for G1 is virtually unchanged, the same cannot be said for the spectra of G2 as this has clearly shifted to a slightly higher guided-mode resonance. This artifact of the double Fano cavity configuration has not been investigated in depth, but it can be argued that the interface from bare SiN into patterned SiN is not invariant from its opposite. The two scenarios are simply sketched in figure 73, outlining the claim that these somehow does not produce identical spectra.

4.4.3 Potential broadening due to walk-off effect

Another potential source of broadening is the so-called *walk-off effect* which is apparent, in this case, for the scenario of a wedge angle between G1 and G2. For a non-zero wedge angle the beam will be reflected inside the cavity and propagate according to said wedge angle as shown in figure 74, which would result in an effective change in beam waist and thus broadening of the recorded spectra.

A small, if not negligible, wedge angle is assumed for any experimentally realized cavity, but for the double Fano cavity with a non-zero detuning Δ this might be enhanced by the method it self. In [42] it is shown that the resonance wavelength will increase for a Fano mirror of a non-zero incident angle at the cost of a higher (lower) minimum (maximum) transmission (reflectivity) when on resonance. The argument can be made that the optimal double Fano configuration for a non-zero detuning is not necessarily normal to the optical axis, but rather at a wedge angle which optimizes the spectral overlap of the two

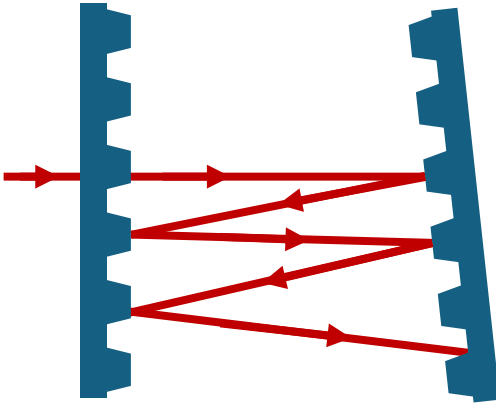


Figure 74: Sketch illustrating the walk-off effect between two Fano mirrors at a non-zero wedge angle.

Fano mirrors. For this reason the angle between G1 and G2 might be increased when on-resonance measurements are recorded and hence the walk-off effect might contribute to the broadening seen in figure 68. The walk-off effect will, if apparent, naturally increase with the cavity length, as a simple geometric consequence of the configuration considered.

5 Conclusion

This project have been a textbook example of an iterative process of improving results one parameter at a time, with methods including both numerical predictions and an experimental trial-and-error approach. We have been able to achieve an almost complete overlap between the Fano theory for a plane-wave and the recorded data, and while broadening is still present in the resonance transmission spectra, I confidently conclude that the double Fano model have been successfully realized.

Using suspended *SiN* membranes patterned with sub-wavelength gratings, utilized as TM_0 waveguides, we have successfully displayed an enhanced spectral sensitivity compared with a single Fano cavity of similar losses for short cavities, i.e. inside the Fano regime. It has been shown numerically that the double Fano cavity has the potential to produce linewidths similarly narrowed even for longer cavities, and the outlook of achieving this experimentaly is believed to belong in the near future.

The general behavior of the double Fano cavity has been thoroughly examined and documented through numerical simulations, once again assuming an incident plane-wave. The analytical model describing the linewidth of single- and double Fano cavities have likewise been studied and verified through both experimental and numerical results.

The realization of the double Fano cavity provides promise for a number of potential applications. These include, but are not limited to Fano cavity optomechanics, optical sensing and Fano lasers, and will be briefly outlines individually in the outlook section below.

5.1 Outlook

5.1.1 Matching analytical and experimental linewidths

I believe that the task of matching the analytical linewidth of the double Fano resonance transmission spectra with experimental data is one that consists of improving the method used and attempting to isolate the setup from vibrational noise stemming from outside sources. For this reason it is believed that this outlook is one that will be fulfilled in the near future.

5.1.2 Optomechanics with the double Fano cavity

This project have been dealing exclusively with the optical properties of the Fano mirrors. They are however often chosen for experiments in the field of cavity electrodynamics for their remarkable mechanical properties displaying high mechanical quality factors. Inside the Fano regime where the double Fano cavity linewidth is much narrower than for a similar broadband cavity of the same length, the radiation pressure is also high enough to excite mechanical modes in the high-Q *SiN* membranes. If placed inside a vacuum, the double Fano cavity is therefore an obvious candidate for studying optomechanical effects, e.g. the optical spring effect[36].

5.1.3 Sensing applications of the double Fano cavity

Various sensing applications using the bare *SiN* membranes are already being studied extensively. The isothermic compression of a gas in the free molecule regime inside a so-called membrane "sandwich" modifies the mechanical properties of the membranes due to the *squeeze film effect*. Figure 75 shows an example as a simple sketch of a double Fano cavity in a membrane "sandwich" configuration which can be utilized to measure absolute vapor pressure[22]. The change in mechanical properties of the Fano mirrors can then be recorded optically[20, 21].

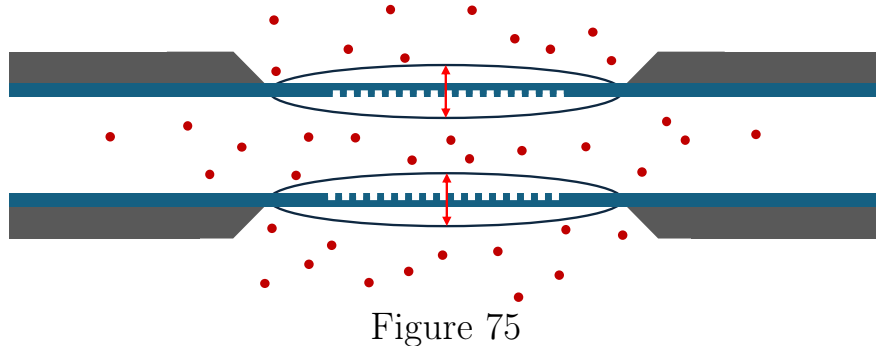


Figure 75

5.1.4 Fano laser based on bound states in the continuum

Firstly, a bound state in the continuum (BIC) is a state that remains localized while existing alongside a continuous spectrum of states that can provide and take away energy. They defy the general idea that states are either discrete or exist in a continuum. They are a relatively new discovery in the field of quantum mechanics, but have since been discovered to exist as a general wave phenomenon and can thus be utilized in numerous applications[53].

It has been proposed to utilize these BICs based on interference inside a cavity closely related to the double Fano cavity. This principle would allow for the construction of an ultra-coherent nanoscale laser, combating the limitation of quantum fluctuations, with potential applications in on-chip communication, photonic integrated circuits, bio/chemical sensing and quantum computing[54].

References

- [1] S. Haroche. “A short history of Cavity Quantum Electrodynamics”. In: *Optical Society of America* (2007).
- [2] J. J. Sakurai and J. Napolitano. *Modern Quantum Mechanics (3rd ed.)* Cambridge University Press, 2020.
- [3] Juliette Monsel et al. “Dissipative and dispersive cavity optomechanics with a frequency-dependent mirror”. In: *Phys. Rev. A* 109 (4 Apr. 2024), p. 043532. DOI: 10.1103/PhysRevA.109.043532. URL: <https://link.aps.org/doi/10.1103/PhysRevA.109.043532>.
- [4] J. C. Sankey et al. “Strong and tunable nonlinear optomechanical coupling in a low-loss system”. In: *Nature Physics* 6.9 (June 2010), pp. 707–712. ISSN: 1745-2481. DOI: 10.1038/nphys1707. URL: <http://dx.doi.org/10.1038/nphys1707>.
- [5] Kerry J. Vahala. “Optical microcavities”. In: *Nature* 424.6950 (2003), pp. 839–846.
- [6] J. D. Thompson et al. “Strong dispersive coupling of a high-finesse cavity to a micromechanical membrane”. In: *Nature* 452.7183 (2008), pp. 72–75.
- [7] A M Jayich et al. “Dispersive optomechanics: a membrane inside a cavity”. In: *New Journal of Physics* 10.9 (Sept. 2008), p. 095008. ISSN: 1367-2630. DOI: 10.1088/1367-2630/10/9/095008. URL: <http://dx.doi.org/10.1088/1367-2630/10/9/095008>.
- [8] D. J. Wilson et al. “Cavity Optomechanics with Stoichiometric SiN Films”. In: *Phys. Rev. Lett.* 103 (20 Nov. 2009), p. 207204. DOI: 10.1103/PhysRevLett.103.207204. URL: <https://link.aps.org/doi/10.1103/PhysRevLett.103.207204>.
- [9] Andrew T. Land et al. “Sub-ppm Nanomechanical Absorption Spectroscopy of Silicon Nitride”. In: *Nano Letters* 24.25 (May 2024), pp. 7578–7583. ISSN: 1530-6992. DOI: 10.1021/acs.nanolett.4c00737. URL: <http://dx.doi.org/10.1021/acs.nanolett.4c00737>.
- [10] Yannick Seis et al. “Ground state cooling of an ultracoherent electromechanical system”. In: *Nature Communications* 13.1 (2022), p. 1507.
- [11] Andrea Cupertino et al. “Centimeter-scale nanomechanical resonators with low dissipation”. In: *Nature Communications* 15.1 (2024), p. 4255.

- [12] T. Bagci et al. “Optical detection of radio waves through a nanomechanical transducer”. In: *Nature* 507.7490 (2014), pp. 81–85.
- [13] R. W. Andrews et al. “Bidirectional and efficient conversion between microwave and optical light”. In: *Nature Physics* 10.4 (2014), pp. 321–326.
- [14] Mitul Dey Chowdhury, Aman R. Agrawal, and Dalziel J. Wilson. “Membrane-Based Optomechanical Accelerometry”. In: *Phys. Rev. Appl.* 19 (2 Feb. 2023), p. 024011. DOI: 10.1103/PhysRevApplied.19.024011. URL: <https://link.aps.org/doi/10.1103/PhysRevApplied.19.024011>.
- [15] Jack Manley et al. “Searching for Dark Matter with an Optomechanical Accelerometer”. In: *Conference on Lasers and Electro-Optics*. Optica Publishing Group, 2021, STh2Q.2. DOI: 10.1364/CLEO_SI.2021.STh2Q.2. URL: https://opg.optica.org/abstract.cfm?URI=CLEO_SI-2021-STh2Q.2.
- [16] Elías Ferreiro-Vila et al. “Micro-Kelvin Resolution at Room Temperature Using Nanomechanical Thermometry”. In: *ACS Omega* 6.36 (Sept. 2021), pp. 23052–23058.
- [17] Chang Zhang et al. “Radiative Heat Transfer in Freestanding Silicon Nitride Membranes”. In: *Phys. Rev. Appl.* 14 (2 Aug. 2020), p. 024072. DOI: 10.1103/PhysRevApplied.14.024072. URL: <https://link.aps.org/doi/10.1103/PhysRevApplied.14.024072>.
- [18] Bhagya Nair. “Towards collective optomechanics with nanomembranes”. PhD thesis. Department of Physics and Astronomy - Aarhus University, 2017.
- [19] Sepideh Naserbakht and Aurélien Dantan. “Squeeze film pressure sensors based on SiN membrane sandwiches”. In: *Sensors and Actuators A: Physical* 298 (2019), p. 111588. ISSN: 0924-4247. DOI: <https://doi.org/10.1016/j.sna.2019.111588>. URL: <https://www.sciencedirect.com/science/article/pii/S0924424719310787>.
- [20] S. Al-Sumaidae et al. “Pressure sensing with high-finesse monolithic buckled-dome microcavities”. In: *Appl. Opt.* 60.29 (Oct. 2021), pp. 9219–9224. DOI: 10.1364/AO.438942. URL: <https://opg.optica.org/ao/abstract.cfm?URI=ao-60-29-9219>.

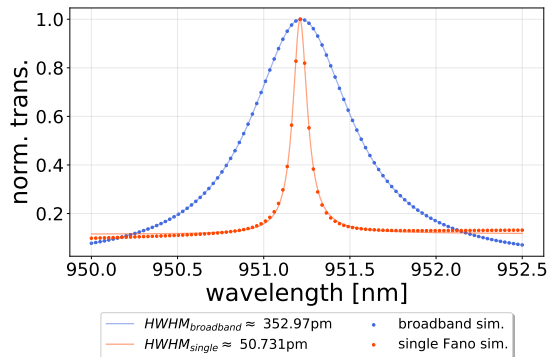
- [21] G. J. Hornig et al. “Ultrasound sensing at thermomechanical limits with optomechanical buckled-dome microcavities”. In: *Opt. Express* 30.18 (Aug. 2022), pp. 33083–33096. DOI: 10.1364/OE.463588. URL: <https://opg.optica.org/oe/abstract.cfm?URI=oe-30-18-33083>.
- [22] Mohsen Salimi et al. “Squeeze film absolute pressure sensors with sub-millipascal sensitivity”. In: *Sensors and Actuators A: Physical* 374 (Aug. 2024), p. 115450. ISSN: 0924-4247. DOI: 10.1016/j.sna.2024.115450. URL: <http://dx.doi.org/10.1016/j.sna.2024.115450>.
- [23] Utku Kemiktarak et al. “Mechanically compliant grating reflectors for optomechanics”. In: *Applied Physics Letters* 100.6 (Feb. 2012). ISSN: 1077-3118. DOI: 10.1063/1.3684248. URL: <http://dx.doi.org/10.1063/1.3684248>.
- [24] Utku Kemiktarak et al. “Cavity optomechanics with sub-wavelength grating mirrors”. In: *New Journal of Physics* 14.12 (Dec. 2012), p. 125010. DOI: 10.1088/1367-2630/14/12/125010. URL: <https://dx.doi.org/10.1088/1367-2630/14/12/125010>.
- [25] Catvu H. Bui et al. “High-reflectivity, high-Q micromechanical membranes via guided resonances for enhanced optomechanical coupling”. In: *Applied Physics Letters* 100.2 (Jan. 2012). ISSN: 1077-3118. DOI: 10.1063/1.3658731. URL: <http://dx.doi.org/10.1063/1.3658731>.
- [26] R. A. Norte, J. P. Moura, and S. Gröblacher. “Mechanical Resonators for Quantum Optomechanics Experiments at Room Temperature”. In: *Phys. Rev. Lett.* 116 (14 Apr. 2016), p. 147202. DOI: 10.1103/PhysRevLett.116.147202. URL: <https://link.aps.org/doi/10.1103/PhysRevLett.116.147202>.
- [27] Christoph Reinhardt et al. “Ultralow-Noise SiN Trampoline Resonators for Sensing and Optomechanics”. In: *Physical Review X* 6.2 (Apr. 2016). ISSN: 2160-3308. DOI: 10.1103/physrevx.6.021001. URL: <http://dx.doi.org/10.1103/PhysRevX.6.021001>.
- [28] Xu Chen et al. “High-finesse Fabry–Perot cavities with bidimensional Si₃N₄ photonic-crystal slabs”. In: *Light: Science & Applications* 6.1 (2017), e16190–e16190.
- [29] Feng Zhou et al. *Cavity optomechanical bistability with an ultrahigh reflectivity photonic crystal membrane*. 2022. arXiv: 2211.10485 [physics.optics]. URL: <https://arxiv.org/abs/2211.10485>.

- [30] Jipeng Xu et al. “Millimeter-scale ultrathin suspended metasurface integrated high-finesse optomechanical cavity”. In: *Optics Letters* 47 (Oct. 2022), pp. 5481–5484. DOI: 10.1364/OL.465567.
- [31] You Sang et al. “Spatial Nonreciprocal Transmission and Optical Bistability Based on Millimeter-Scale Suspended Metasurface”. In: *Advanced Optical Materials* 10 (Sept. 2022), p. 2201523. DOI: 10.1002/adom.202201523.
- [32] Georg Enzian et al. “Phononically shielded photonic-crystal mirror membranes for cavity quantum optomechanics”. In: *Optics Express* 31.8 (Apr. 2023), p. 13040. ISSN: 1094-4087. DOI: 10.1364/oe.484369. URL: <http://dx.doi.org/10.1364/OE.484369>.
- [33] Shanhui Fan and J. D. Joannopoulos. “Analysis of guided resonances in photonic crystal slabs”. In: *Physical Review B* 65 (2002).
- [34] Shanhui Fan, Wonjoo suh, and J. D. Joannopoulos. “Temporal coupled-mode theory for the Fano resonance in optical resonators”. In: *Optical Society of America* 20.3 (2003).
- [35] T. Mitra et al. “Narrow-linewidth Fano microcavities with resonant subwavelength grating mirror”. In: *Optics Express* 32.9 (2024).
- [36] Sushanth Kini Manjeshwar et al. “Integrated microcavity optomechanics with a suspended photonic crystal mirror above a distributed Bragg reflector”. In: *Opt. Express* 31.19 (Sept. 2023), pp. 30212–30226. DOI: 10.1364/OE.496447. URL: <https://opg.optica.org/oe/abstract.cfm?URI=oe-31-19-30212>.
- [37] Marc Eichhorn. *Laser Physics - From Principles to Practical Work in the Lab*. Springer International Publishing Switzerland, 2014.
- [38] Frank L. Pedrotti, Leno M. Pedrotti, and Leno S. Pedrotti. *Introduction to Optics, 3rd edition*. Cambridge University Press, 2018.
- [39] U. Fano. “Effects of Configuration Interaction on Intensities and Phase Shifts*”. In: *Physical Review* 124.6 (1961).
- [40] Dmitry A. Bykov and Leonid L. Doskolovich. “Spatiotemporal coupled-mode theory of guided-mode resonant gratings”. In: *Optical Society of America* 14.3 (2015).
- [41] A. A. Darki et al. “Profilometry and stress analysis of suspended nanosstructured thin films”. In: *Journal of Applied Physics* (2021).

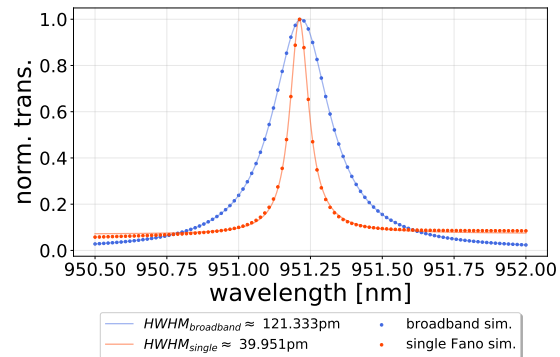
- [42] A. Parthenopoulos et al. “Optical spatial differentiation with suspended subwavelength gratings”. In: *Optics Express* 29.5 (2021).
- [43] E. Popov, L. Mashev, and D. Maystre. “Theoretical Study of the Anomalies of Coated Dielectric Gratings”. In: *Optica Acta: International Journal of Optics* 33.5 (1986).
- [44] URL: <https://pages.nist.gov/ScatterMIST/docs/index.htm>.
- [45] C. Toft-Vandborg et al. “Collimation and finite-size effects in suspended resonant guided-mode gratings”. In: *Journal of the Optical Society of America* 38.11 (2021).
- [46] Ali Akbar Darki. “Nanostructured trampolines for photonics and sensing”. PhD thesis. Department of Physics and Astronomy - Aarhus University, 2022.
- [47] A. Naesby and A. Dantan. “Microcavities with suspended subwavelength structured mirrors”. In: *Optics Express* 26.23 (2018).
- [48] URL: <https://www.edmundoptics.com/knowledge-center/application-notes/optics/understanding-waveplates/>.
- [49] S. Yu. Sadov and K. A. McGreer. “Polarization dependence of diffraction gratings that have total internal reflection facets”. In: *J. Opt. Soc. Am. A* 17.9 (2000).
- [50] M. Forster et al. “213 nm and 532 nm solid state laser treatment of biogenetical fibrous materials”. In: (2010).
- [51] Ifan G. Hughes and Thomas P.A. Hase. *Measurements and their Uncertainties - A Practical Guide to Modern Error Analysis*. Oxford University Press, 2010.
- [52] B. Nair, A. Naesby, and A. Dantan. “Optomechanical characterization of silicon nitride membrane arrays”. In: *Optics Letter* 42.7 (2017).
- [53] Chia Wei Hsu et al. “Bound states in the continuum”. In: *Nature Reviews Materials* 1.9 (2016), p. 16048.
- [54] Yi Yu et al. “Ultra-coherent Fano laser based on a bound state in the continuum”. In: *Nature Photonics* 15.10 (2021), pp. 758–764.

Appendix

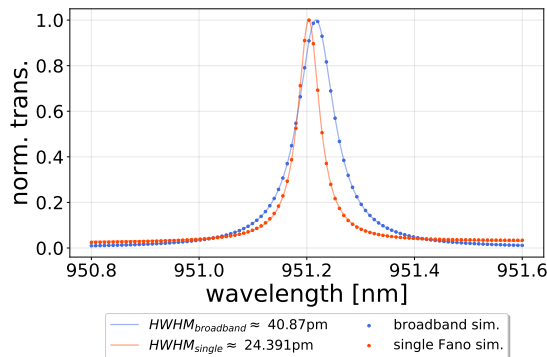
A Simulated broadband and single Fano cavity resonance transmission spectra (Figure 11a in section 2.3.2)



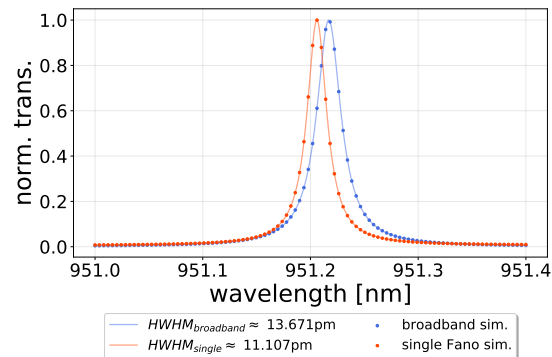
(a)



(b)



(c)



(d)

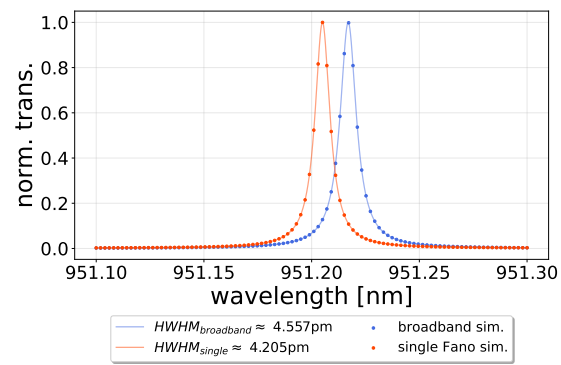


Figure 76

B Simulated single and double Fano cavity resonance transmission spectra

(Figure 15a in section 2.4.3)

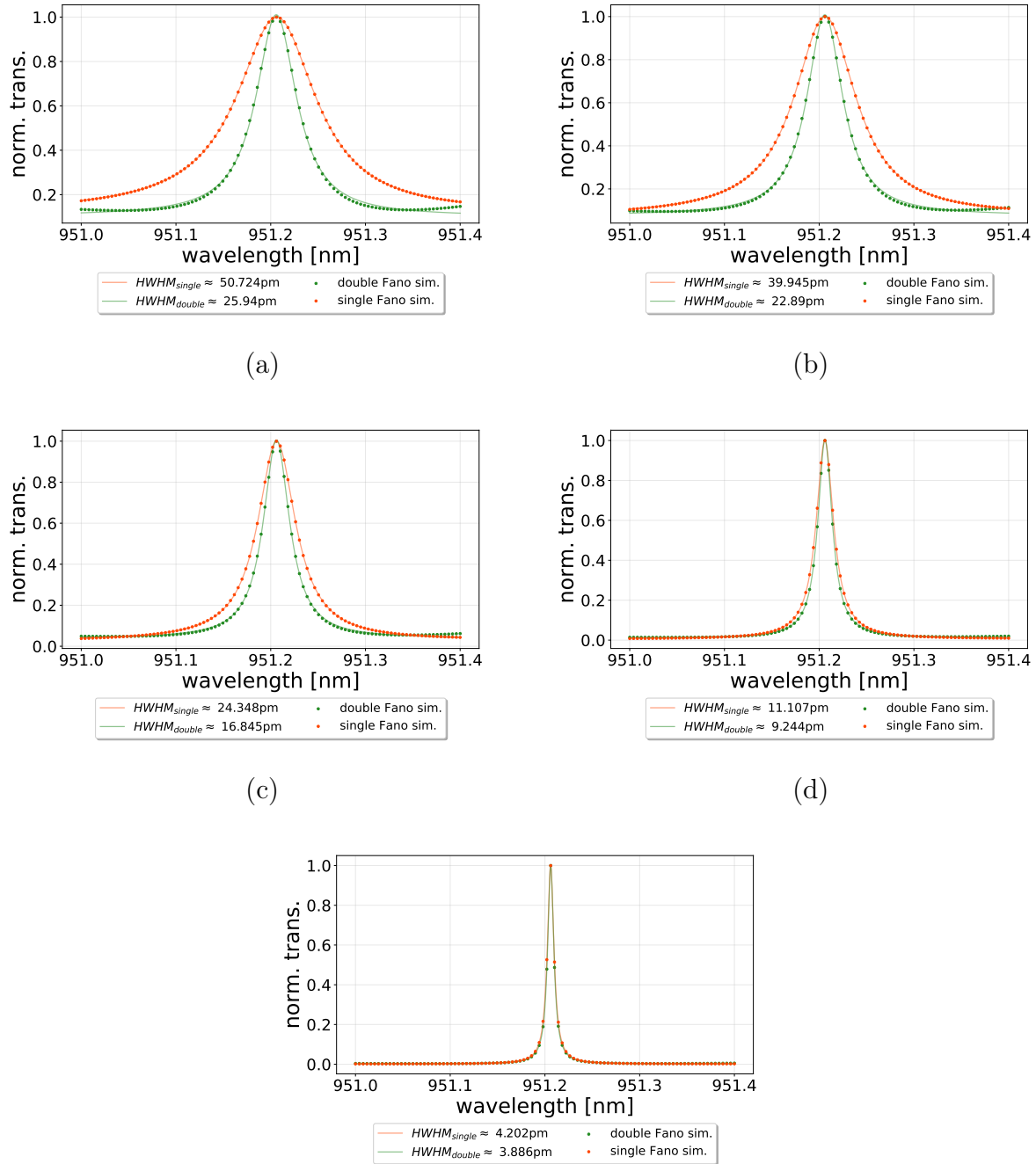
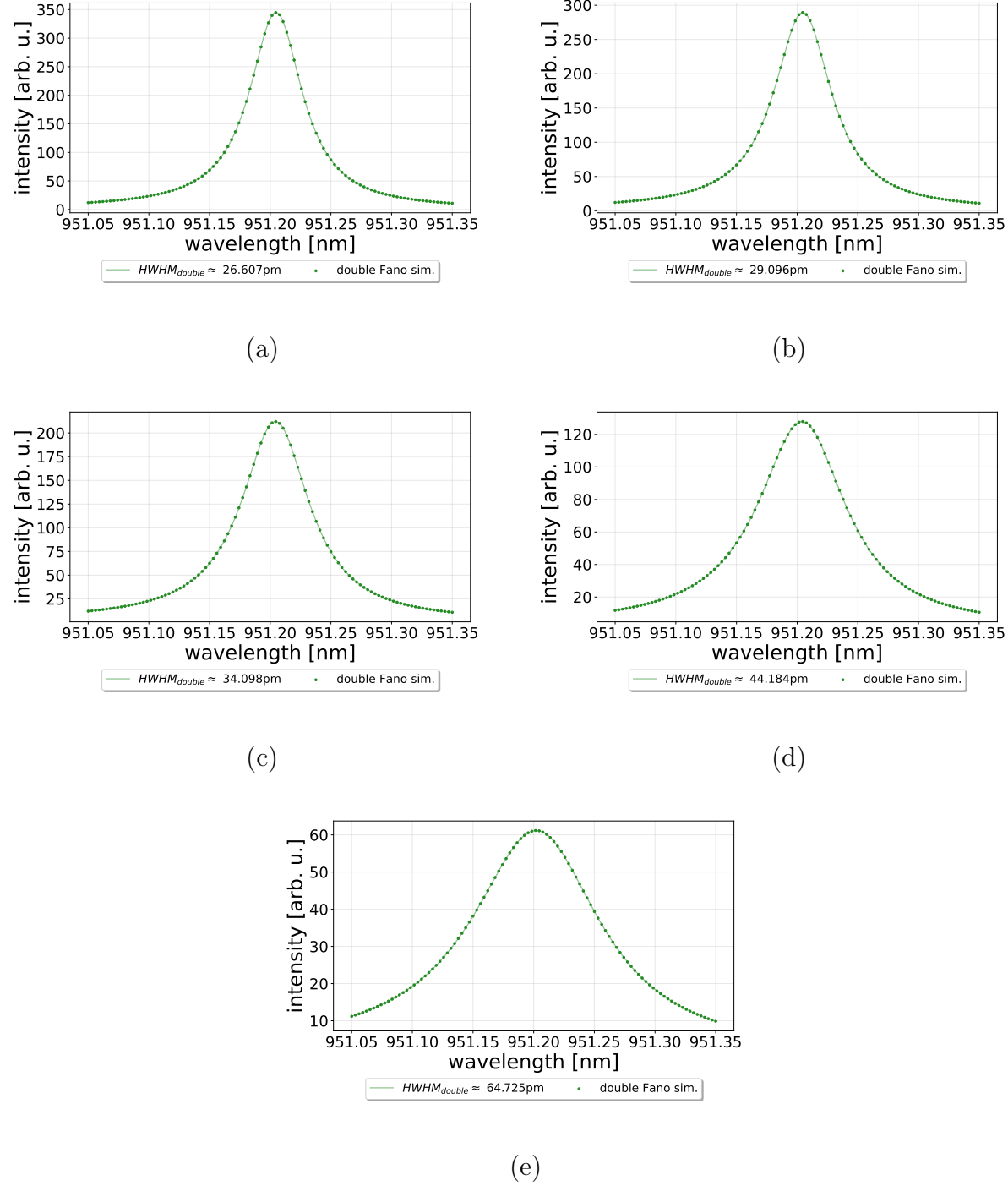


Figure 77

C Simulated double Fano cavity resonance transmission spectra for different values of the resonant loss term

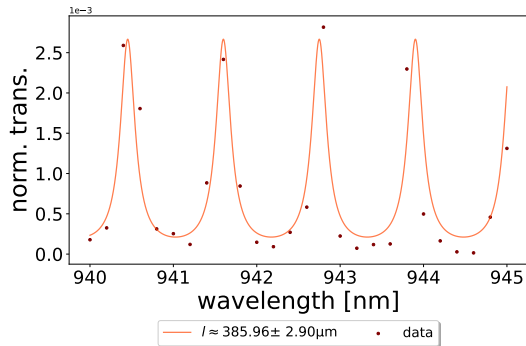
(Figure 17 in section 2.4.4)



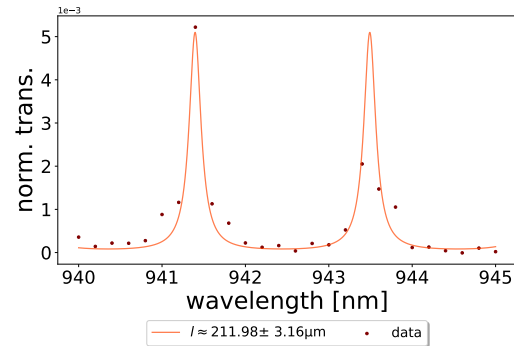
D Measured single Fano transmission data

(Figure 58 in section 4.2)

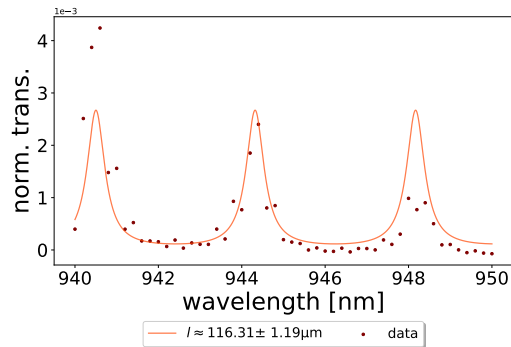
Off-resonance spectra (determining the cavity length)



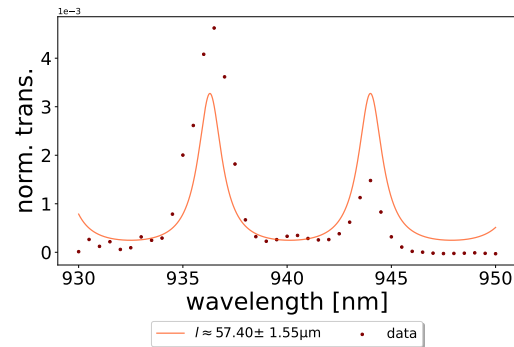
(a)



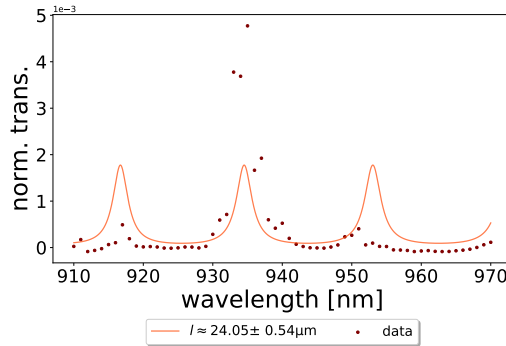
(b)



(c)

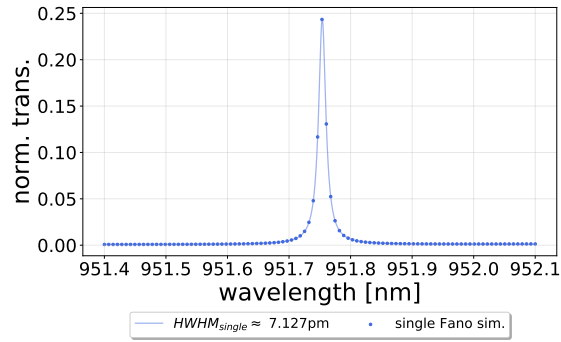


(d)

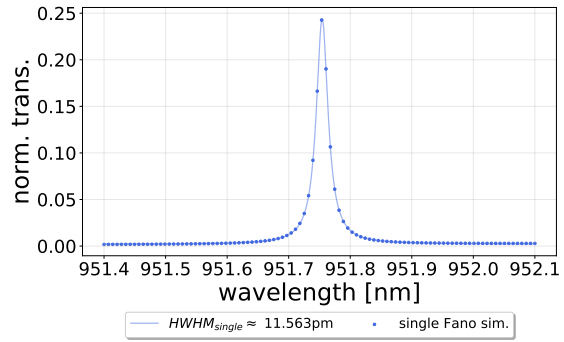


(e)

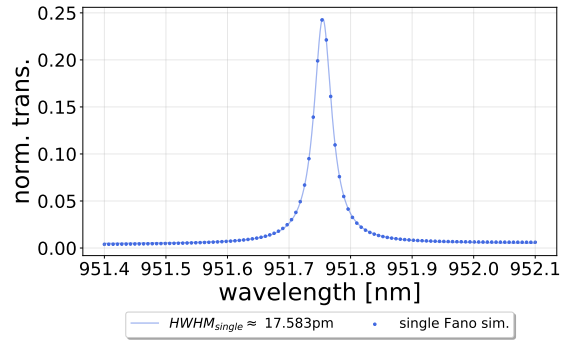
Simulated spectra



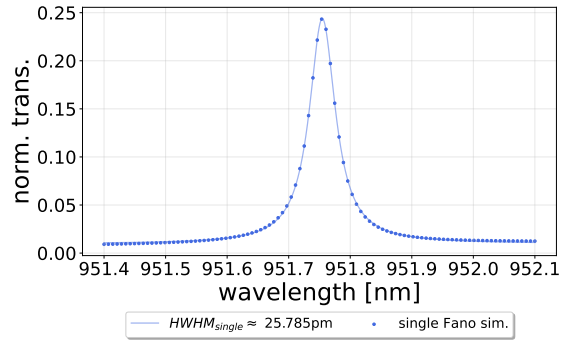
(a)



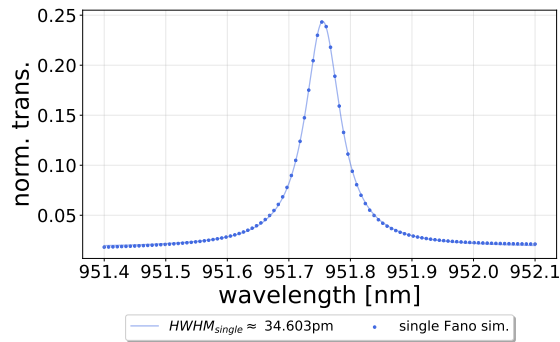
(b)



(c)

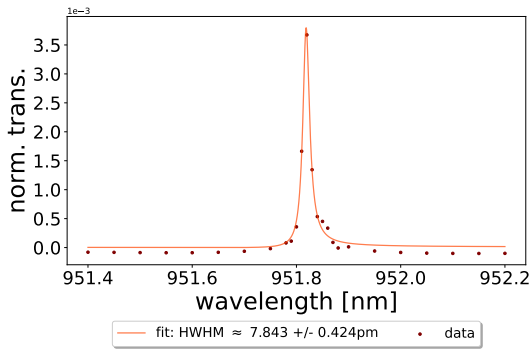


(d)

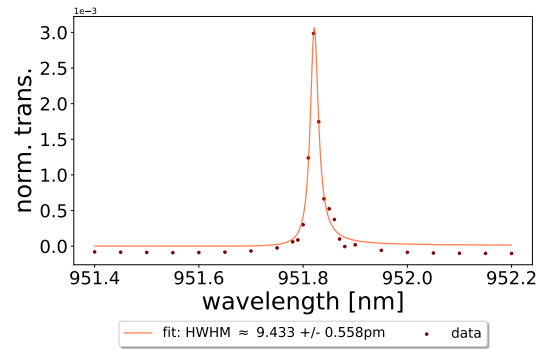


(e)

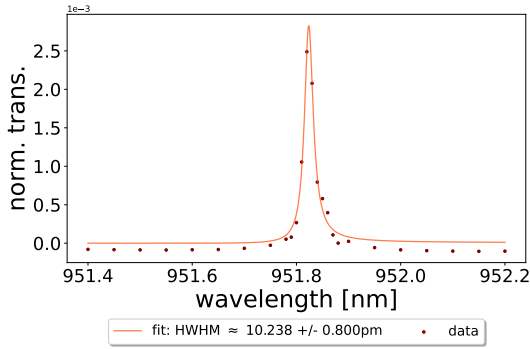
cavity length: $l \approx 386\mu m$



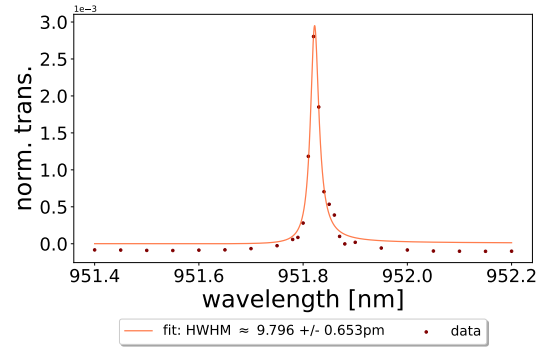
(a)



(b)

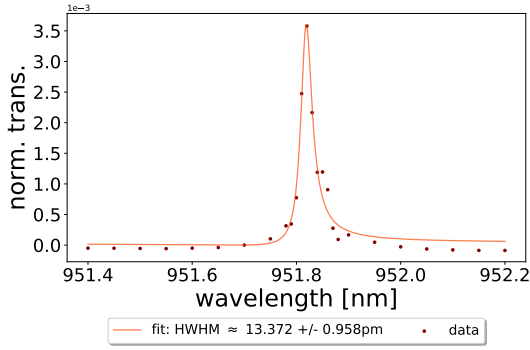


(c)

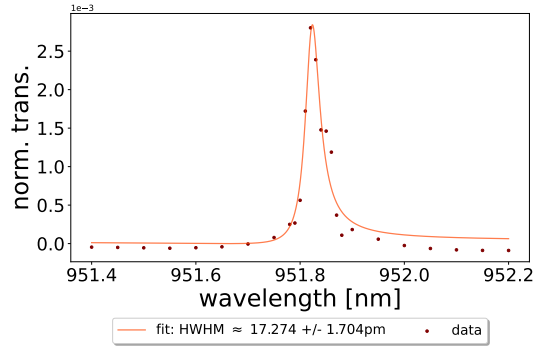


(d)

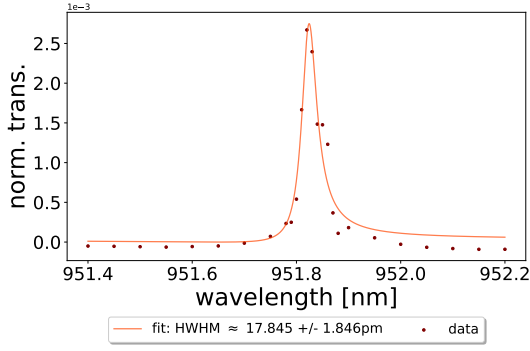
cavity length: $l \approx 212\mu m$



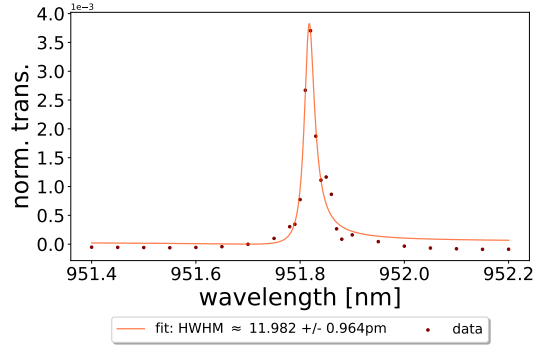
(a)



(b)

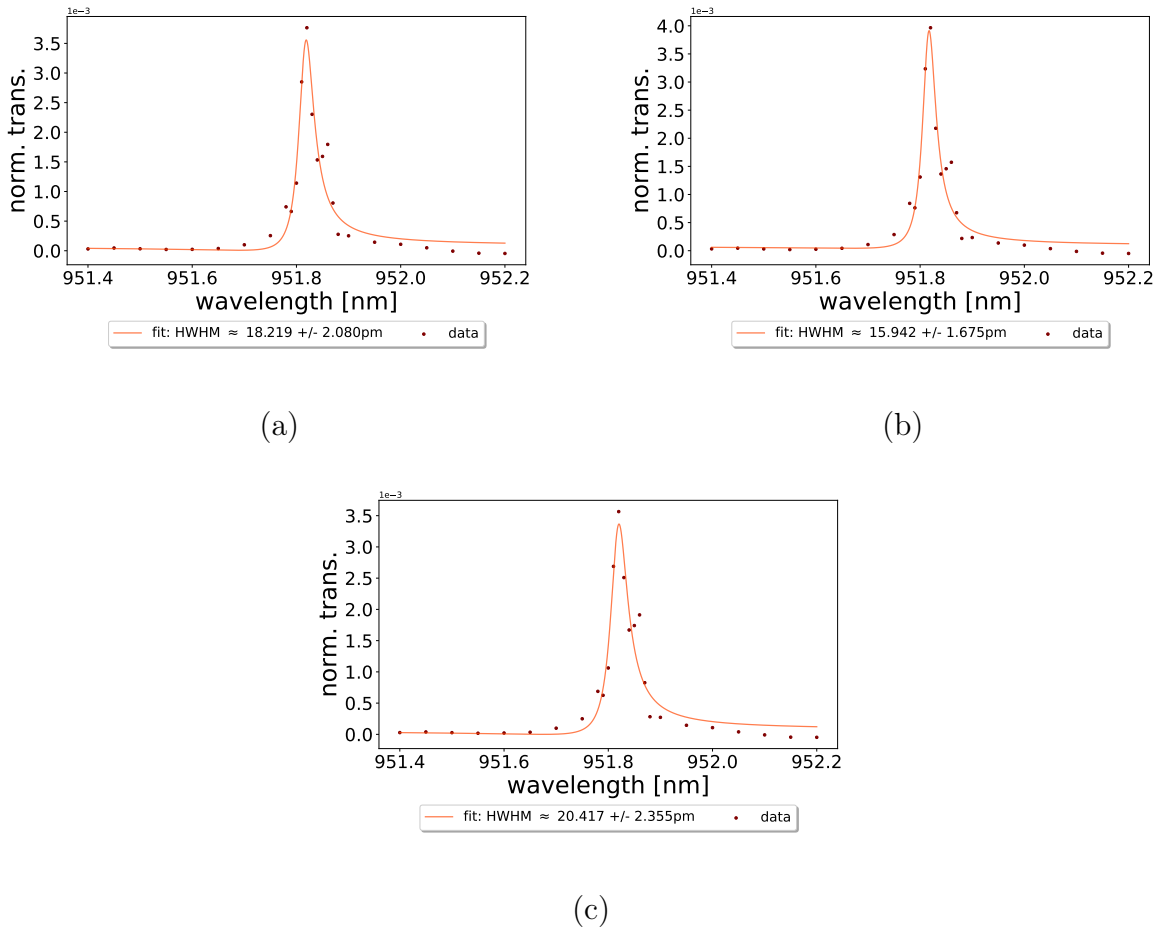


(c)

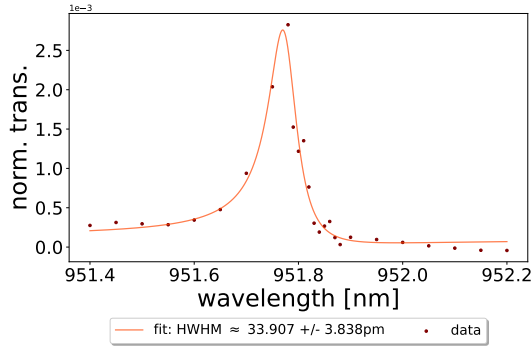


(d)

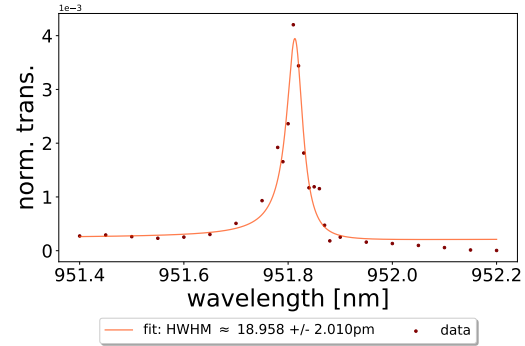
cavity length: $l \approx 116\mu m$



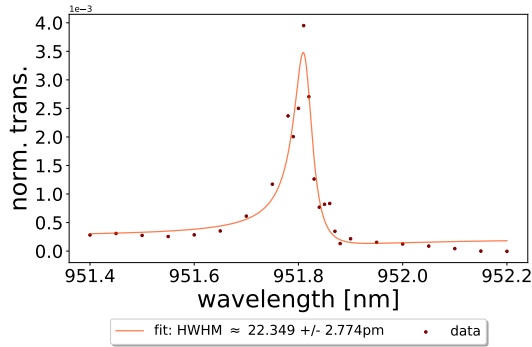
cavity length: $l \approx 57\mu m$



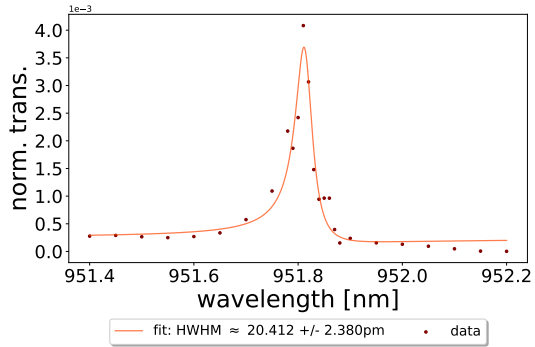
(a)



(b)

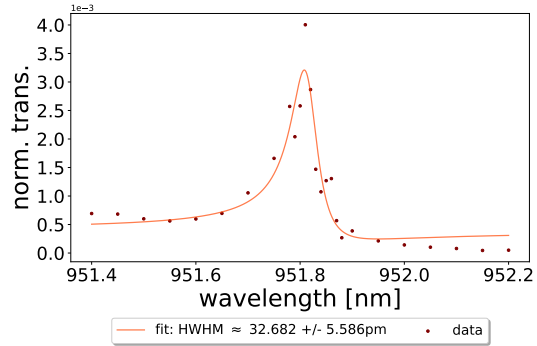
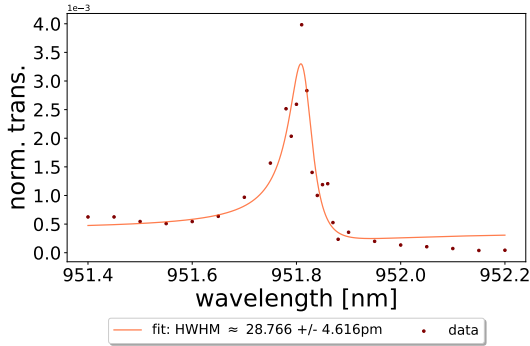


(c)



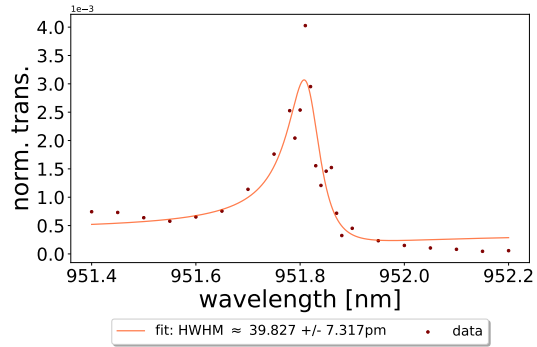
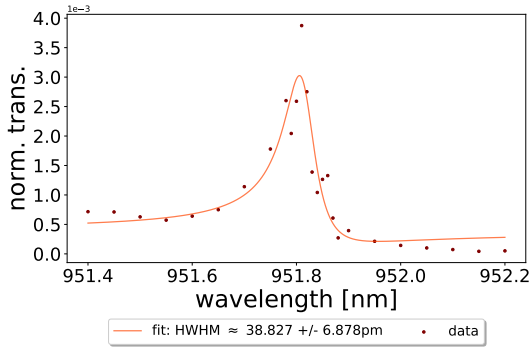
(d)

cavity length: $l \approx 24\mu m$



(a)

(b)



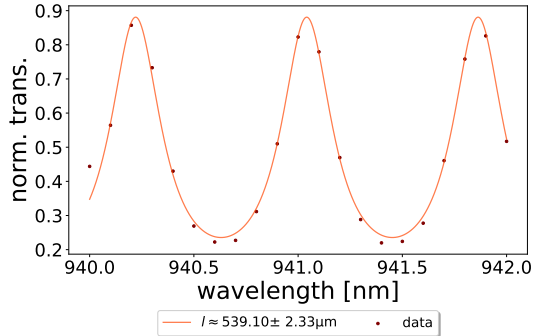
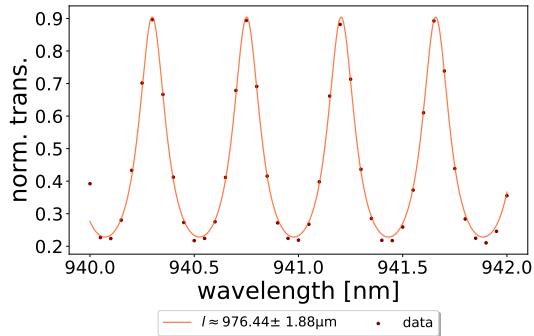
(c)

(d)

E Measured double Fano transmission data

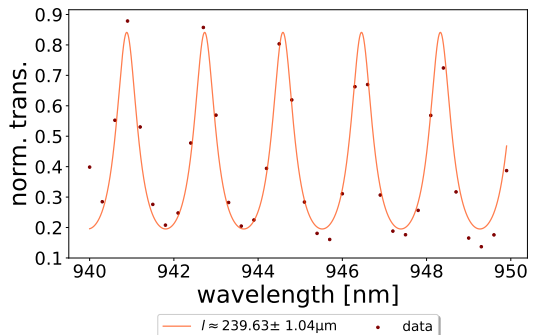
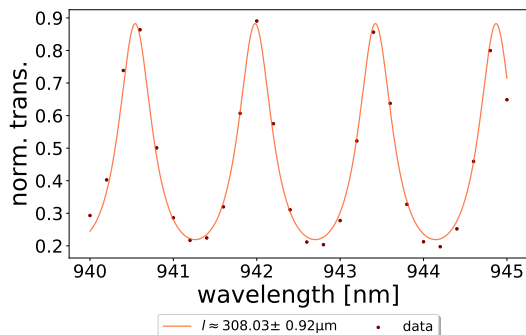
(Figure 68 in section 4.3)

Off-resonance spectra (determining the cavity length)



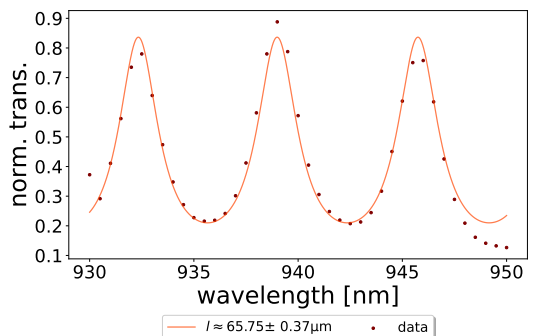
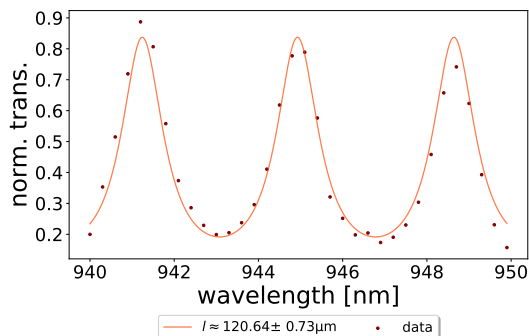
(a)

(b)



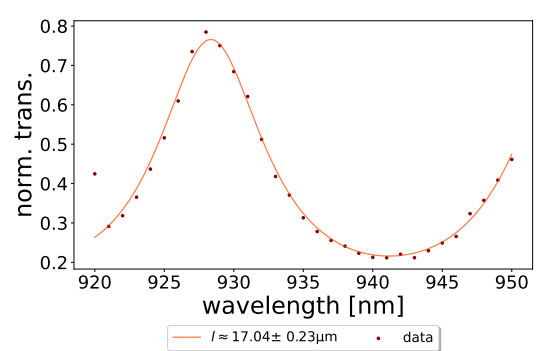
(c)

(d)



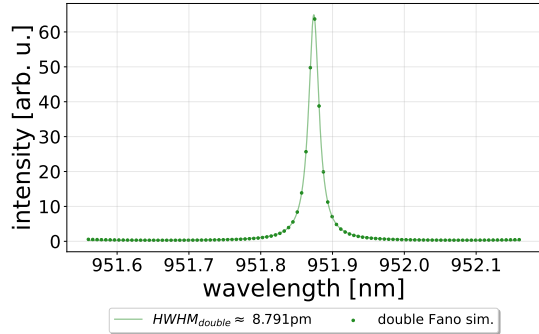
(e)

(f)

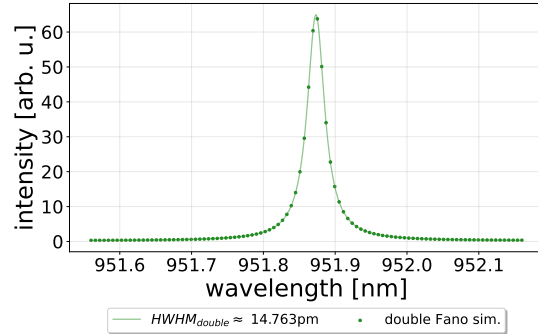


(g)

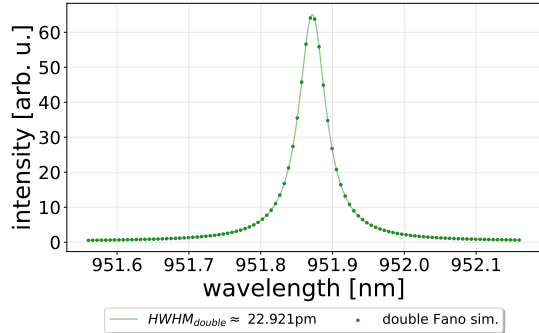
Simulated spectra



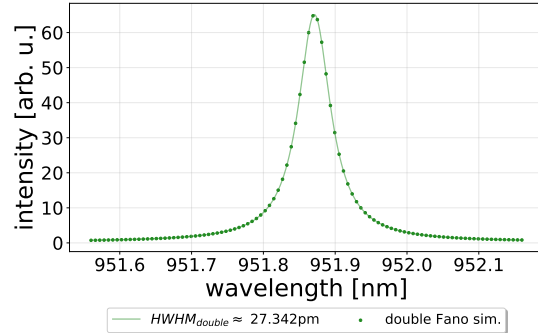
(a)



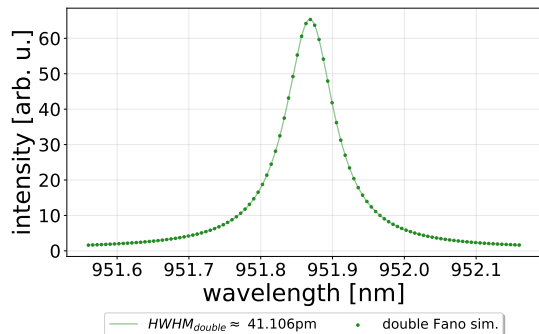
(b)



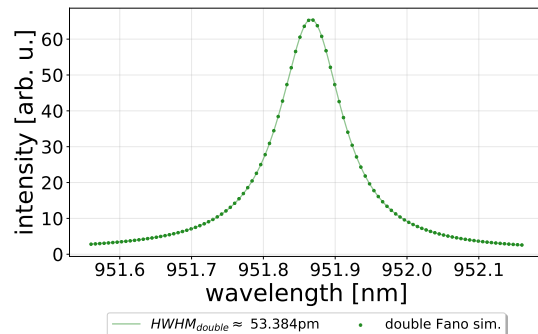
(c)



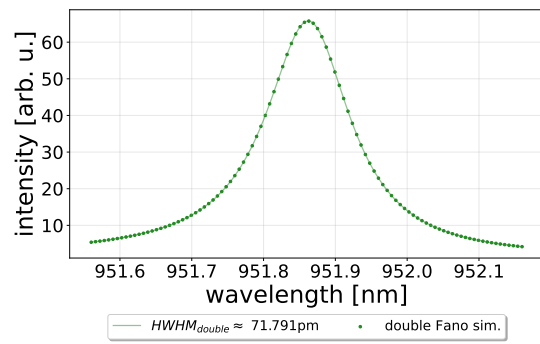
(d)



(e)

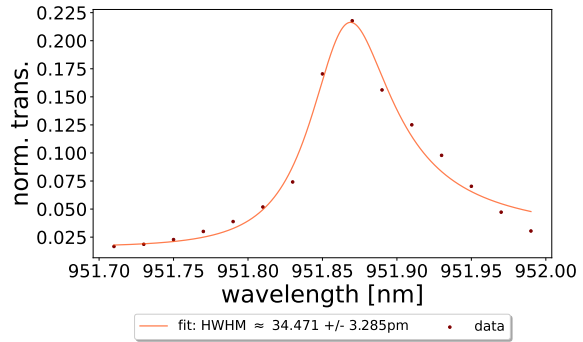


(f)

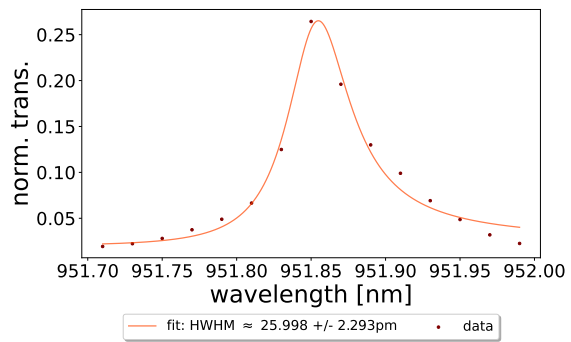


(g)

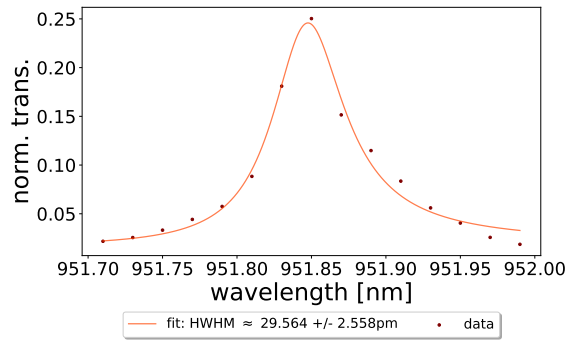
cavity length: $l \approx 976\mu m$



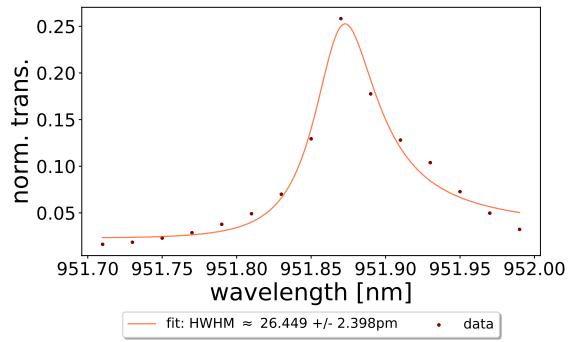
(a)



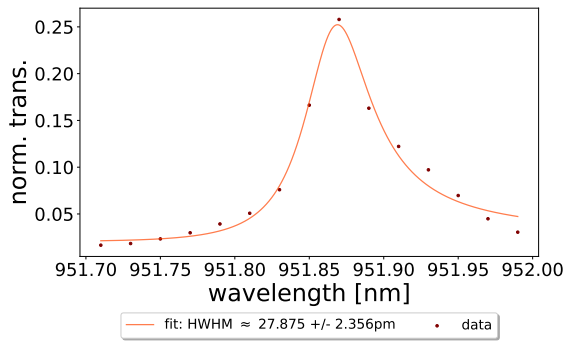
(b)



(c)

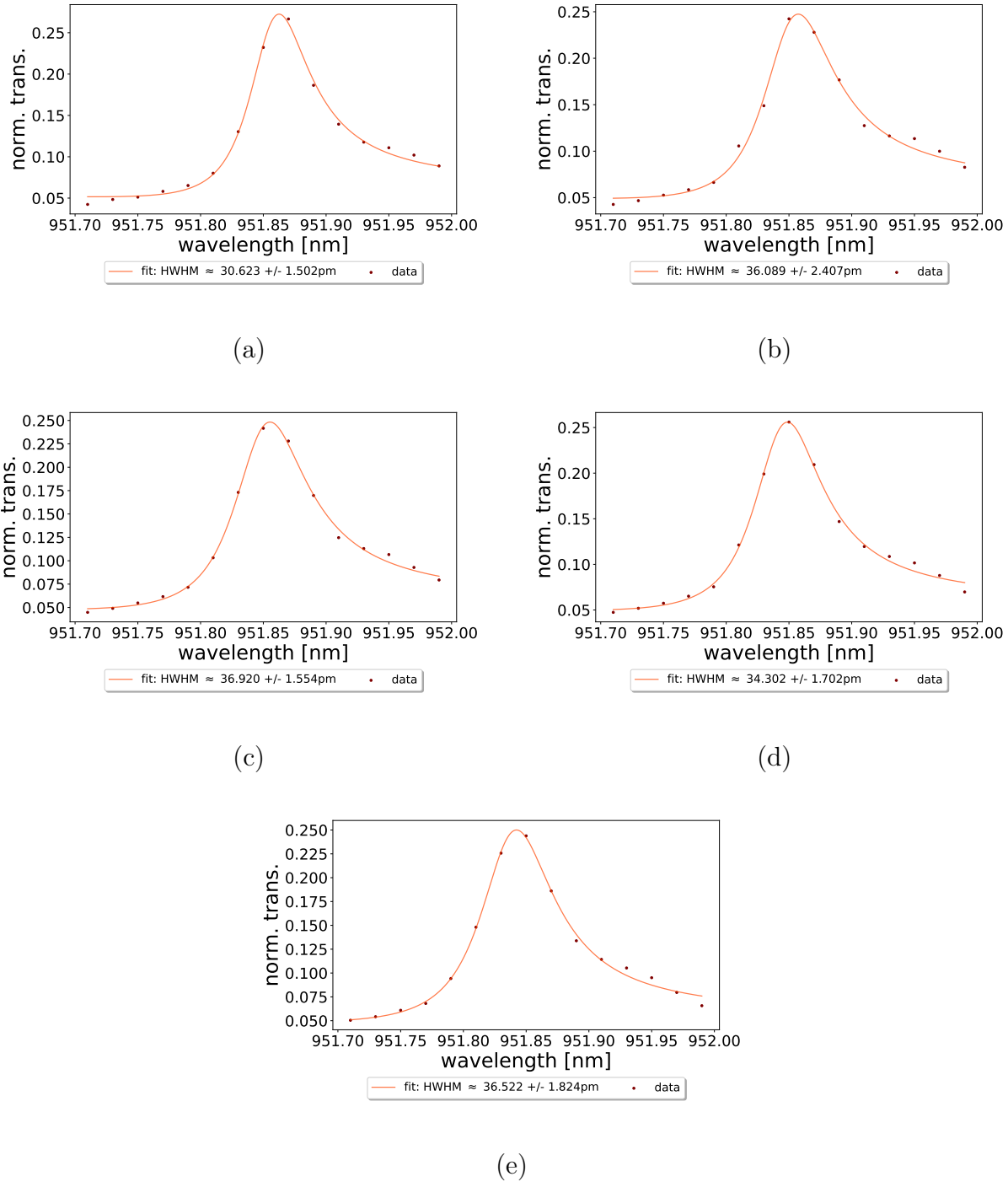


(d)

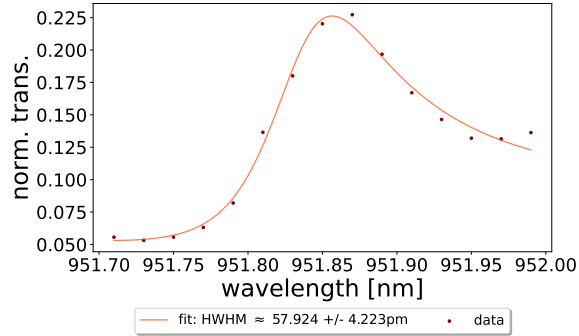


(e)

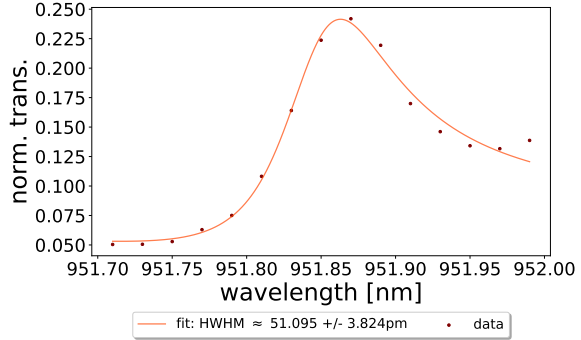
cavity length: $l \approx 539\mu m$



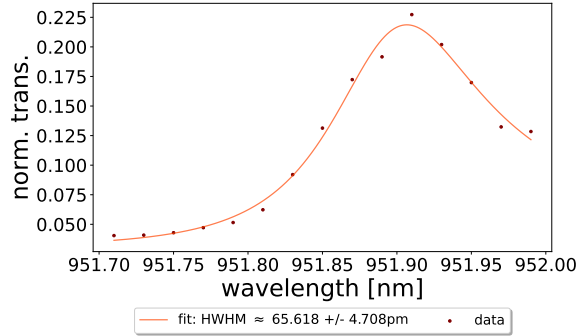
cavity length: $l \approx 308\mu m$



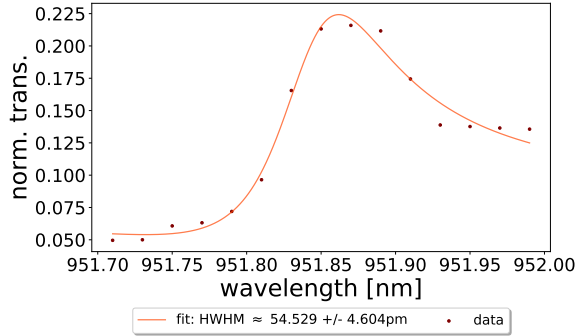
(a)



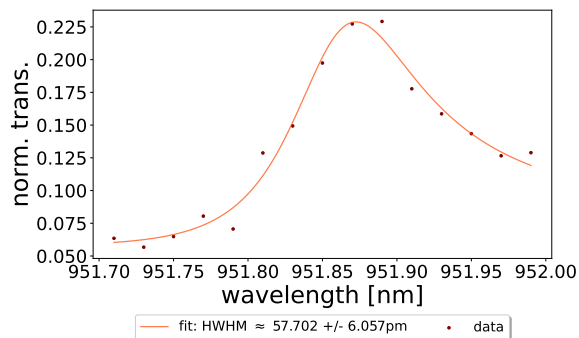
(b)



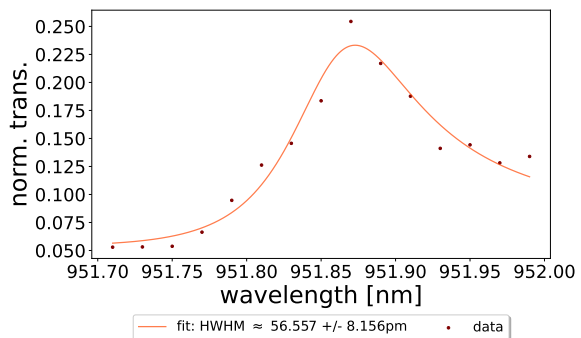
(c)



(d)

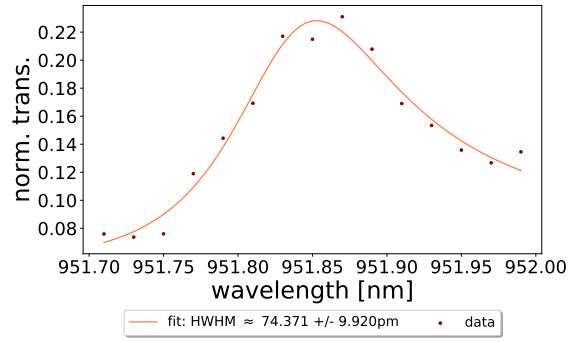


(e)

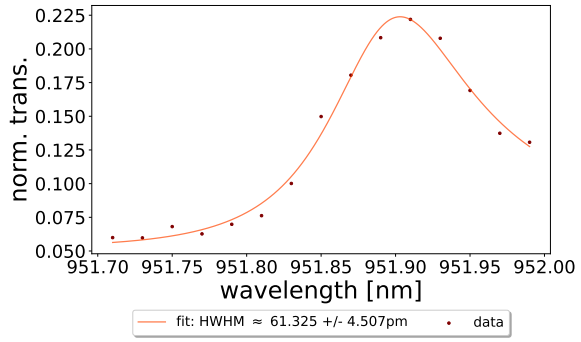


(f)

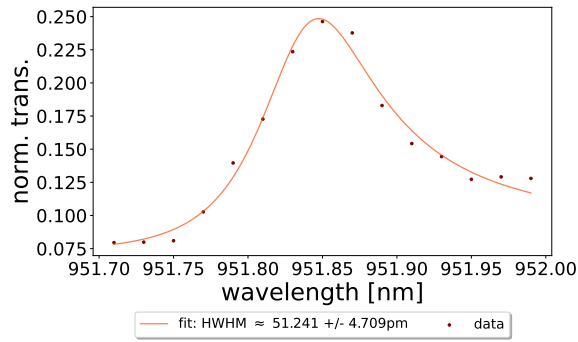
cavity length: $l \approx 239\mu m$



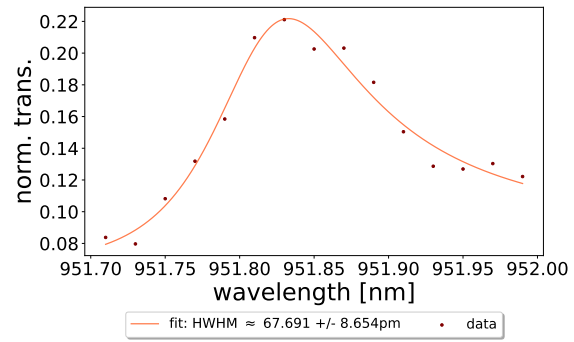
(a)



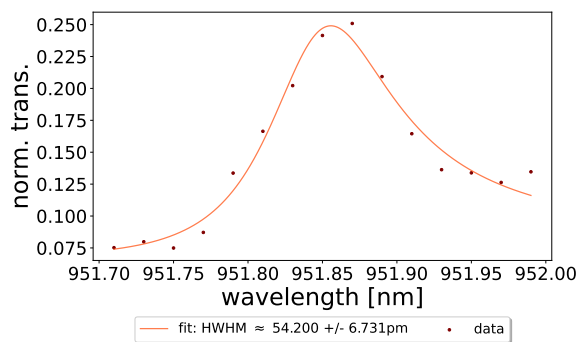
(b)



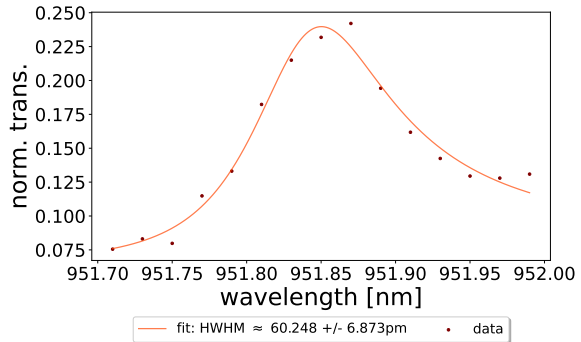
(c)



(d)

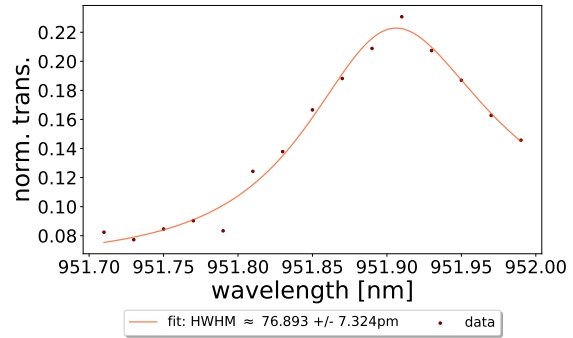


(e)

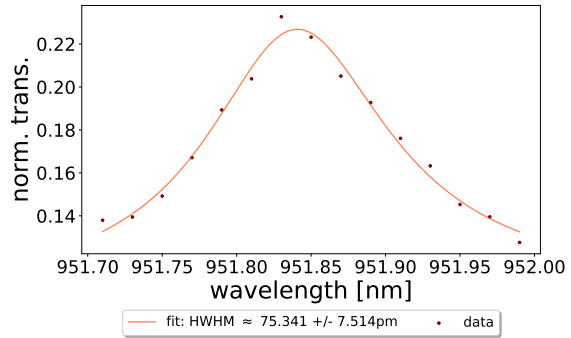


(f)

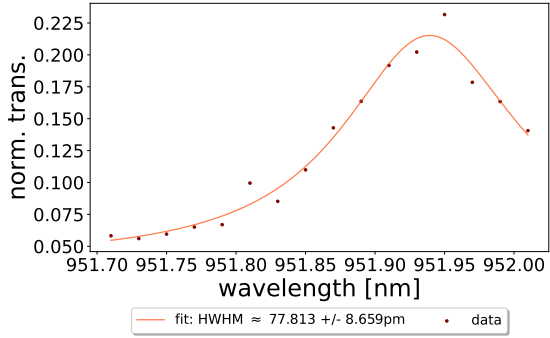
cavity length: $l \approx 121\mu m$



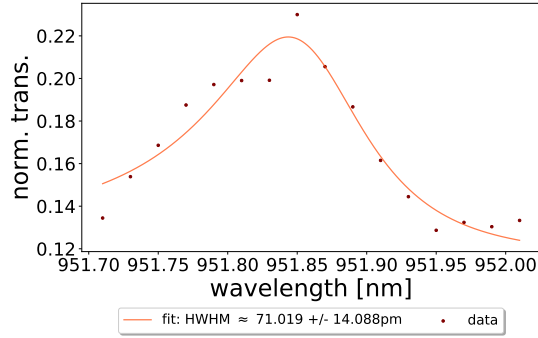
(a)



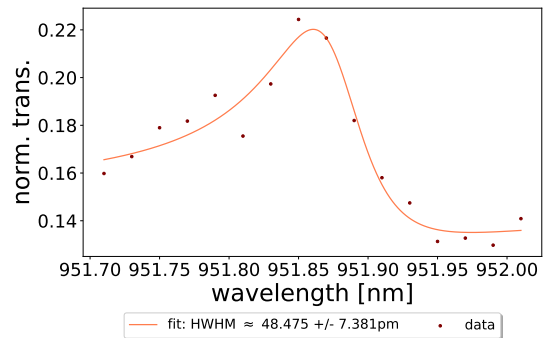
(b)



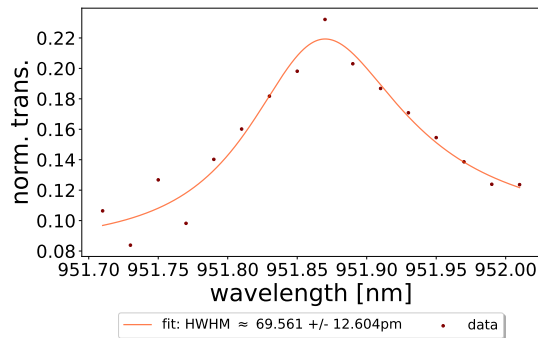
(c)



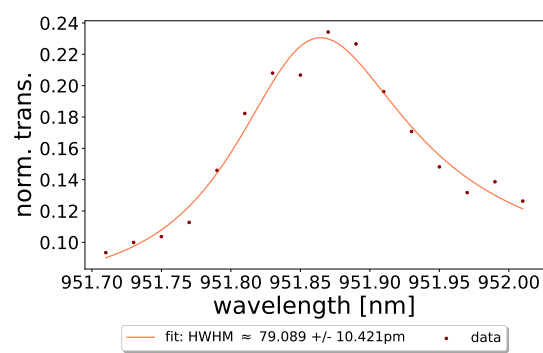
(d)



(e)

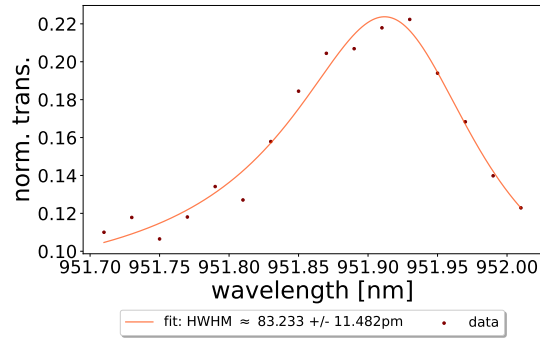


(f)

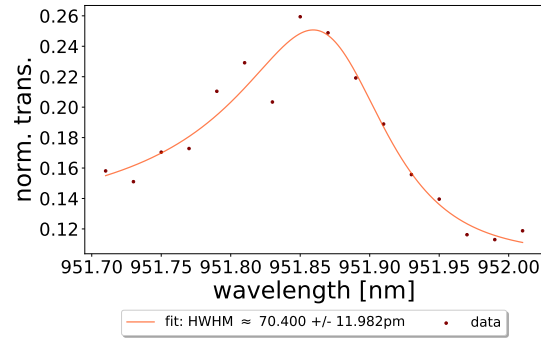


(g)

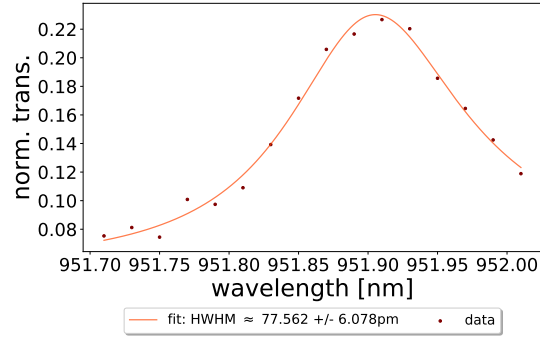
cavity length: $l \approx 66\mu m$



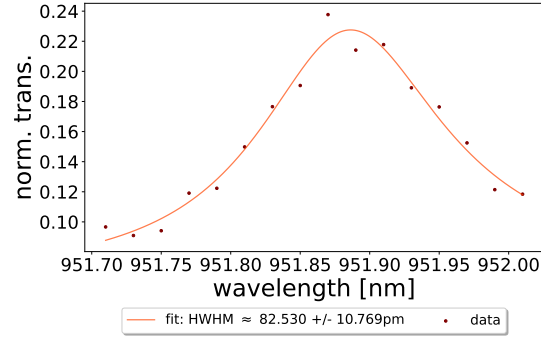
(a)



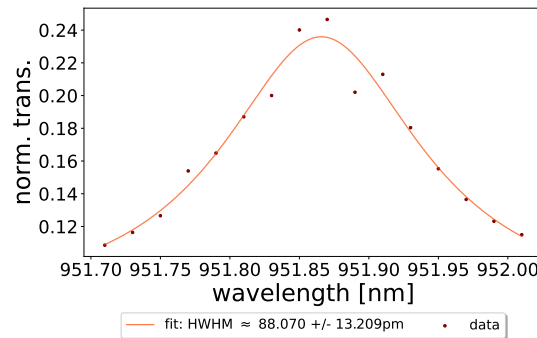
(b)



(c)

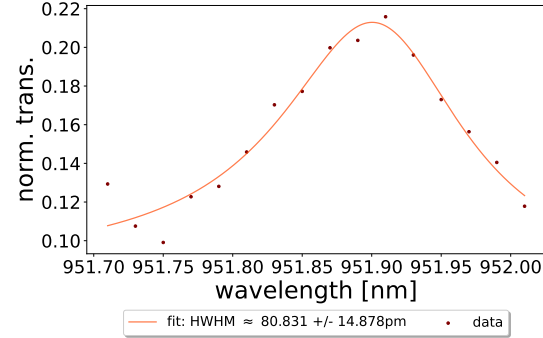
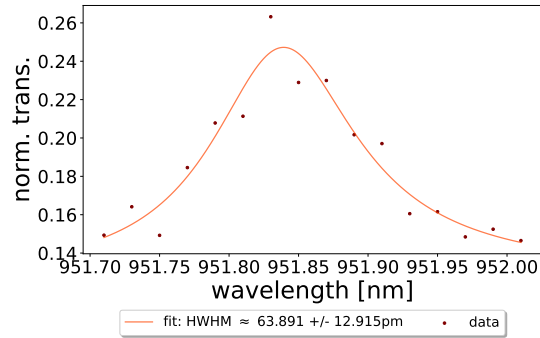


(d)



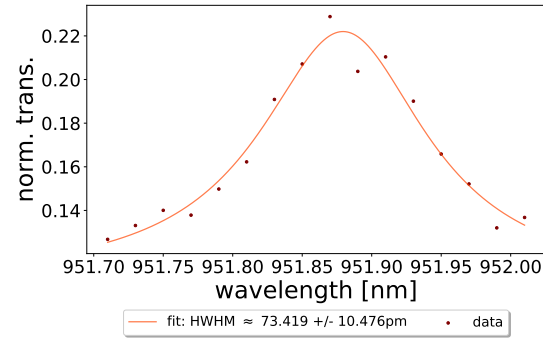
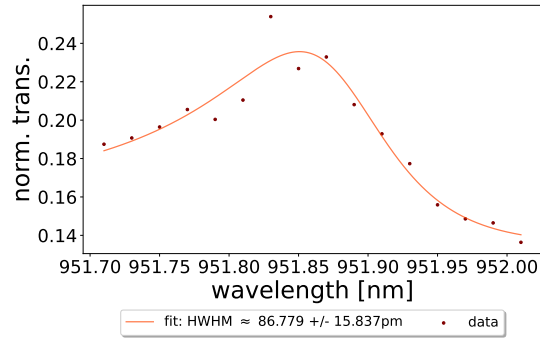
(e)

cavity length: $l \approx 17\mu m$



(a)

(b)

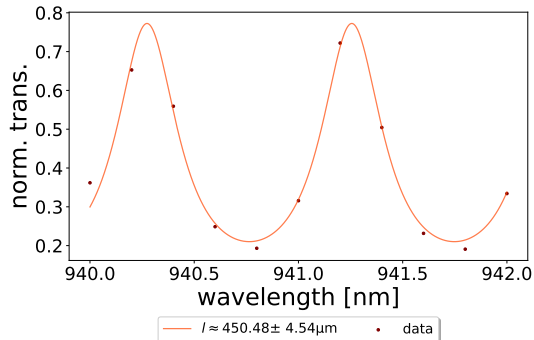


(c)

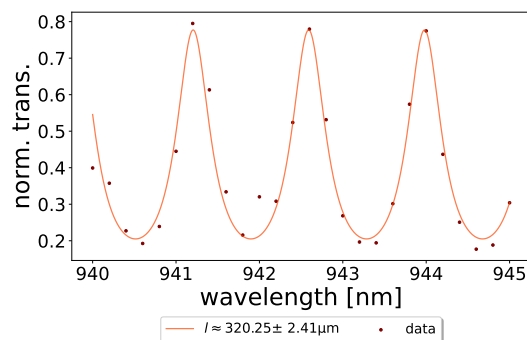
(d)

(Figure 71 in section 4.4)

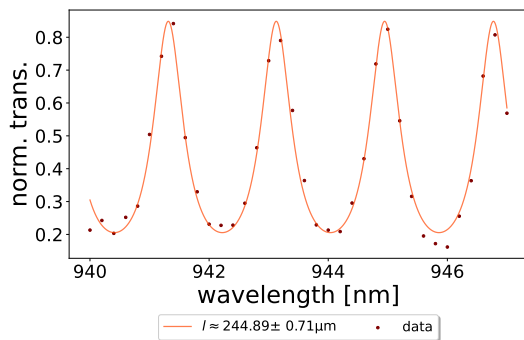
Off-resonance spectra (determining the cavity length)



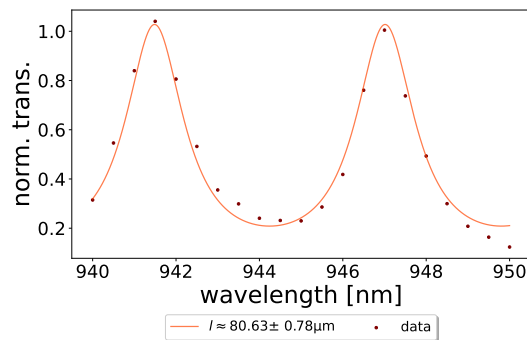
(a)



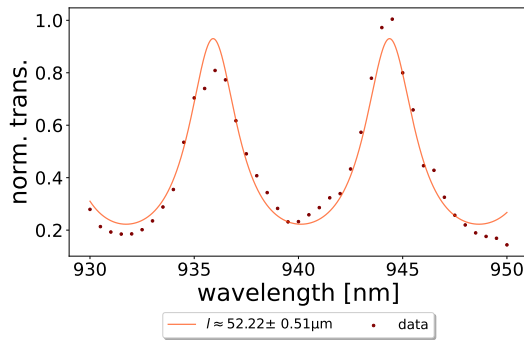
(b)



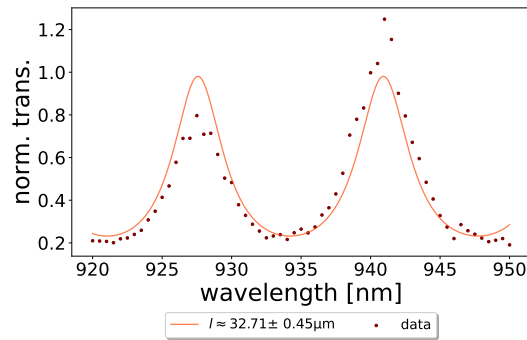
(c)



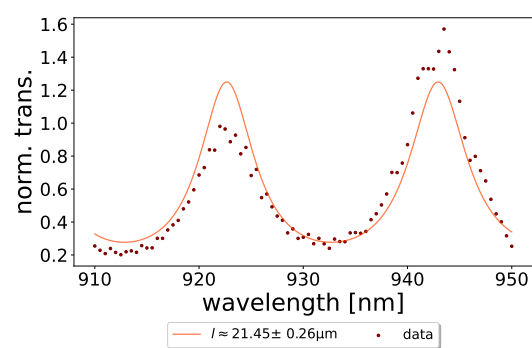
(d)



(e)

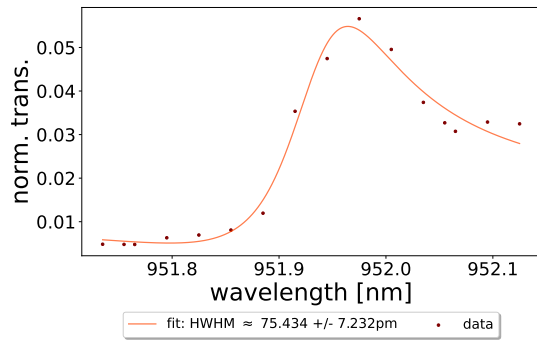
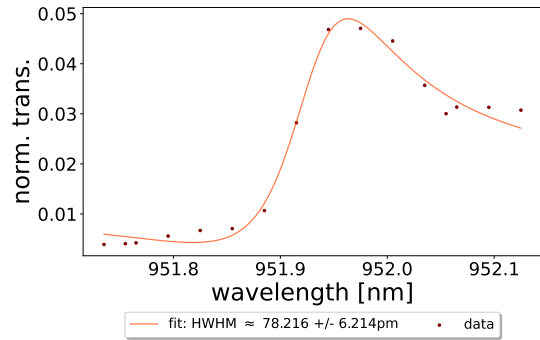


(f)



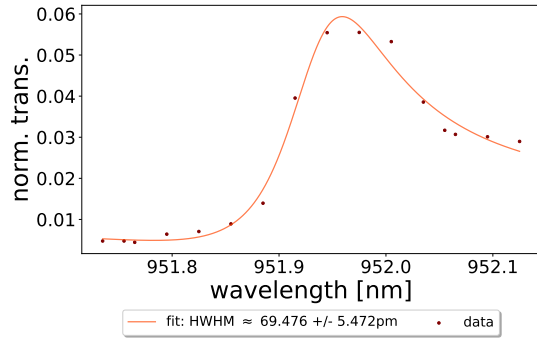
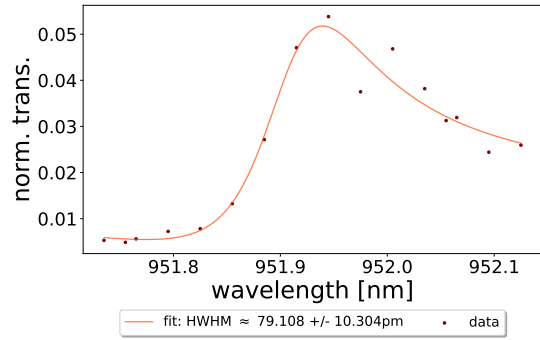
(g)

cavity length: $l \approx 450\mu m$



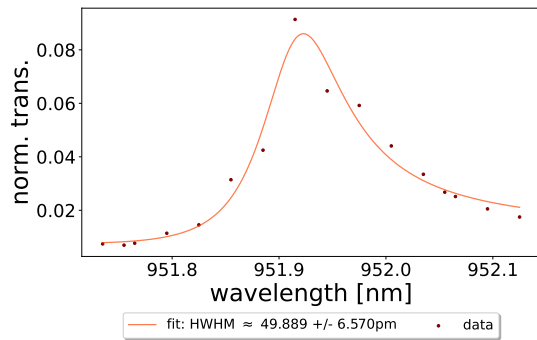
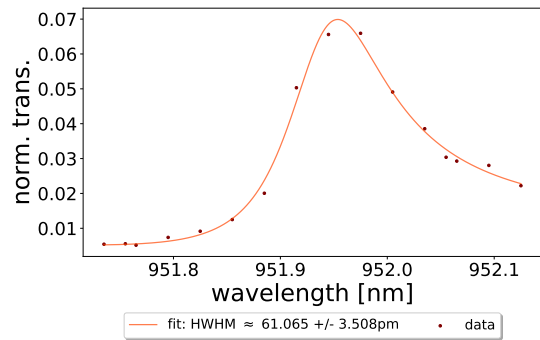
(a)

(b)



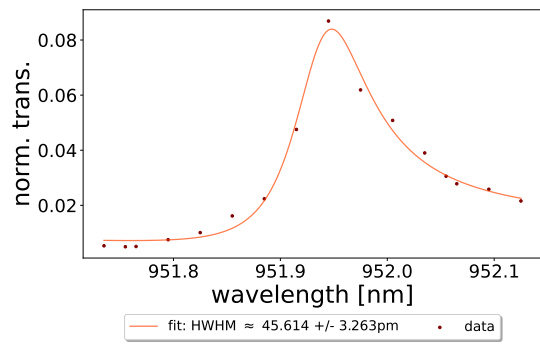
(c)

(d)

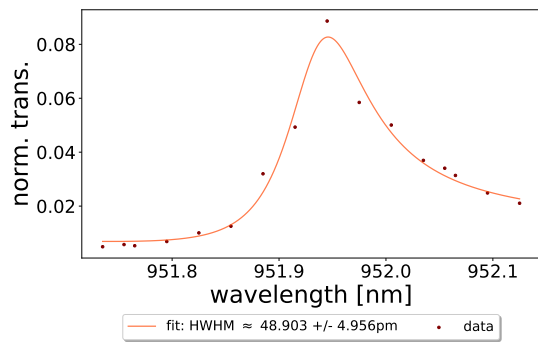


(e)

(f)

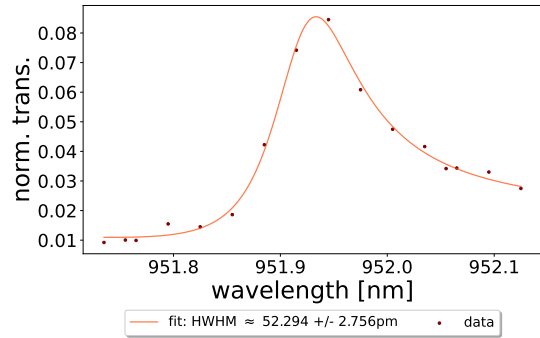


(g)

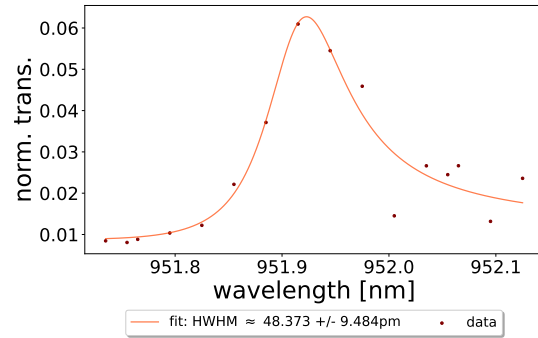


(h)

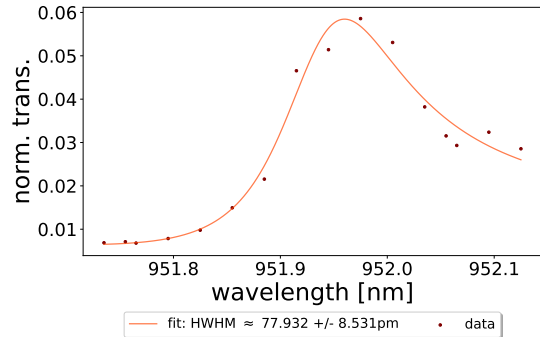
cavity length: $l \approx 320\mu m$



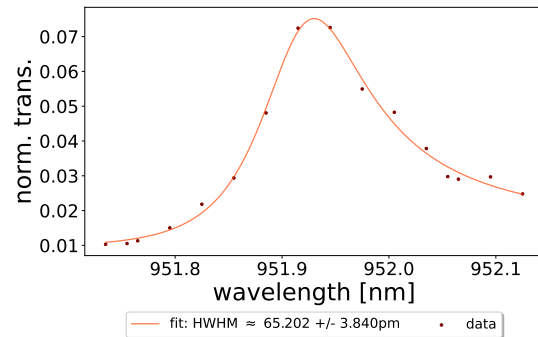
(a)



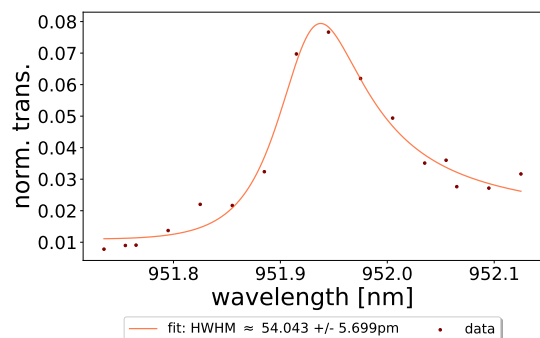
(b)



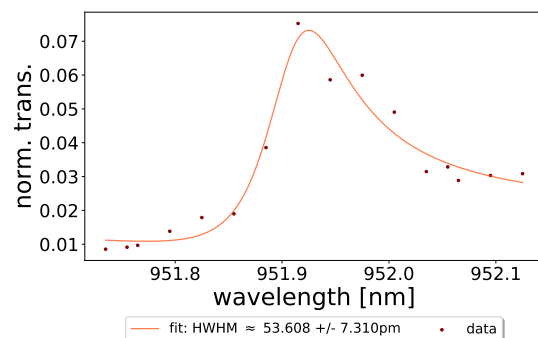
(c)



(d)

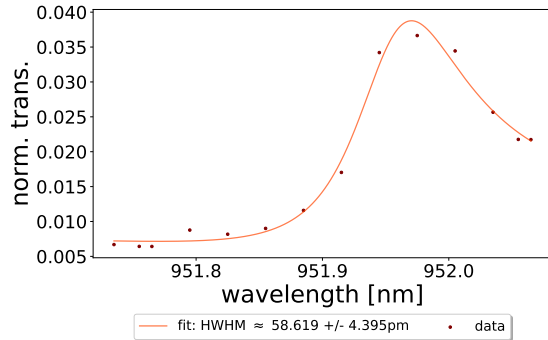


(e)

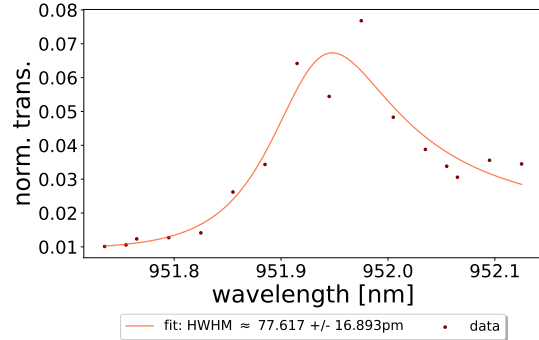


(f)

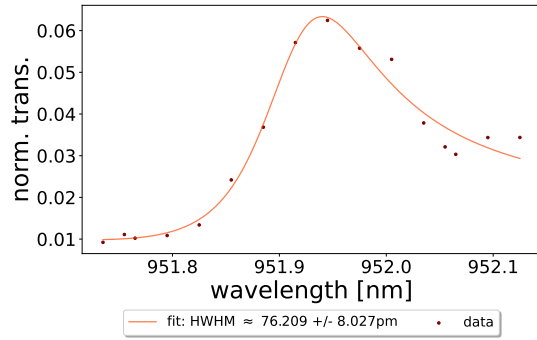
cavity length: $l \approx 245\mu m$



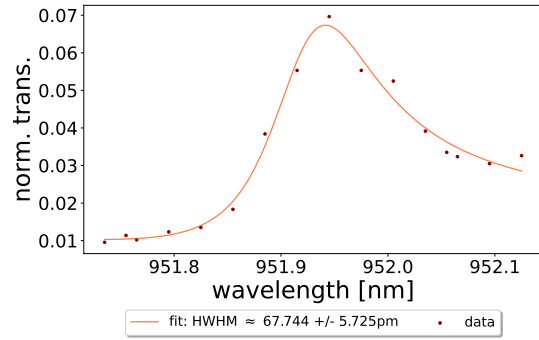
(a)



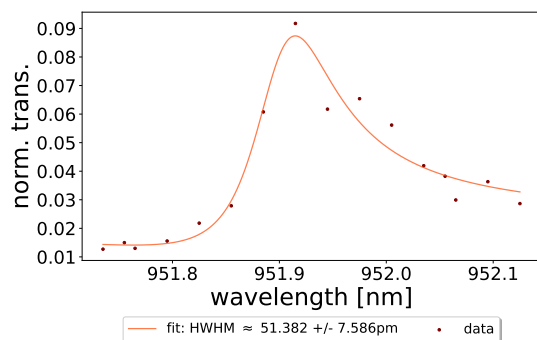
(b)



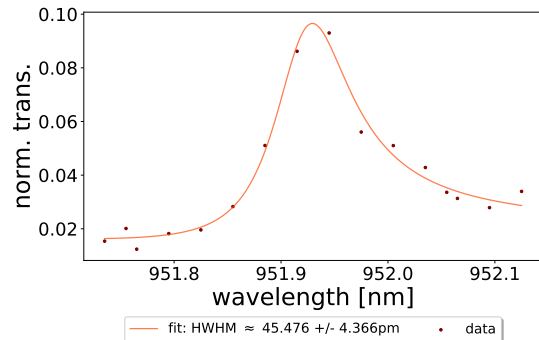
(c)



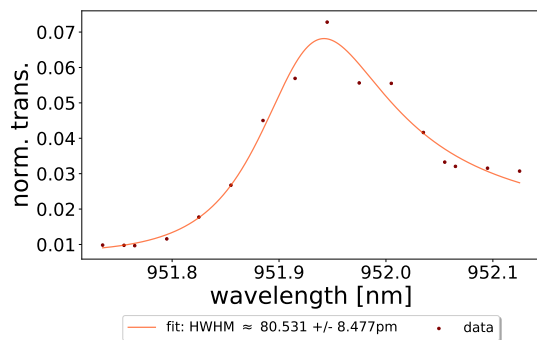
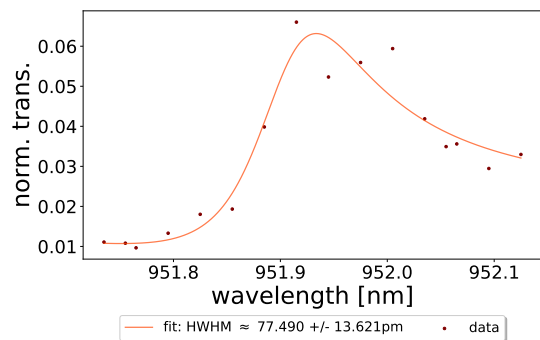
(d)



(e)

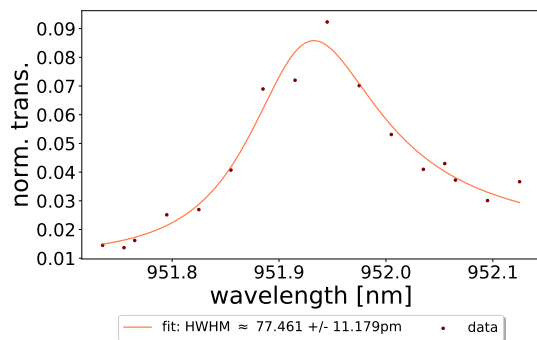
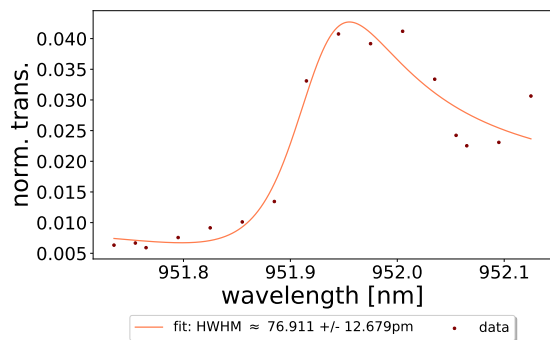


(f)



(g)

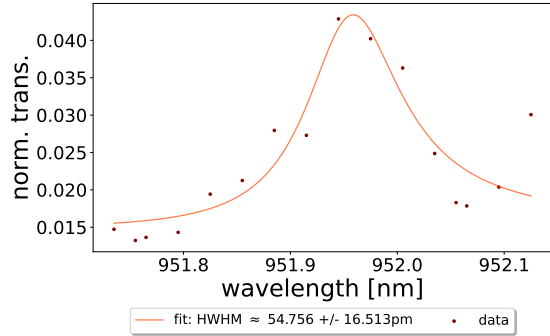
(h)



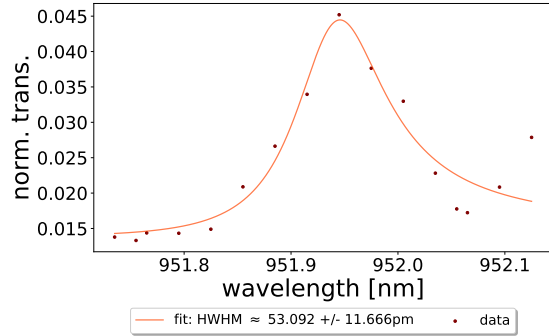
(i)

(j)

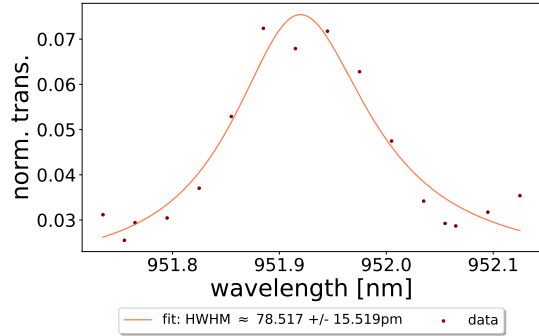
cavity length: $l \approx 81\mu m$



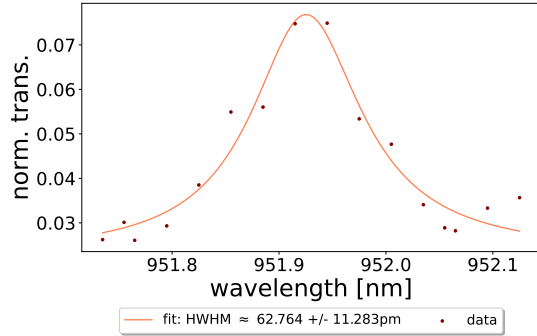
(a)



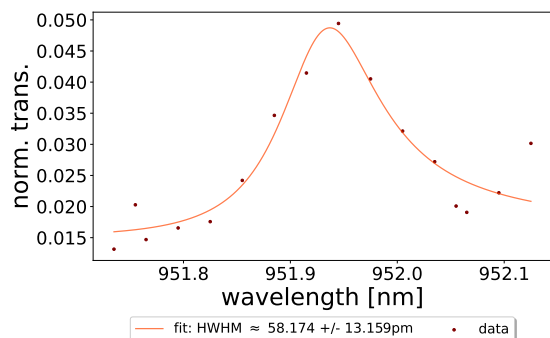
(b)



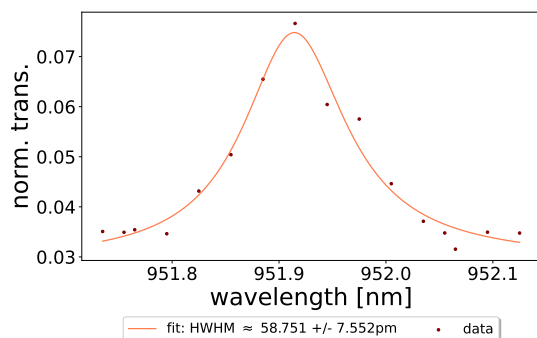
(c)



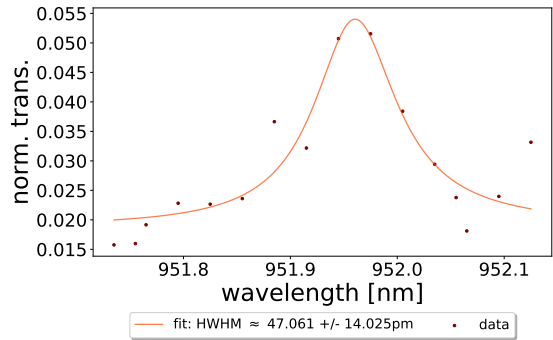
(d)



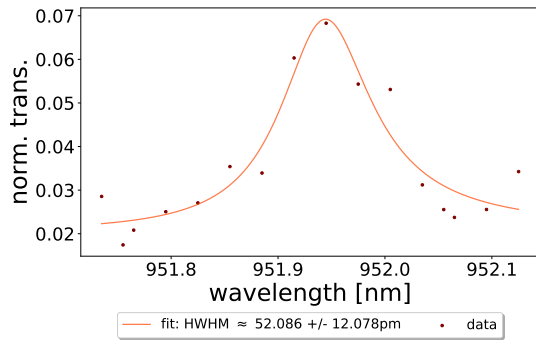
(e)



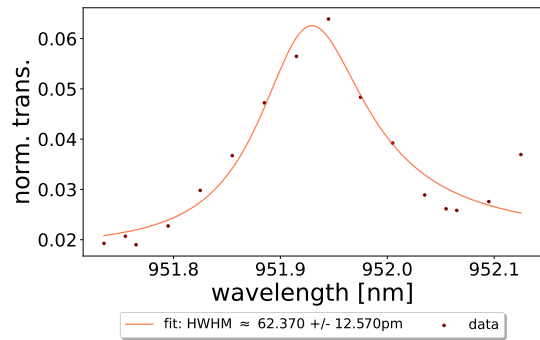
(f)



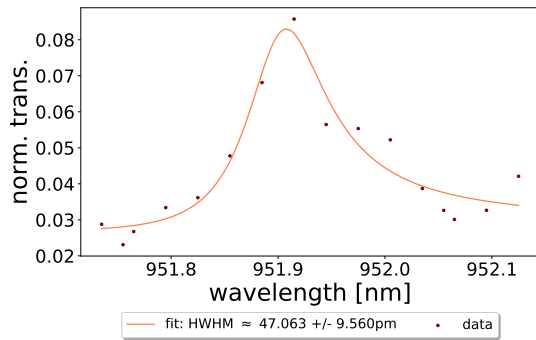
(g)



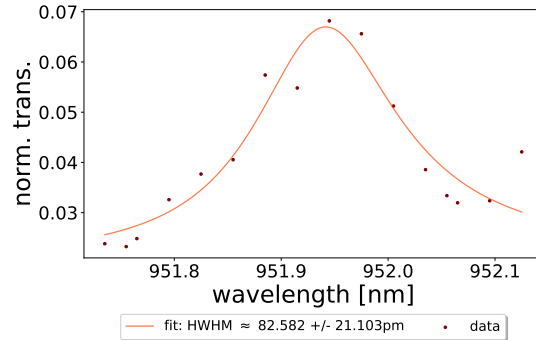
(h)



(i)

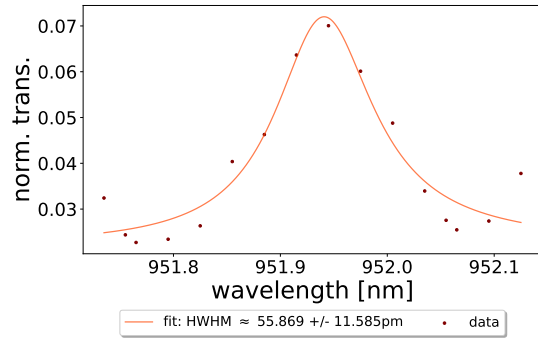


(j)

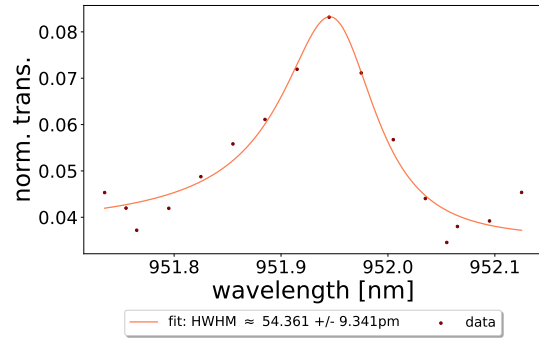


(k)

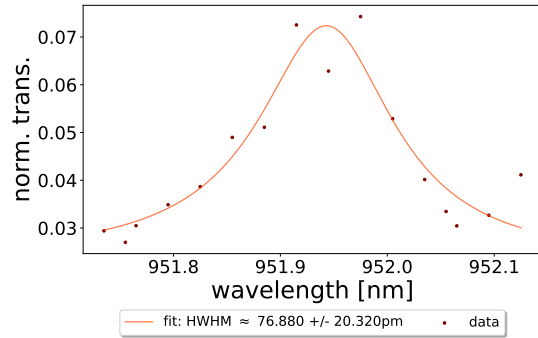
cavity length: $l \approx 52\mu m$



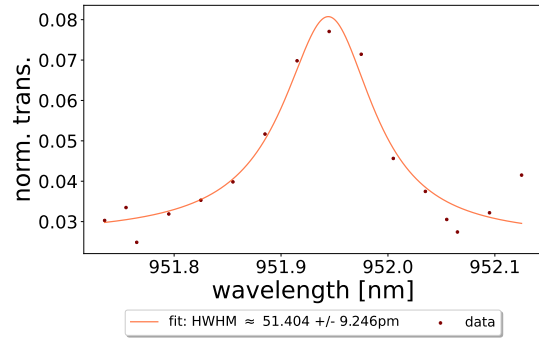
(a)



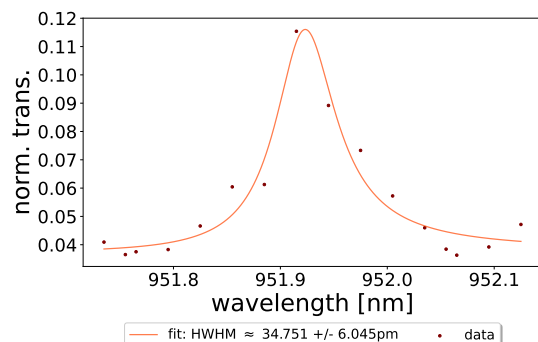
(b)



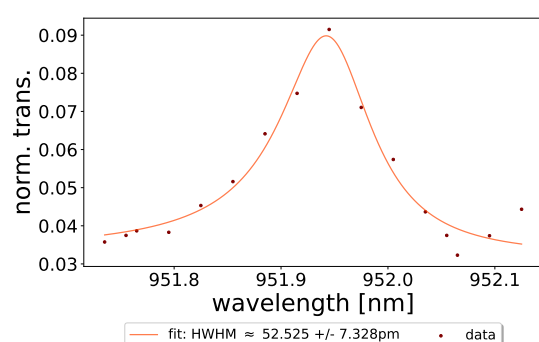
(c)



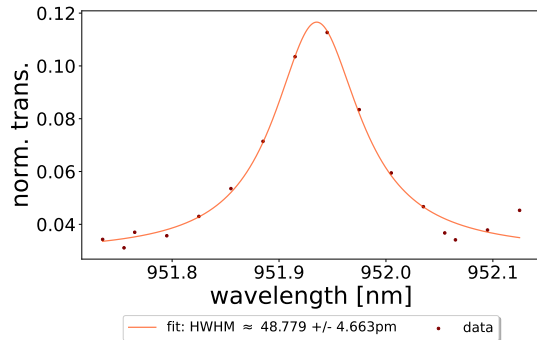
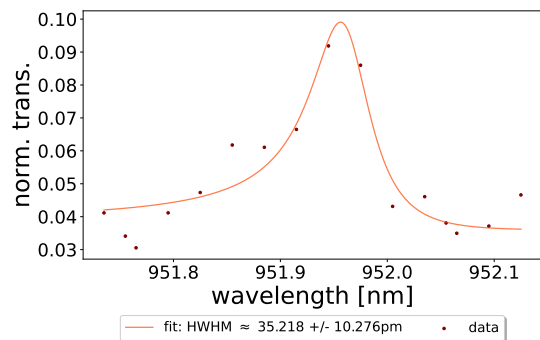
(d)



(e)

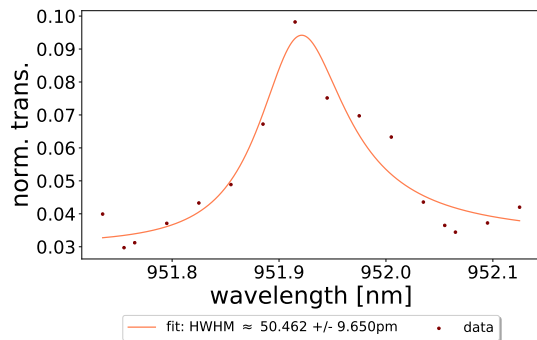
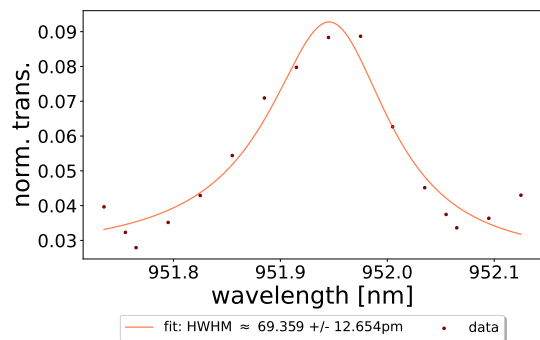


(f)



(g)

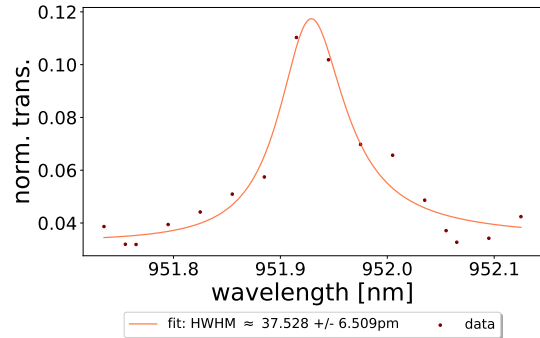
(h)



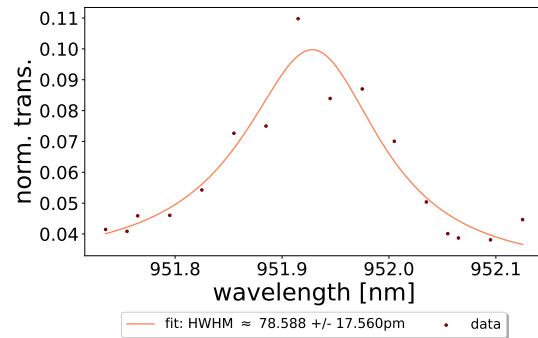
(i)

(j)

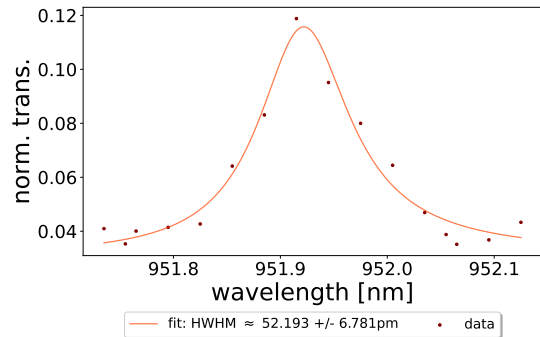
cavity length: $l \approx 33\mu m$



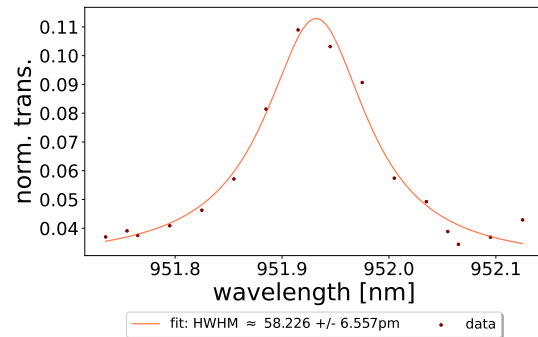
(a)



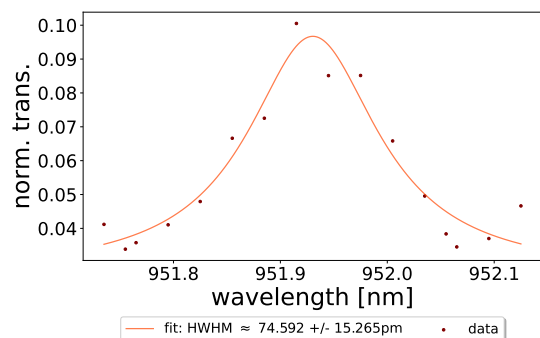
(b)



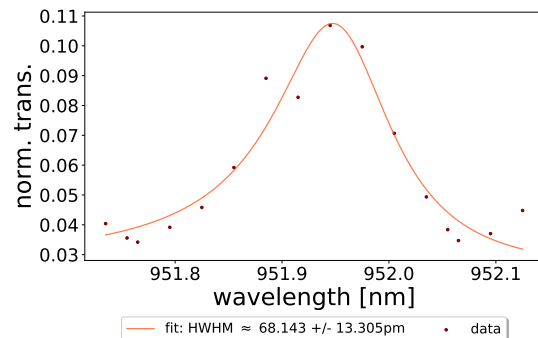
(c)



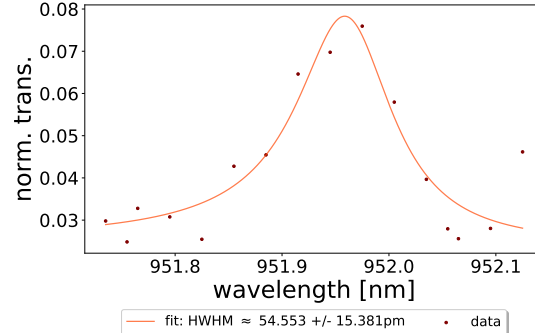
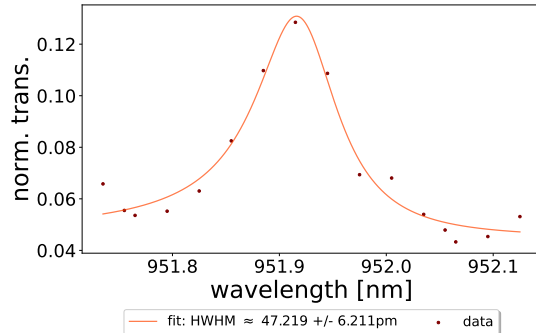
(d)



(e)

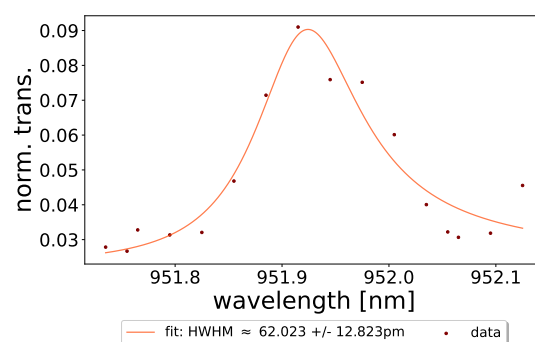
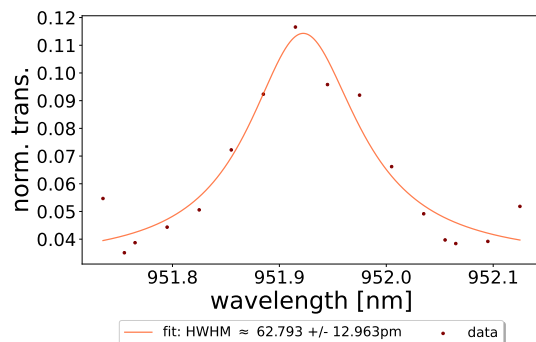


(f)



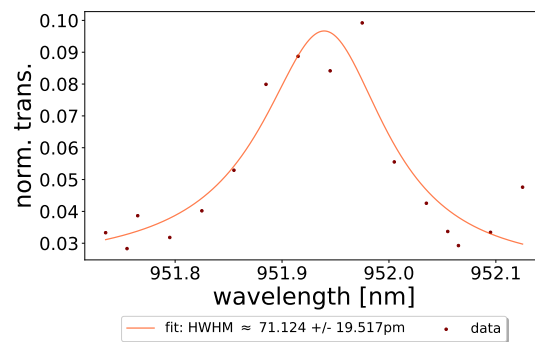
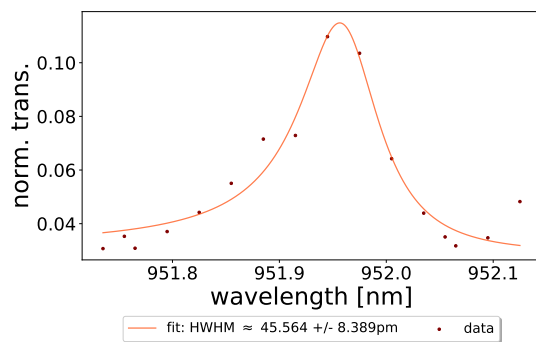
(g)

(h)



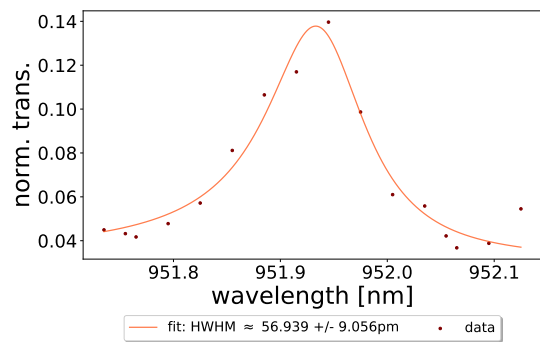
(i)

(j)

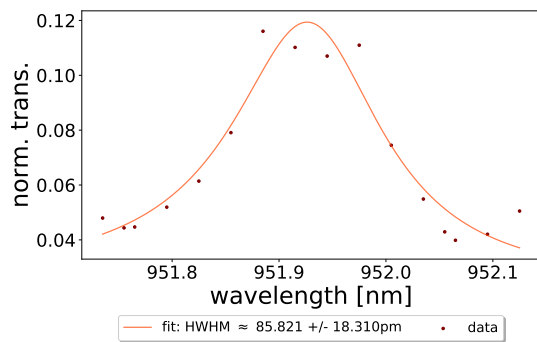


(k)

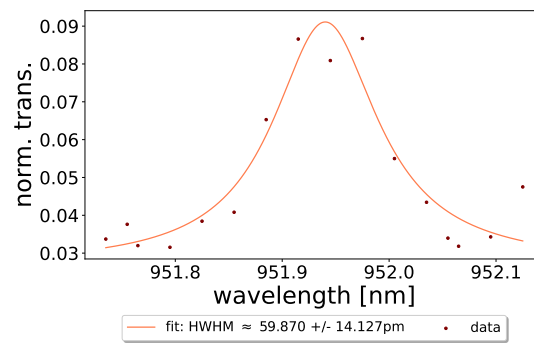
(l)



(m)

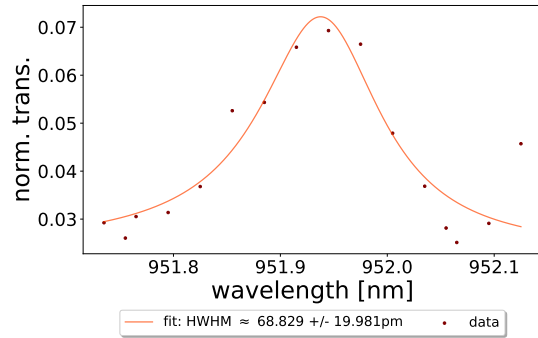


(n)

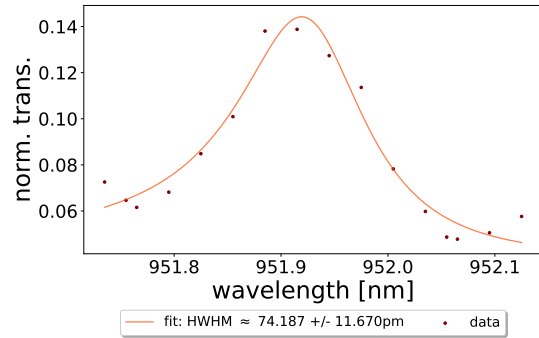


(o)

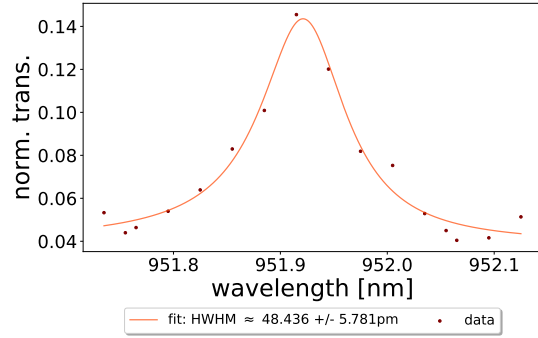
cavity length: $l \approx 21\mu m$



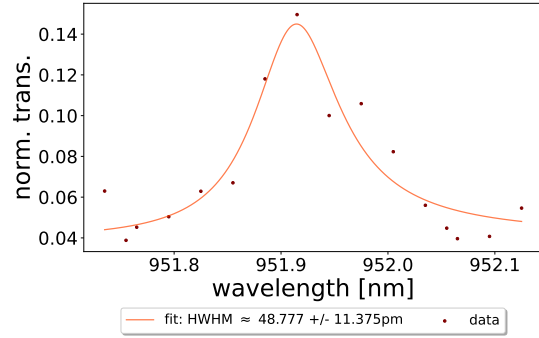
(a)



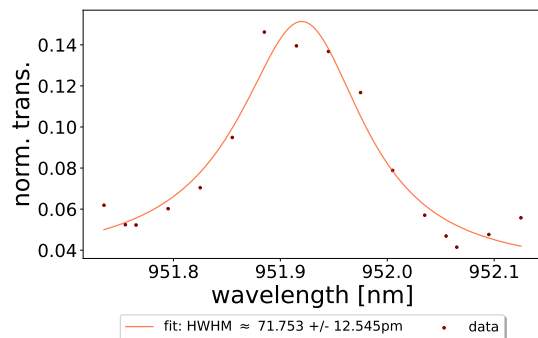
(b)



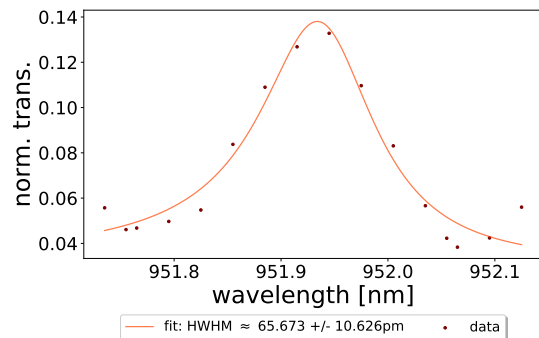
(c)



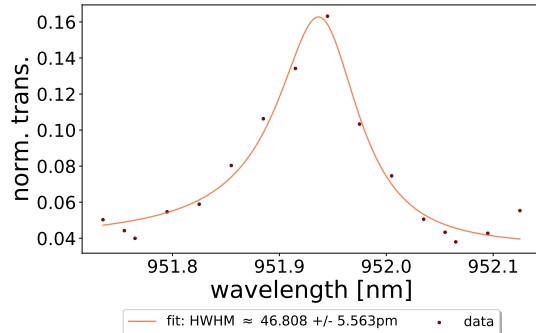
(d)



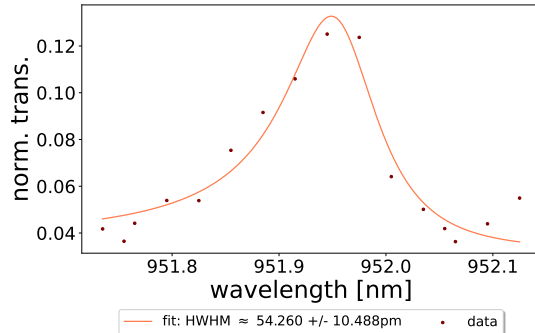
(e)



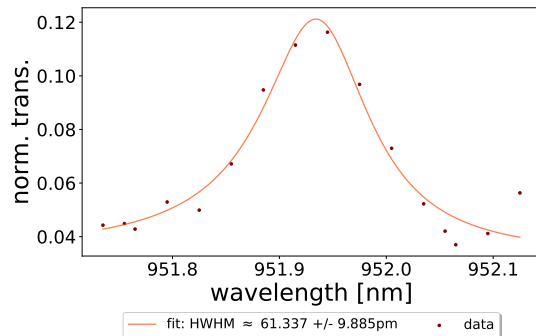
(f)



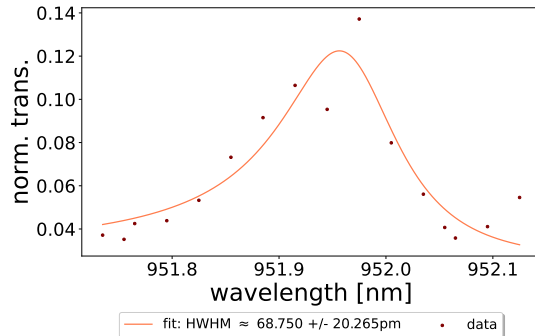
(g)



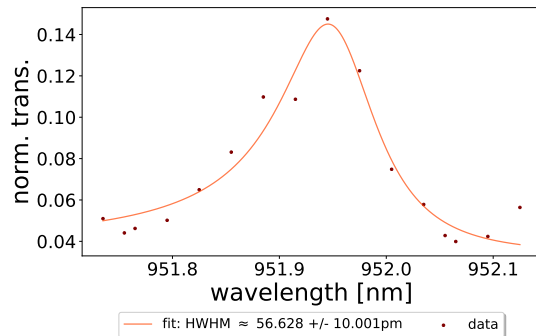
(h)



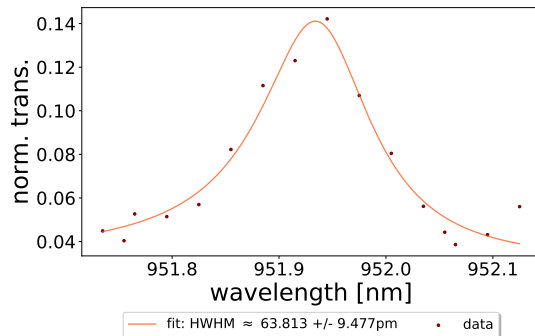
(i)



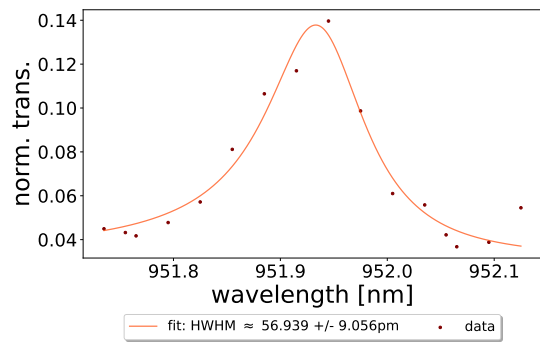
(j)



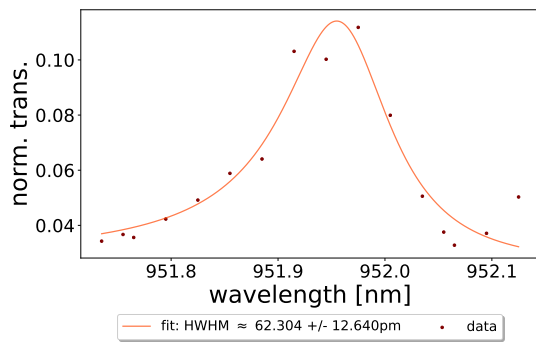
(k)



(l)



(m)



(n)

Things to add to appendix:

- The derivation of equation 33
- The derivation of equation 34
- Same derivations for the double fano cavity.
- Link to GitHub repo (data, scripts, figures, etc.)